LOS ALAMOS SCIENTIFIC LABORATORY
of the
University of California
LOS ALAMOS • NEW MEXICO

Calculation and Interpretation of the UHTREX Critical Experiments

UNITED STATES
ATOMIC ENERGY COMMISSION
CONTRACT W-7405-ENG. 36

This report expresses the opinions of the author or authors and does not necessarily reflect the opinions or views of the Los Alamos Scientific Laboratory.

Printed in the United States of America. Available from
Clearinghouse for Federal Scientific and Technical Information
National Bureau of Standards, U. S. Department of Commerce
Springfield, Virginia 22151
Price: Printed Copy $3.00; Microfiche $0.65

Written: August 1969
Distributed: June 1970

LA-4218
UC-80, REACTOR
TECHNOLOGY
TID-4500

LOS ALAMOS SCIENTIFIC LABORATORY
of the
University of California
LOS ALAMOS • NEW MEXICO

Calculation and Interpretation of the UHTREX Critical Experiments

by

B. M. Carmichael
J. C. Vigil
J. L. Meem, Jr.*

*Present address: Nuclear Engineering Department, University of Virginia, Charlottesville, Virginia.

CONTENTS

CALCULATION AND INTERPRETATION OF THE UHTREX CRITICAL EXPERIMENTS

by

B. M. Carmichael, J. C. Vigil, and J. L. Meem, Jr.

ABSTRACT

The UHTREX (Ultra High Temperature Reactor Experiment) critical experiments are analyzed in a detailed comparison of calculations with experiment. Critical masses and flux profiles; control rod, fuel, and void worths; and temperature and pressure coefficients of reactivity for the reactor operating at low power and ambient temperature are discussed.

1. INTRODUCTION AND SUMMARY

Two critical experiments were performed in support of the Ultra High Temperature Reactor Experiment (UHTREX). The first experiment, designated as UHTREX Critical Experiment I (UCX-I), was performed in a preassembly of the main UHTREX core and reflector components, and the second experiment (UCX-II) was carried out in the UHTREX facility itself. This report describes these critical experiments and compares the experimental results with calculations.

UCX-I was conducted in a separate facility which is described in the safety analysis report covering UCX-I.[1] The assembly, shown in Fig. 1.1, consisted primarily of the core graphite structure and the inner graphite and carbon reflectors of UHTREX. A special stand on top of the assembly provided support for the control rods, neutron source, and instrumentation. Convenient access was available for void, control rod, and other worth measurements as well as for activation experiments. UCX-I provided an early verification of the adequacy of the UHTREX control rod system and gave a first test of the unique fuel loading techniques required for the radially oriented fuel channels in the rotatable UHTREX core.

UCX-II was conducted at low power and at ambient temperature in the UHTREX facility to secure final verification of the reactor physics parameters prior to the hot startup of the reactor. The reactor assembly used in UCX-II is shown in Fig. 1.2. During the experiments, the remotely operated fuel loading facilities were thoroughly tested, the problem of providing an adequate neutron source for the hot restart of the reactor was resolved, and several refinements to the instrumentation were developed.

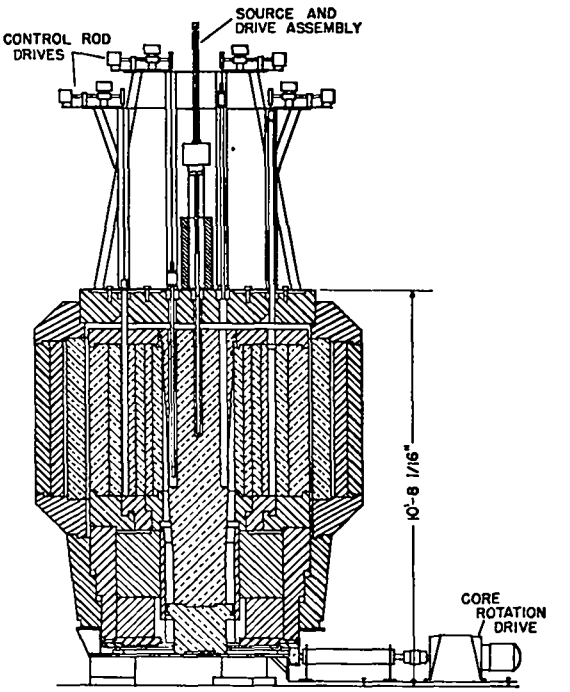

Fig. 1.1. UCX-I assembly.

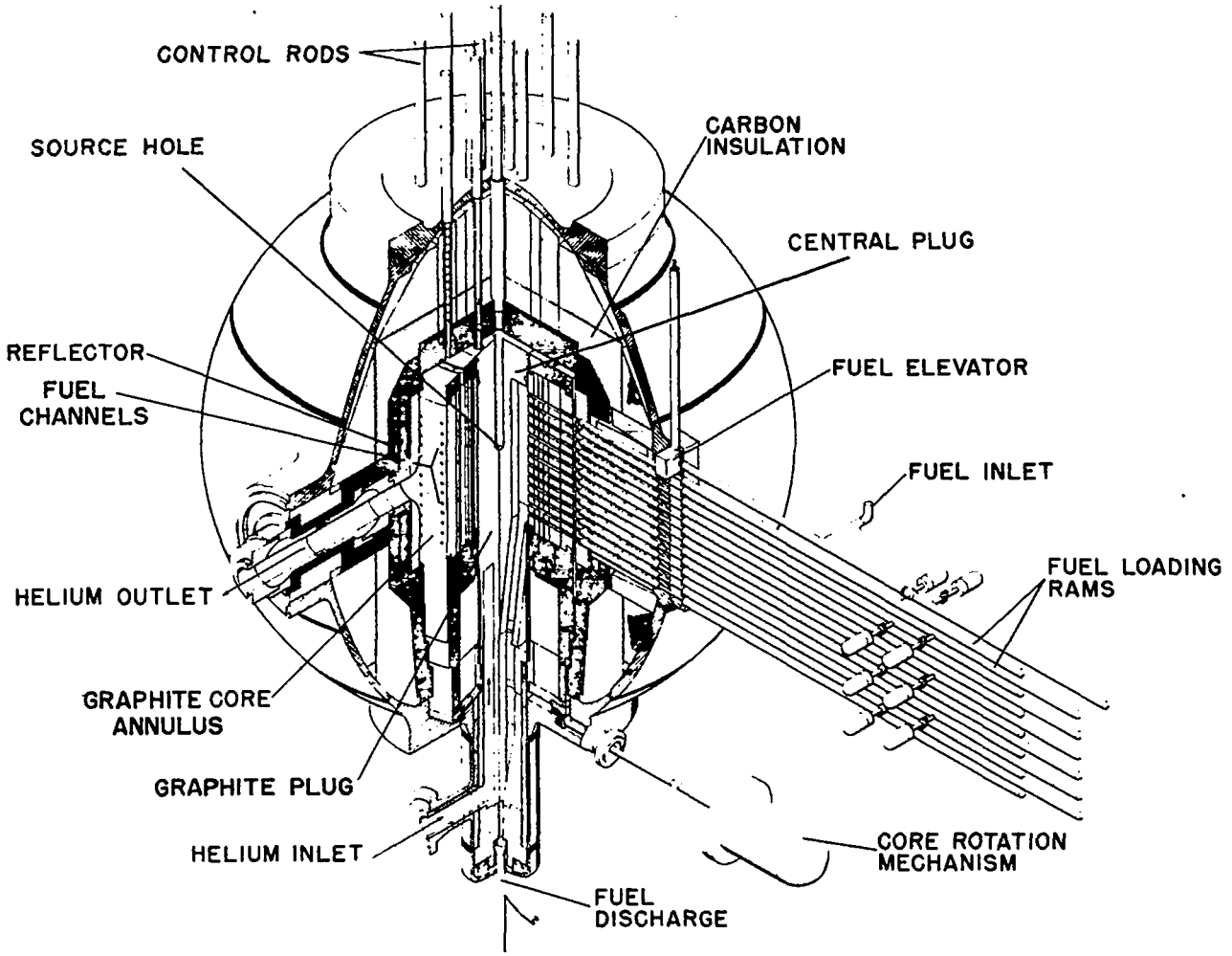

Fig. 1.2. UCX-II assembly.

In addition to checking some of the parameters such as the critical mass, the power profiles, and control rod worth measured previously in UCX-I, the pressure, ambient temperature, and flow coefficients of reactivity were measured for the first time in UCX-II.

A complete description of the UHTREX facility is given in the UHTREX Safety Analysis Report.[2] However, condensed descriptions of those components which were involved directly in the critical experiments are included in Sec. 2.1 for convenient reference.

Experimental results which were reported earlier in quarterly status reports[3] are reviewed in detail in Secs. 2.2 through 2.6. Critical masses observed were 7.003 and 6.277 kg in UCX-I and UCX-II, respectively. These are the total masses of uranium* which were required for criticality with all control rods withdrawn. The lower critical mass for UCX-II is due to the porous carbon and vessel, which provided added reflection not present in UCX-I.

The UCX critical masses are roughly comparable to the minimum critical mass of 5.5 kg uranium (5.2 kg ^{235}U) observed in the TREAT reactor.[4] TREAT is also a carbon-moderated uranium reactor with a carbon-to-uranium atom ratio (C/U) of 10,000; the C/U's for UCX-I and UCX-II were 8850 and 9875, respectively.

* In this report, uranium shall mean uranium enriched to 93% ^{235}U.

Other related critical experiments were the five carbon-moderated uranium configurations assembled in the Los Alamos Honeycomb facility. A summary description of these experiments is given by Iskenderian.[5] They were parallelepiped core assemblies reflected on all sides by 1 ft of graphite. The C/U in the Honeycomb experiments varied from 2200 to 6200 with critical masses of 8 to 10 kg uranium. The Honeycomb experiments were used as the reference configurations for normalizing calculations prior to the UHTREX critical experiments.

The differences in the critical masses in UHTREX, TREAT, and the Honeycomb experiments are attributed to the differences in the core configurations and compositions. The critical mass in TREAT was lower than in the other assemblies because the C/U was larger and because the fuel was homogeneously dispersed in the core graphite. In UHTREX, the fuel is concentrated in 1-in.-o.d. x 0.5-in.-i.d. x 5.5-in.-long fuel elements that contain only 4% of the core graphite, and, inside the fuel elements, the fuel is further concentrated in coated particles. Another contribution to an increased critical mass in UHTREX is the inert central plug region inside the core cylinder (Fig. 1.2). The larger critical masses in Honeycomb were due primarily to the lower C/U and to the self-shielding effects of distributing the uranium in the core in the form of metallic foils.

The fuel loading apparatus and procedures in UHTREX are designed to permit the core loading to be varied over a wide range, while preserving symmetry in the loading and while maintaining a constant geometry. The cylindrical core has 312 evenly distributed radial fuel channels, each of which contains 4 fuel elements. When new fuel elements are added to a channel, the fuel loading in these elements is increased in a geometric progression in order to give a smoothly varying increase in total core loading. In addition, by loading channels in the appropriate sequence, symmetry in the loading is preserved even for large loading changes.

This loading sequence was followed in the approach to critical and was continued in order to maintain criticality as control rods were inserted. In this way, rods were calibrated in terms of critical mass. At intervals, period measurements were performed to determine the current reactivity worth of fuel additions, which enabled conversion of the mass equivalent rod worths to reactivities.

The control rods in UHTREX are described in detail in Sec. 2.1. Four of the rods are borated steel rods equally spaced on approximately the mean radius of the rotating core annulus. The eight remaining rods are boron carbide rods situated in the fixed inert region inside the core annulus.

The methods used in UHTREX calculations and comparisons between experiment and calculations are given in Sec. 3. For any given configuration, infinite medium calculations were first performed to obtain a flux spectrum to use in collapsing cross sections to a few-group set. Separate reduced cross-section sets were derived for the core and reflector regions because of the differences in the thermal neutron spectra in the two regions. Typical spectra of the core and reflector media are shown in Fig. 1.3. The uranium absorber in the core produces significant hardening of the thermal spectrum, compared to the spectrum in a pure graphite medium.

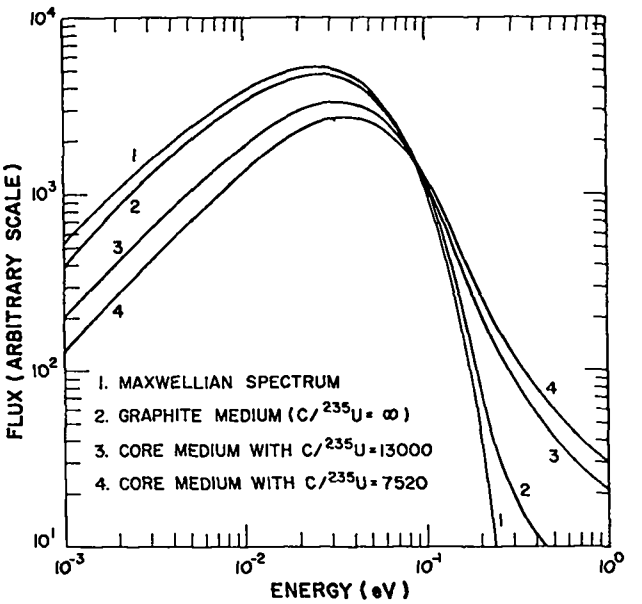

Fig. 1.3. Infinite medium spectra for thermal neutrons at 293°K.

The thermal spectrum in the UHTREX core is still relatively soft, however. Approximately 96% of the fissions in UHTREX are caused by thermal neutrons. Because of the softness in spectrum, the fuel loading required for criticality is very sensitive to the presence of thermal poisons such as the graphite contaminants. Lists of the impurities, found in the UHTREX graphite and carbon components, are given in Appendix A. The derivation of few-group microscopic cross sections and associated spectrum problems are discussed in Sec. 3.2.

In addition to the spectrum calculations, other preparatory calculations are required to account for the heterogeneities in the core. As mentioned previously, the fuel is lumped in two respects. First, it is concentrated in fuel elements within the core, and second, it is lumped in coated UC_2 particles within the elements. The spherical UC_2 particles, which are nominally 150-μ diam, are small compared to the mean free path of thermal neutrons. Consequently, secondary collisions may be neglected and the simple theory of fuel particle self-shielding as discussed in Appendix B is applicable. The particle self-shielding correction factors were applied to cross sections prior to their use in the infinite medium calculations discussed above.

In the case of the fuel element self-shielding, the elements are large compared to the mean free paths of thermal neutrons; consequently, diffusion or transport effects must be considered. These were taken into account by performing cell calculations using the one-dimensional DTF-IV S_n code.[6] The radially oriented fuel channels and associated moderator, however, do not in all respects constitute a repetitive or cellular geometry. The geometry of the core is repetitive in the vertical and azimuthal directions but, in the radial direction, the spacing between channels increases continuously with radius over the extent of the core. Consequently, the geometry in the radial direction is not cellular. Nevertheless, it was found that infinite cylinder models of the fuel elements and their associated moderator were satisfactory for estimating flux weighting factors or disadvantage factors. Details of the fuel element self-shielding calculations are covered in Sec. 3.3.

The effective cross sections from the infinite medium and cell calculations were part of the input to the finite two-dimensional cylinder (R,Z) calculations used to obtain eigenvalues and flux profiles. The detailed two-dimensional reactor models for the remaining input are described in Sec. 3.4. A 33-region vertically asymmetric model was developed for UCX-I, and a 26-region vertically symmetric model was adopted for UCX-II. The top and bottom reflectors on UCX-II were nearly equivalent, but UCX-I was much better reflected on the bottom.

In the formulation of the calculational models, the most important requirement was the faithful representation of the amount and distribution of thermal absorbers in both the core and reflector regions. Thus, homogenization of voids was avoided where practicable because such homogenization leads to a redistribution of materials. A large number of voids exist in UHTREX to provide for coolant passageways, expansion clearances, and control rod holes. As a further mark of the necessity for accurate treatment of absorbers, it was found that the air in the voids had a small but nonnegligible effect on criticality.

For the finite two-dimensional calculations, the 2DF S_n code[7] was used. The calculated k_{eff}'s for the reference configurations in the critical experiments are given in Table 1.1. The same calculations provided specific power profiles (thermal flux profiles) which are in close agreement with experiment. These power measurements were performed by direct counting of fuel elements as described in Sec. 2.3. These and other thermal flux measurements described in Sec. 2.3 are compared to calculations in Sec. 3.3 and 3.4.

TABLE 1.1

CALCULATED k_{eff}'s FOR REFERENCE CONFIGURATIONS

	Experimental Critical Mass (kg U)	Calculated k_{eff}
UCX-I	7.003	0.998
UCX-II	6.277	1.003

The importance of the reflectors is illustrated by the difference in critical masses observed in UCX-I and UCX-II. Further insight into the action of the reflectors is provided by the neutron economy analysis given in Sec. 3.4. In particular, 44% of all neutrons produced leak from the core. Of these, about 2% or less are thermal and the remainder are above thermal. The total leakages in UCX-I and UCX-II are 31% and 0.5%, respectively. However, the graphite reflectors in UCX-II are far from infinite in their effect on thermal neutrons since 21% of all neutrons produced are absorbed in the steel vessel.

Although the methods used in the control rod calculations are described in a separate report,[8] they are reviewed briefly in Sec. 3.5. Two basically different approaches were used. An analytic two-group multiregion method was used in scoping and design calculations, and numerical calculations with the R-θ options of the multigroup two-dimensional CRAM[9] diffusion and 2DF S_n codes were done to confirm the more approximate analytic calculations.

The calculated and experimental rod worths are shown in Fig. 1.4.

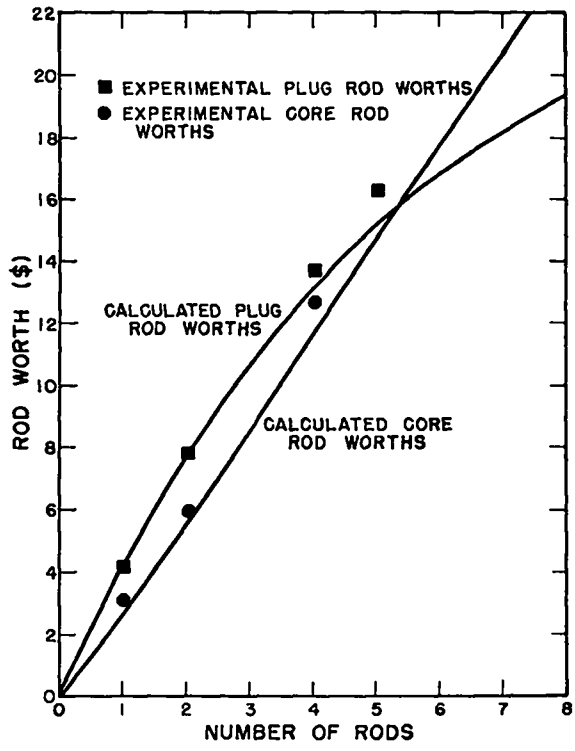

Fig. 1.4. Rod worths.

A variety of perturbation measurements and calculations were performed. The perturbation measurements were done with the standard technique of observing the displacement of a calibrated rod required to maintain criticality while a given perturbation is applied. For the perturbation calculations, a code was used which calculates the worth of an arbitrary perturbation of the macroscopic cross sections of a reactor using the regular and adjoint fluxes and currents from two-dimensional S_n calculations. The perturbation calculation methods are described in Sec. 3.6.

Some of the perturbation results are summarized in Table 1.2. Each perturbation is an increase in the cited parameter in the critical assembly at ambient temperature and pressure conditions, and with all control rods removed except for the small amount of control rod insertion necessary for performing the measurement. Explanations for the differences between calculation and experiment in the pressure and temperature coefficients are given in Sec. 3.6.

TABLE 1.2

SUMMARY OF PERTURBATION RESULTS FOR UCX-II AT ROOM TEMPERATURE

Isothermal temperature coefficients (¢/°K)		
Net	-0.98	-1.02[a]
Core	-2.73	
Reflector	+1.75	
Fuel element	-0.23	
Gas pressure coefficients (¢/psi)		
Helium	+0.025	
Nitrogen	-5.4	
Air	-4.2	
Self-shielding worths ($)		
Coated particle	-3.02	
Fuel element	-5.24	-5.06[a]
Average fuel worth (¢/g)	0.74	0.77[a]
Effective delayed neutron fraction	0.00679	

[a] Computed by the k_{eff} difference method from two-dimensional S_4 calculations.

In general, the UHTREX reactor configuration is sufficiently complex that experimental verification of calculations was necessary. While the experiments performed previously in other carbon-moderated enriched-uranium assemblies (TREAT and Honeycomb) were useful, such configurational differences in UHTREX as the fuel and void distributions and the complex reflector geometry necessitated separate experimental investigation. As is seen in Table 1.1, the combined experimental and analytical program associated with the UHTREX critical experiments has led to the development of an accurate calculational representation for UHTREX.

2. CRITICAL EXPERIMENTS

2.1 Description of the Reactor and Mockup

The UHTREX reactor (Fig. 1.2) was used in the final critical experiments (UCX-II), and the mockup assembly (Fig. 1.1) was used in the preliminary experiments (UCX-I). The same core, fuel elements, central graphite plug assembly, and the dense graphite and carbon components of the outer reflector were used in both UCX-I and UCX-II.

The core is a graphite cylindrical annulus 70 in. o.d. x 23 in. i.d. x 39 in. high. Each fuel channel (Fig. 2.1) contains four fuel elements resting end-to-end in a nominal 1.1-in.-diam hole penetrating the core cylinder along a radius. The fuel channel axes lie in 13 horizontal planes spaced at 3-in. intervals and in 24 vertical planes spaced at 15° angular intervals. In sum, there are 312 channels containing 1248 fuel elements.

The fuel elements are hollow graphite cylinders 1 in. o.d. x 0.5 in. i.d. x 5.5 in. long loaded with uranium particles (Fig. 2.2). The particles consist of nominal 150-μ-diam spherical cores of UC_2 which contain a coating of about 100 μ of pyrolytic carbon. Further details concerning particle specifications are given in Refs. 2 and 10.

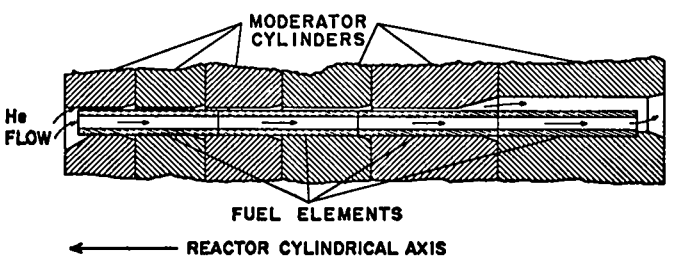

Fig. 2.1. Fuel channel geometry.

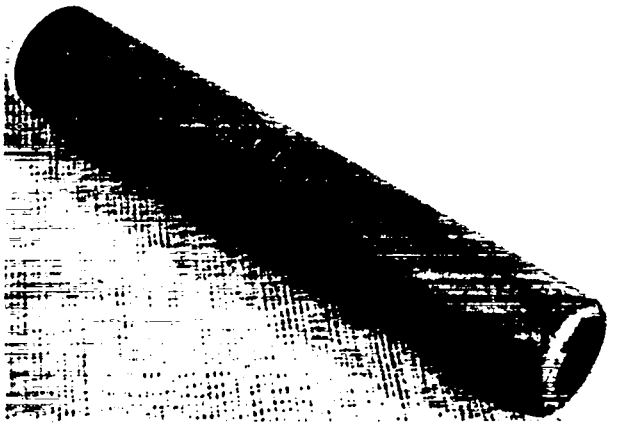

Fig. 2.2. Fuel element.

Nine different fuel element loadings (Table 2.1) were used in the critical experiments. At least 312 elements were available for each loading.

The core and other components shown in Fig. 2.3 were rotatable in both UCX-I and UCX-II to permit loading of the fuel elements from a fixed side position. Torque to rotate the assembled annulus was provided by a motor-driven shaft geared to the steel plate supporting the assembly.

The nonrotatable graphite and dense carbon components common to both UCX-I and UCX-II are shown in Fig. 2.4. These include a central graphite cylindrical plug that fits inside the core annulus, the shells of graphite and dense carbon that surround the core to act as the principal radial reflectors, and a top plate of dense carbon which, together with the dense carbon ring on top of the movable annulus, is the principal top reflector.

TABLE 2.1

URANIUM LOAD IN ELEMENTS

Group	Average Mass (g U/element)	Density (mg U/cm^3)
1	3.54	67
2	4.16	78
3	4.82	91
4	5.67	107
5	6.57	124
6	7.65	144
7	8.93	168
8	10.48	197
9	12.08	228

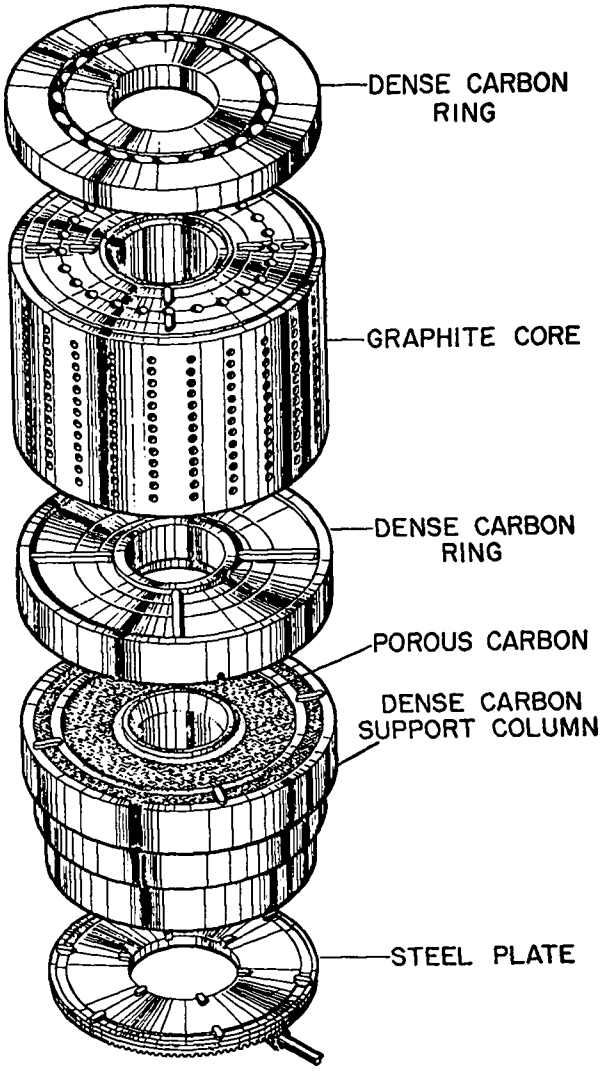

Fig. 2.3. Rotatable components.

The vessel and carbon insulation (Fig. 1.2) were present only in the UCX-II assembly. The vessel is a spherical steel shell 1.75 in. thick with an inner diameter of 13.2 ft. The carbon insulation, consisting of porous carbon of density 1.0 g/cc, filled the space between the dense components (shown darkened in Fig. 1.2) and the vessel.

Fuel elements were loaded manually into UCX-I. The core was rotated to bring the desired vertical row of channels into alignment with a row of holes (Fig. 2.4) in the stationary outer reflector. A

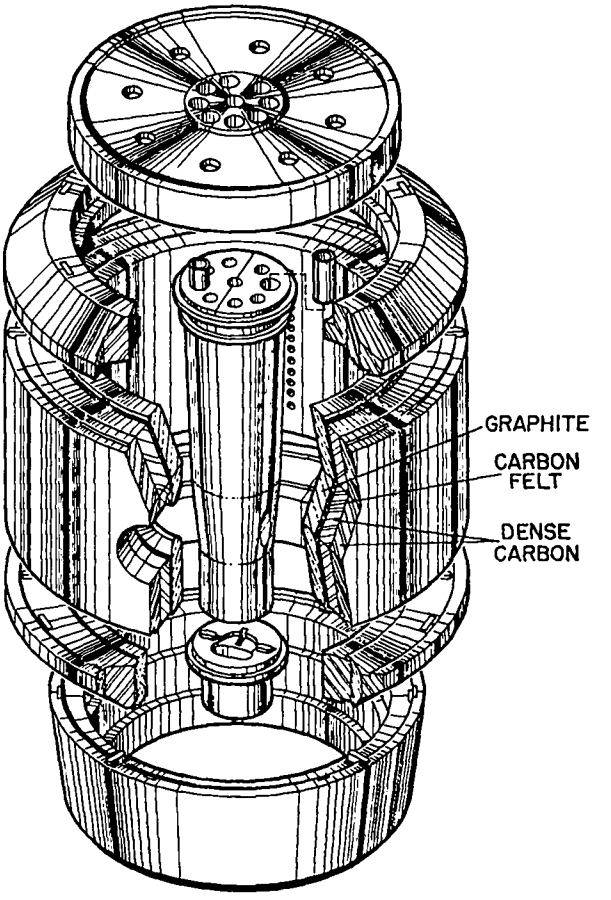

Fig. 2.4. Nonrotatable components.

fuel element was next pushed into one of the channels of the selected row using a tool (Fig. 2.5) consisting of a push rod with its length of stroke restricted to provide the correct depth of entry into the channel. Elements already in the channel were displaced inward one position with the original innermost element being displaced into a vertical slot in the central plug. This element fell

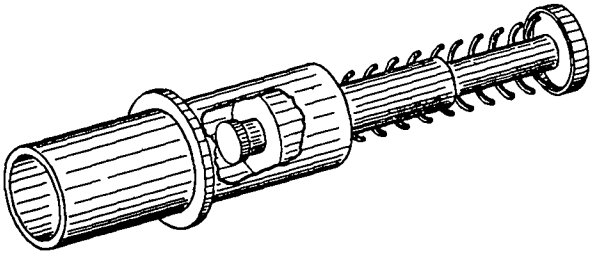

Fig. 2.5. Fuel loading tool.

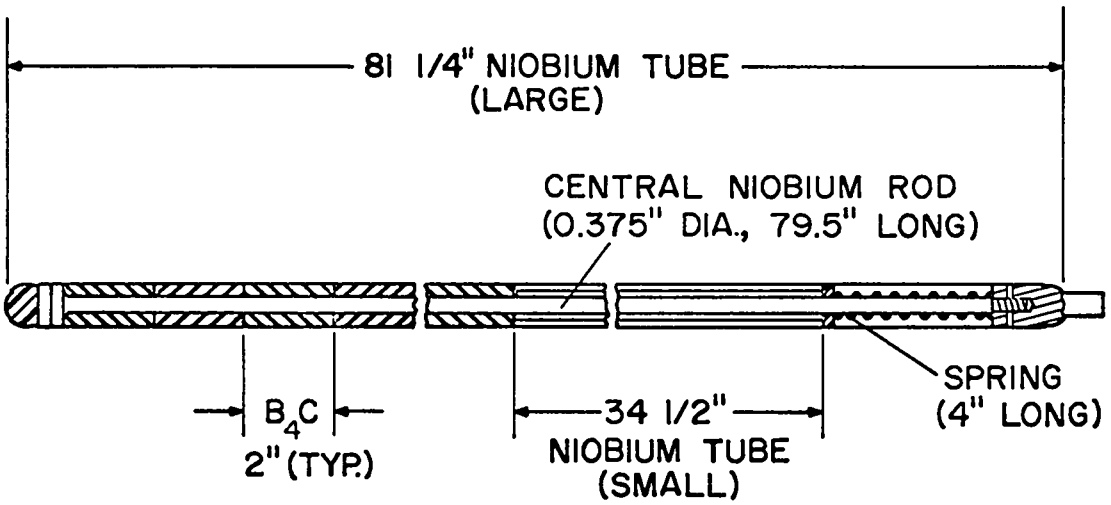

Fig. 2.6. Plug control rod.

into a padded box on the floor beneath the assembly from which it was recovered and stored.

The passage of fuel elements into and out of UCX-II was similar, except that all the necessary operations were controlled remotely by a process computer. A set of motor-driven rams (Fig. 1.2) operating in conjunction with an elevator arrangement was available for injecting the elements into preselected channels. A conveyor system transported the elements through the radiation shields, and a system of gas locks provided access while the reactor was pressurized. Thus, loading in UCX-II could be performed with the reactor critical at substantial powers. In contrast, UCX-I could be loaded only while the assembly was shut down to a low multiplication by the insertion of control rods.

Two types of control rods of distinctly different design are used in UHTREX (UCX-II). One type of rod (Fig. 2.6), which is designed for the high temperature control of the reactor, contains boron carbide (B_4C) compressed to 97% theoretical density to form hollow cylinders 0.875 in. o.d. x 0.410 in. i.d. x 2 in. long. The cylinders are supported by a central niobium rod and an outer niobium tube. Eight of these control rods are arranged in a ring of diameter 16.25 in. in 2.5-in.-diam holes bored vertically through the stationary central plug.

The second type of rod (Fig. 2.7), which is designed for low-temperature service to provide shutdown margin, contains a joined series of 1-7/16-in.-diam stainless steel segments borated to 1 wt% with ^{10}B. Four of these articulated rods reside equally spaced in a ring of 47 in. diam in 2.5-in.-diam holes passing vertically through the core annulus. A rod hole is situated midway between each pair of adjacent vertical rows of fuel channels such that there are 24 holes in all. The

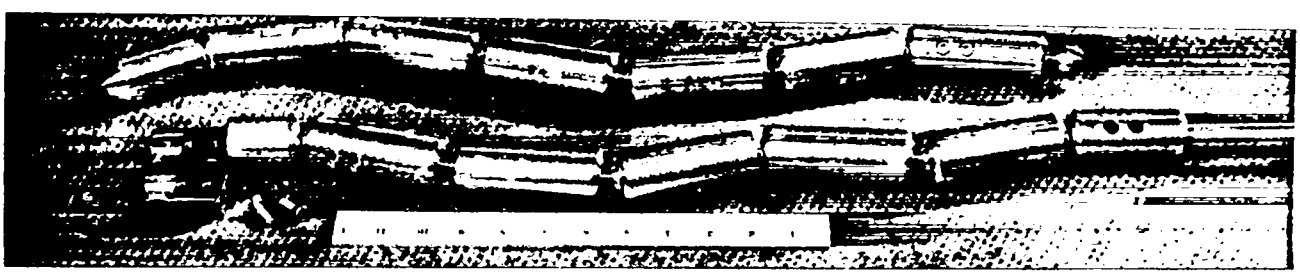

Fig. 2.7. Core control rod.

combination of closely spaced rod holes and segmented rods permits insertion of the rods for any rotational position of the core.

In UCX-I, the active material in both types of rods was contained in aluminum tubes. The B_4C cylinders of the plug rods were held in 1-1/4-in.-o.d. x 1/8-in.-wall tubing, and the borated steel segments of the core rods were contained in 3/4-in.-o.d. x 1/8-in.-wall tubing.

The active lengths of the plug and core rods were 40 in. and 39.5 in., respectively, which are roughly equivalent to the 39 in. effective height of the core. Rod positions were defined in terms of inches of withdrawal upwards with 0 in. withdrawal (full insertion) implying that the lower ends of the rods were situated at the bottom of the core (1.5 in. below center axis of a bottom fuel channel).

A ^{239}Pu-Be source of strength 1.0×10^6 neutrons/sec was positioned in the source hole (Fig. 1.2) in the center of the reactor during the initial loading approaches to critical in both assemblies. A ^{238}Pu-Be source yielding 1.25×10^8 neutrons/sec was placed external to the vessel in UCX-II to test the efficacy of an external startup source. Toward the end of the UCX-II experiments, a 1.3×10^7 neutrons/sec source was attached to the lower end of a plug rod. The last source, which is designed for use at high temperatures in UHTREX became the permanent startup source.[11]

The nuclear instrumentation used on both assemblies was conventional.

2.2 Critical Approaches and Loading Procedures

The fuel loading increments used in the approaches to critical in UCX-I and UCX-II are listed in Tables 2.2 and 2.3, respectively. The fuel element positions in the core are identified by the indices I, J, and K. These indices identify, respectively, the four radial positions of elements within a channel, the 13 vertical positions of channels, and the 24 rotational positions of channels. The

TABLE 2.2

LOADING INCREMENTS IN UCX-I

Increment Number	Element Load (g U)	Vertical Channel Position J	Rotational Channel Position K	No. of Elements in Increment	Mass Increment (g)	Total Mass (g)
0[a]	0.00	1-13	1-24	1248	0.0	0.0
1	3.54	odd	odd	84	297.3	297.3
2	3.54	even	even	72	254.8	552.1
3	4.16	odd	odd	84	349.4	901.5
4	4.16	even	even	72	299.5	1201.0
5	4.82	odd	odd	84	405.0	1606.1
6	4.82	even	even	72	347.2	1953.3
7	5.67	odd	odd	84	476.4	2429.7
8	5.67	even	even	72	408.4	2838.1
9	3.54	odd	even	84	297.3	3135.4
10	3.54	even	odd	72	254.8	3390.2
11	4.16	odd	even	84	349.4	3739.6
12	4.16	even	odd	72	299.5	4039.1
13	4.82	odd	even	84	405.0	4444.2
14	4.82	even	odd	72	347.2	4791.4
15	5.67	odd	even	84	476.4	5267.8
16	5.67	even	odd	72	408.4	5676.2
17	6.57	odd	odd	84	254.6	5930.8
18	↓	even	even	36	109.1	6039.9
19		even	↓	36	109.1	6149.0
20		odd		42	127.3	6276.3
21		odd		42	127.3	6403.6
22		even	odd	12	36.4	6440.0
23		↓	↓	↓	↓	6476.4
24[b]						6512.8

[a] Fuel channels filled with dummy elements.

[b] Reactor critical with all rods completely withdrawn.

TABLE 2.3

LOADING INCREMENTS IN UCX-II

Increment Number	Element Load (g U)	Vertical Channel Position J	Rotational Channel Position K	No. of Elements in Increment	Mass Increment (g)	Total Mass (g)
0[a]	0.00	1-13	1-24	1248	0.0	0.0
1	3.54		1-24	312	1104.2	1104.2
2	4.16		even	156	649.0	1753.1
3	4.16		odd		649.0	2402.1
4	4.82		even		752.2	3154.3
5	4.82		odd		752.2	3906.5
6	5.67		1,5,9,13 17,21	78	442.4	4349.0
7			3,7,11,15 19,23			4791.4
8			2,6,10,14 18,22			5233.8
9			4,12,20	39	221.2	5455.0
10			8,16,24		221.2	5676.2
11	6.57		2,14,22		118.2	5794.4
12			6,10,18			5912.6
13			4,12,20			6030.8
14		odd	8,16,24	21	63.6	6094.5
15		even	8,16,24	18	54.5	6149.0
16		odd	3,11,19	21	63.6	6212.7
17		even	3,11,19	18	54.5	6267.3
18A		odd	15	7	21.2	6288.5
18B[b]		odd	23	7	21.2	6309.7

[a] Fuel channels filled with dummy elements.

[b] Reactor critical with all rods completely withdrawn, except one plug rod at 41.4-in. withdrawal. Residual worth of this rod was 20.7¢. This gives an extrapolated "all rods out" critical mass of 6.277 kg with the reactor under 1 atm air.

innermost element in a channel is indicated by I = 1, a bottom channel is indicated by J = 1, and, because of the rotational symmetry of the core, the plane K = 1 was selected arbitrarily.

The objective of the loading schemes of Tables 2.2 and 2.3 was to achieve criticality with a vertically and rotationally symmetric fuel element array. It was necessary, therefore, that the loading increments meet these symmetry requirements, not only to achieve a final symmetric loading, but to obtain, during the loading approaches to critical, the smooth inverse count curves shown in Figs. 2.8 and 2.9.

In both UCX-I and UCX-II, the core was loaded initially with dummy elements (0th increment in Tables 2.2 and 2.3) which were identical to the loaded elements except that they contained no fuel. The loading operations were performed with a 10^6 neutrons/sec source in the source hole (Fig. 1.2). Since the first critical approach was performed in UCX-I, smaller loading increments were used than those adopted for UCX-II. This was accomplished by loading only alternate channels initially, i.e., those channels for which J and K are both even or both odd. These channels were loaded sequentially

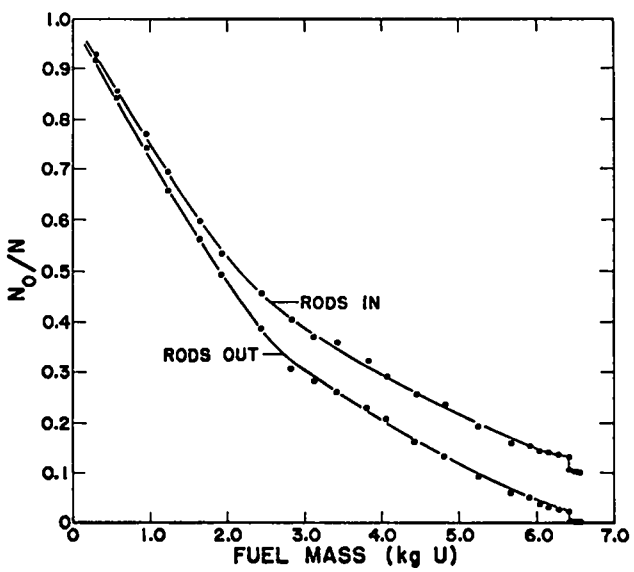

Fig. 2.8. Inverse count vs fuel loading in UCX-I.

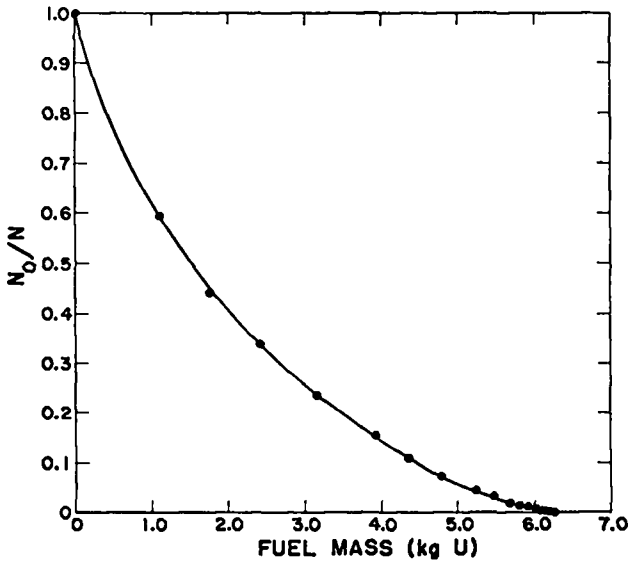

Fig. 2.9. Inverse count vs fuel loading in UCX-II.

with elements containing 3.54, 4.16, 4.82, and 5.67 g. Next, the remaining channels were loaded with the same sequence of elements. The change from one set of channels to the other in this method of loading produced the change in slope seen in the inverse count curves at 2.8 kg in Fig. 2.8.

After 6.4 kg had been loaded in UCX-I, graphite filler rods were inserted in the 24 core rod holes to facilitate measurement of the worth of these voids. The insertion of the graphite rods caused the displacement of the inverse count rates to lower values at 6.4 kg in Fig. 2.8.

Since UCX-I was loaded manually with the fuel loader tool (Fig. 2.5), it was necessary to insert the five plug rods in order to ensure a large shutdown margin during loading. In UCX-II, however, the remote loading facilities permitted loading of fuel with all control rods withdrawn. Under these conditions, continuous monitoring of the multiplication was possible. Thus, the points plotted in Fig. 2.9, which represent only the symmetric loadings of Table 2.3, are only a small fraction of the data actually taken.

After increment 16 was loaded in UCX-I or increment 10 was loaded in UCX-II, all channels contained loaded elements in all four radial positions. Subsequent loadings, therefore, caused the expulsion of loaded elements from the core. As further new elements were loaded, the channel loadings changed according to the sequence in Table 2.4. The fuel elements were loaded according to the prescription f, xf, x^2f, etc., where x = 1.17.

TABLE 2.4

CHANNEL LOADINGS

Channel Loading Sequence	Fuel Element Loadings in Channel (g U)				Total Channel Loading (g U)
	I = 1	I = 2	I = 3	I = 4	
c	3.54	4.16	4.82	5.67	18.19
xc	4.16	4.82	5.67	6.57	21.22
x^2c	4.82	5.67	6.57	7.65	24.71
x^3c	5.67	6.57	7.65	8.93	28.82
x^4c	6.57	7.65	8.93	10.48	33.63
x^5c	7.65	8.93	10.48	12.08	39.14

Channel loadings followed the same type of sequence. For the first channel loading in Table 2.4, the total mass of uranium in the four elements is $c = f + xf + x^2f + x^3f$. When an element containing x^4f is inserted into a channel that contains $c = f + xf + x^2f + x^3f$ the innermost element, f, drops out of the core, and the new channel loading becomes $xf + x^2f + x^3f + x^4f = x(f + xf + x^2f + x^3f) = xc$, the second channel loading in Table 2.4. Subsequent channel loadings are produced similarly.

As is noted in Tables 2.2 and 2.3, the initial critical masses in UCX-I and UCX-II were 6.513 and 6.277 kg, respectively.

2.3 Power and Flux Profile Measurements

Data on the power and flux profiles were gathered from direct gamma counting of fuel elements and from beta and gamma counting of uranium-aluminum (U-Al) wires. The gamma counts of the fuel elements were used primarily to determine the relative fuel element powers in a given core loading. To normalize these relative power data, absolute fission rates of a few elements were measured by radiochemical techniques. The wire data were used primarily to study localized variations in the fission flux, i.e., the flux of neutrons causing fission. In particular, wire count data were used in measurements of flux profiles through the moderator and fuel, and in detailed examinations of the fission flux variation in the fuel radially along a fuel channel. Both the wire and fuel element scans were fission flux measurements, since in both cases the radiations observed were from uranium

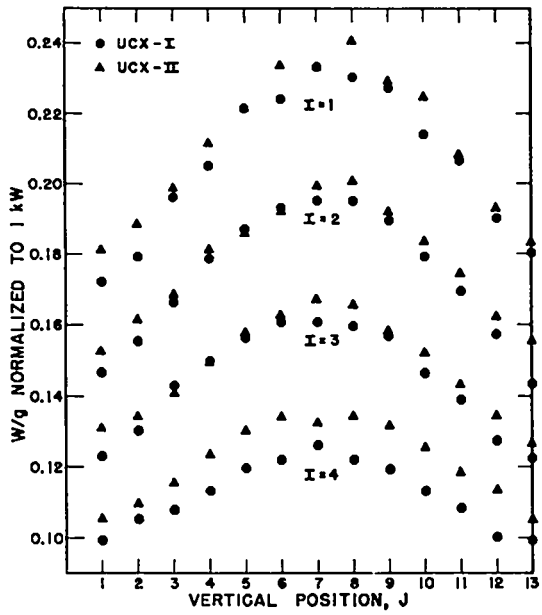

Fig. 2.10. Specific power profiles in UCX-I and UCX-II.

fission products. Since about 96% of the fissions in UHTREX are caused by thermal neutrons, the measurements are thermal flux measurements to a good approximation.

Specific power profiles observed in UCX-I and UCX-II are shown in Fig. 2.10. The gamma count of a fuel element was first normalized to 1 kW total reactor power and then divided by the mass of uranium in the fuel element to obtain the data plotted in Fig. 2.10. Since the fuel element powers are proportional to both the element fuel loadings and the flux and since the fuel loadings were varied across the core, it was essential to use specific power rather than power data to obtain flux plots.

Because of the cylindrical geometry of the core, the vertical flux plots should have a cosine shape. The vertical plots over J = 1 through 13 for each of the four radial fuel element positions I = 1 through 4 are approximately cosine in shape (Fig. 2.10).

Because of the differences in fuel loadings in UCX-I and UCX-II, the average specific power or flux in UCX-I is about 4% below that in UCX-II. The largest differences occur in the outer fuel elements (radial position I = 4) because of the different amounts of reflector material present in the two assemblies.

In the fuel element data shown in Fig. 2.10, only four points are available to define the radial flux shape at any given vertical channel position. To obtain a more detailed experimental plot of the radial flux in UCX-II, U-Al wires were irradiated at three positions in each of the four fuel elements in a channel in the vertical midplane of the core, J = 7. The wire was 10 wt% uranium and 0.02 in. in diameter. The wires were placed in holes drilled through the fuel elements perpendicular to their cylindrical axes. The points in the fuel elements for wire positions were selected to provide 12 equally spaced positions along the fuel channel. At each of the 12 positions, two wires were placed perpendicular to each other.

Results from counting these wires are shown in Fig. 2.11. The wire data are normalized to the four corresponding fuel element counts in Fig. 2.10. The radial slope in the flux obtained by wire count-

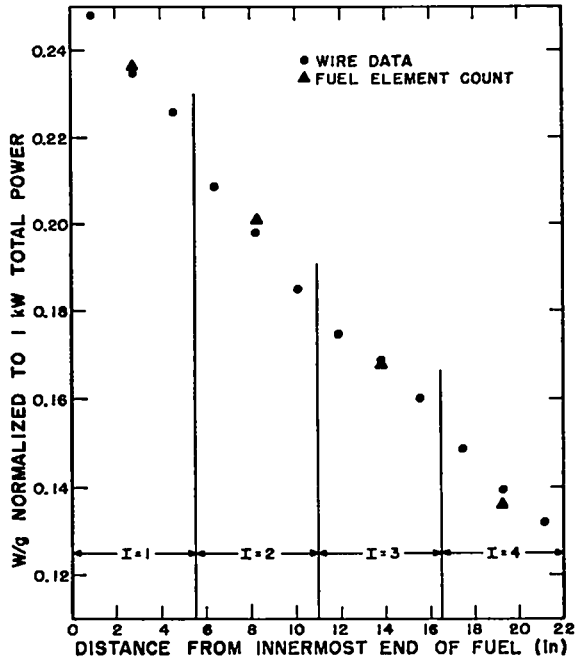

Fig. 2.11. Radial specific power profile.

ing agrees reasonably well with the slope obtained from direct counting of the fuel elements.

To determine the effects of adding thorium to fuel elements, 52 graphite fuel elements, each containing an average of 10.2 g of uranium and 102.3 g of thorium, were used in an irradiation experiment in UCX-II. The central coolant hole provided in the standard elements was omitted in the thorium elements; consequently, the thorium elements were simple 1-in.-o.d. solid cylinders 5.5-in. long.

The thorium elements were substituted for standard elements in a single K plane in the standard loading. Originally, the K plane used contained channel loading c. Since the substitution of a thorium element for a standard element on the average increased reactivity by 1.39¢, an adjustment in the standard loading was required in order to maintain criticality with all control rods withdrawn. This adjustment was made by converting the xc channel loadings in four K planes to c loadings.

The specific power profile obtained for the thorium loading and, for comparison, the profile of the standard loading are shown in Fig. 2.12. As expected, the thermal flux is considerably lower in the thorium elements than in the standard elements because of the larger amount of thermal neutron absorber in the thorium elements.

The thermal flux depressions in both standard and thorium fuel elements are shown in Fig. 2.13.

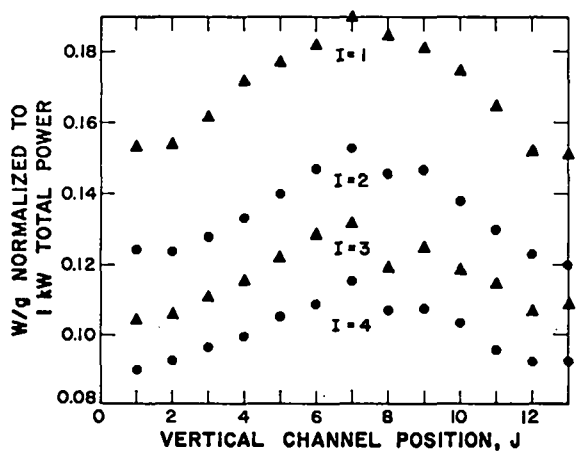

Fig. 2.12. Specific power profile in thorium loading.

For these data, U-Al wires were positioned in holes bored through the fuel perpendicular to the fuel axis. After irradiation, the wires were cut into 0.05-in. segments for counting. Because of the small variation in the fuel flux in the standard elements, counts from 16 wire segments were averaged to obtain each point. For both types of fuel, the wires were irradiated in channels in the vertical midplane, J = 7.

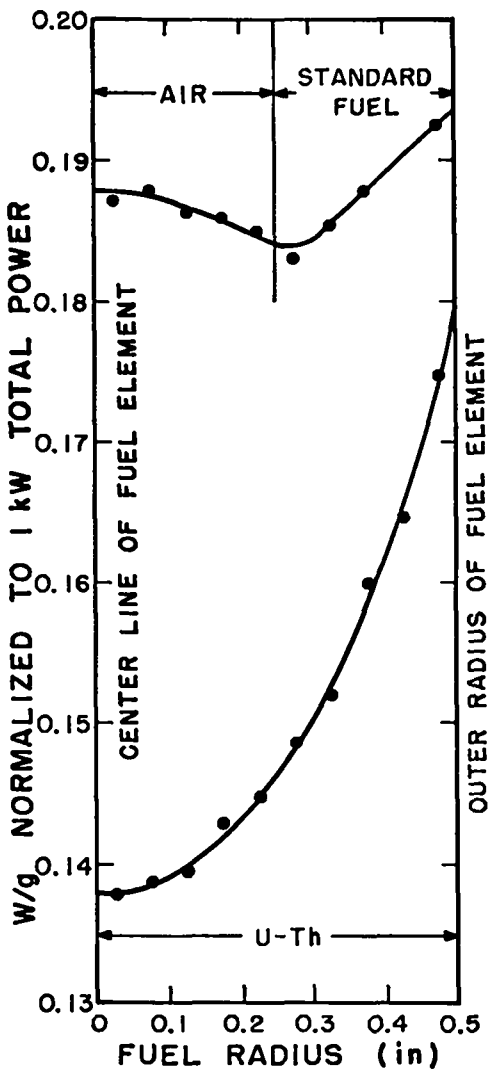

Fig. 2.13. Flux in standard and thorium fuel elements.

In the standard fuel, the rise in flux in the central coolant hole illustrates the focusing of neutrons in central voids in cylindrical or spherical fuel pieces. The effect of air in the coolant hole on the flux shape is negligible. The focusing effect is explained in Sec. 3.3.

2.4 Source Studies

Several neutron source experiments were conducted in UCX-I and UCX-II to investigate source and detector configurations for use in the high-temperature operation of UHTREX. Experiments were conducted in UCX-I to investigate the practicability of a startup on the inherent source, which is mainly the few hundred neutrons produced per second in $^{13}C(\alpha,n)$ reactions induced by alpha particles from uranium decay. At a multiplication of 30,000, the counting rate from this inherent source was only about 100 counts/min. Although it would be possible to start up the reactor with this small source, the startup would be extremely slow and tedious.

In UCX-II, a study was made of the effect of source strength and location on multiplication measurements. For a central source, the effectiveness of the source is determined by its strength and the detector efficiency. If the multiplication is sufficiently high, the count rate C is directly proportional to the multiplication M, $C = aM$, where a provides a measure of the source-detector effectiveness. For noncentral sources, however, some source neutrons will escape the core without being multiplied. At high multiplications, a linear relationship between count rate and multiplication is then observed, $C = aM + b$, where b is a constant background term.

Some results of UCX-II tests of the effect of source strength and locations on multiplication measurements are shown in Fig. 2.14. For these experiments, sources S_1 and S_2 emitting, respectively, 1.0×10^6 and 1.25×10^8 neutrons/sec were used. For the two curves marked "S_2 external" and "S_2 external (shielded)," the stronger source was situated immediately external to the vessel, and

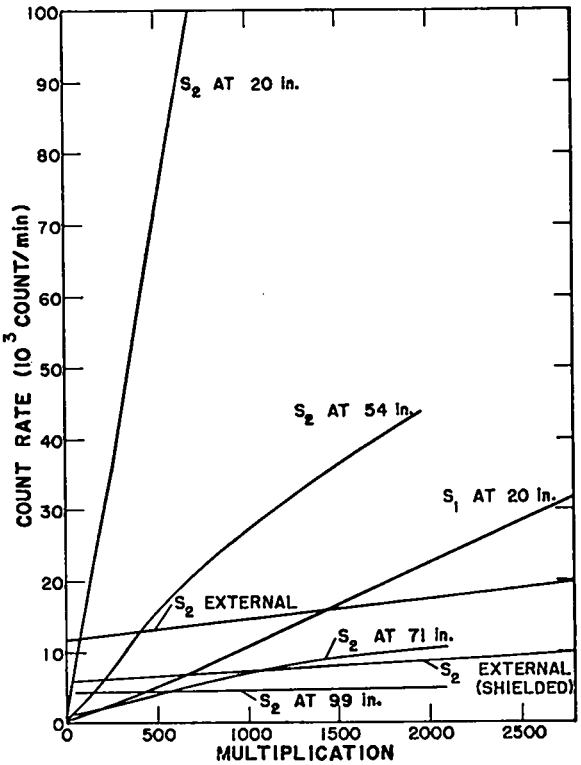

Fig. 2.14. Detector response for various source locations.

the detectors were positioned external to the vessel on the side opposite the source. The response observed from the external source was deemed unsatisfactory because of the high background and the relatively low response to multiplication changes. In the shielded case, approximately 12 in. of water surrounded by a cadmium layer was placed around the source except on the side facing the reactor core. The shielding was not significantly effective.

For the remaining curves in Fig. 2.14, the sources were positioned at the indicated elevations in the central source tube. The detectors were placed below the core. Good response is observed for both sources at 20 in., which is near the vertical center of the core. At other locations, except 54 in., the response was regarded as unsatisfactory. Values observed for a and b are given in Table 2.5.

As a result of these tests, a high-temperature source of 1.3×10^7 neutrons/sec was developed for use in the internal UHTREX environment.[11] This was attached to the lower extremity of a plug control

TABLE 2.5

SOURCE EFFECTIVENESS VERSUS POSITION

Source	Elevation (in. above core bottom)	a (counts/min)	b (counts/min)
S_1	20	10.6	≈0
S_2	20	108	≈0
S_2	54	26	600
S_2	71	5.6	1,100
S_2	99	0.3	4,300
S_2	External Unshielded	2.9	11,500
S_2	External Shielded	1.4	5,900

rod. Since motion of this rod will cause simultaneous changes in the multiplication and source effectiveness, the source rod is withdrawn to a fixed position near the top of the core for critical approaches.

Results from tests conducted with the source rod withdrawn to various positions are summarized in Table 2.6. Zero withdrawal corresponds to the source positioned near the bottom of the core, and 40 in. withdrawal corresponds to the source positioned near the top of the core. Over the range 35 to 50 in., the response is satisfactory for multiplications as low as 10.

TABLE 2.6

EFFECTIVENESS OF HIGH-TEMPERATURE SOURCE POSITIONED NEAR TOP OF CORE

Source Rod Position (in.)	a (counts/min)	b (counts/min)
35	69	<20
40	56	≈50
45	39	≈80
50	26	150

2.5 Control Rod Calibrations

The basic technique for control rod worth measurements was to increase the fuel loading as rods were inserted to maintain the reactor critical. Fuel additions were made according to the prescription described in Sec. 2.2. That is, the channel loadings were increased through the sequence of Table 2.4 as the amount of control-rod absorber in the assembly was increased. Particular fuel configurations consisted, in general, of a combination of two channel loadings differing by the factor 1.17. This difference in channel loadings produces only a small perturbation in the thermal flux. Thus, by distributing the different channel loadings symmetrically through the array of channels, a nearly constant geometry was maintained.

As fuel was added, period measurements were performed to determine the incremental fuel worths. The worths associated with incremental insertions of a control rod were then summed to obtain the reactivity worth of the rod.

Control rod positions are shown in Fig. 2.15. The rods in the plug ring are designated P1, P2, etc. Similarly, the rods in the core ring are designated C1, C2, etc. There are 24 rod holes provided in the core. This redundancy in rod holes accommodates insertion of rods into the core at any core rotational position. (See Sec. 2.1 for further discussion of this feature.)

Most of the measurements of control rod worth were performed in UCX-I. The critical masses and loading configurations for the control-rod combinations investigated are given in Table 2.7. For case 1, the critical mass was measured with the 24 core holes filled with plain graphite rods. This is the critical case described in Sec. 2.2. Case 2 gives the critical mass with the graphite rods

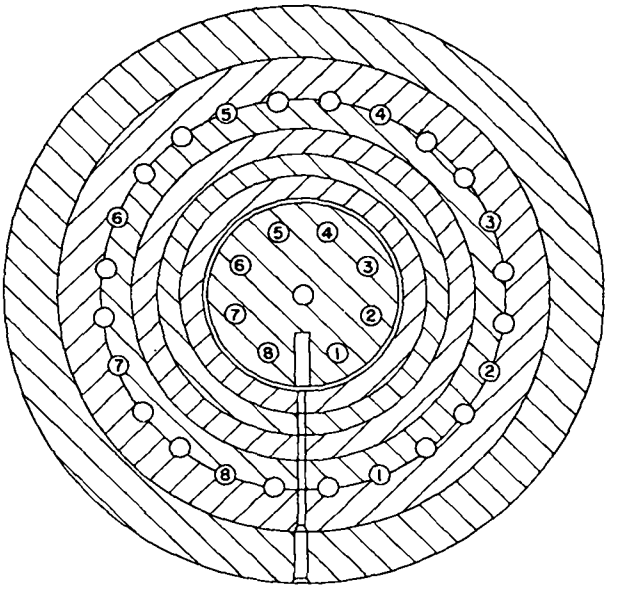

Fig. 2.15. Control rod positions in UHTREX.

TABLE 2.7

CRITICAL MASS VERSUS CONTROL ROD CONFIGURATION

Case	Control Rod Configuration	Group 1 Channels Loading	Group 1 Channels Positions Vertical	Group 1 Channels Positions Rotational	Group 2 Channels Loading	Critical Mass (g U)
1	24 core rod holes filled with graphite	c	even	1,5,9,13 17,21	xc	6,513
2	All rod holes empty	x^2c	all	2,4,8,12 14,16,20,24	xc	7,003
3	1 core rod (C1)	xc	all	5,11,23	x^2c	7,604
4	1 plug rod (P1)	x^3c	all	24	x^2c	7,813
5	2 core rods (C1 + C5)	x^3c	all	1,3,6,9,12 15,18,21,24	x^2c	8,219
6	1 plug rod + 1 core rod (P1 + C5)	x^3c	all	1,3,6,7,9 12,13,15,18 19,21,24	x^2c	8,397
7	2 plug rods (P1 + P5)	x^2c	all	2,5,8,11,14 17,20,23	x^3c	8,646
8	2 plug rods + 1 core rod (P1 + P5 + C1)	x^4c	all	12,14	x^3c	9,184
9	4 core rods (C1 + C3 + C5 + C7)	x^3c	all	2,5,8,11,14 17,20,23	x^4c	9,952
10	4 plug rods (P1 + P2 + P5 + P7)	x^3c	all	8,11,17 20,23	x^4c	10,206
11	5 plug rods (P1 + P3 + P5 + P7 + P8)	x^4c	all	all (loading = 10,470 g)	none	10,955 (extrapolated)
12	4 plug rods + 1 core rod (P1 + P3 + P5 + P7 + C1)	x^4c	all	all (loading = 10,470 g)	none	11,103 (extrapolated)

removed. A comparison of cases 1 and 2, then, shows the effect on critical mass of filling the 24 rod holes with graphite. Cases 3 through 12 show the increases in critical mass required to compensate for the insertion of various combinations of control rods.

Results for the various control rod configurations were compared to case 2 to obtain the worth of the configurations in terms of incremental mass changes. Rod worths determined by summing the worths of the mass changes as described above are shown in Fig. 2.16. Strong negative shadowing effects are observed in the plug ring, where the spatial separation between rods is small. The worths of individual rods decrease as the number of rods in the plug increases because of the increase in the thermal flux depression as the number of rods increases. There is, on the other hand, a small positive shadowing effect in the core ring, where, because of the wide separation between rod positions, the insertion of a rod at one position causes an increase in the flux at other positions.

The worths versus position of a plug rod and a core rod are shown in Fig. 2.17. For each rod, the worths were measured with all other control rods withdrawn. At zero withdrawal, the bottom end of a rod is near the bottom of the core, and at 40 in. withdrawal, the bottom of the rod is near the top of the core. At 52 in., or 1 ft above the core, rods are effectively withdrawn.

Rod calibrations in UCX-II were greatly expedited by the use of an on-line analog computer for observing reactivities. Signals from a power channel were fed into an analog circuit that simulated delayed neutron effects to provide a continuous readout of reactivity. The analog computer gave immediate indication of the reactivity; consequently, the long waiting times required for asymptotic period measurements were avoided. The partial rod calibration shown in Fig. 2.18 illustrates the fine reactivity detail available from the analog reactivity monitor.

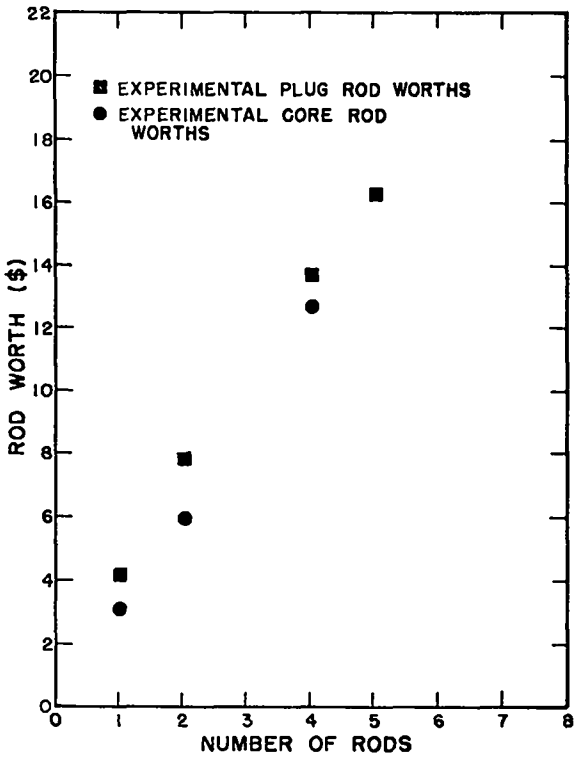

Fig. 2.16. Worths of rods in UCX-I.

2.6 Worth Measurements

Fuel Worth. In the discussion of the control-rod calibrations, it was noted that the control rods were calibrated simultaneously in terms of fuel mass worth and reactivity worth. For a given fuel loading, the rod was displaced to several positions about its critical position to determine the local reactivity versus rod position curve. By adding

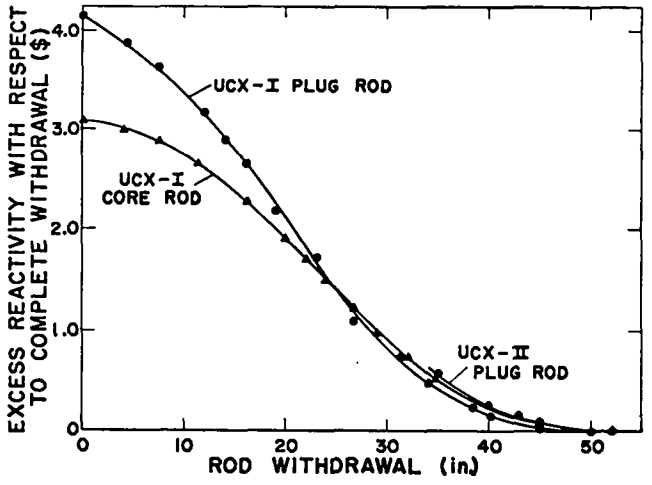

Fig. 2.17. Worth vs position of rods.

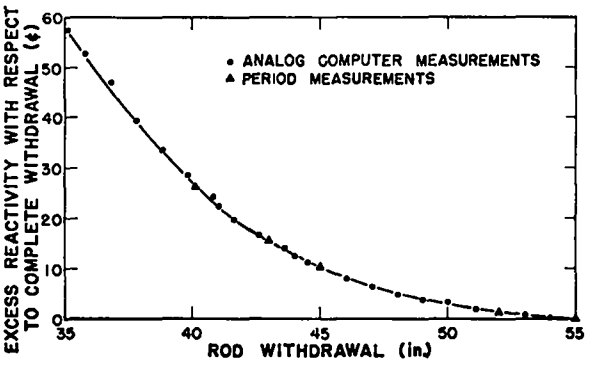

Fig. 2.18. Detail of a plug rod calibration in UCX-II.

an increment of fuel, the rod was displaced to a new critical position. The selected fuel increment was small enough to obtain an overlap with the reactivity versus rod position curves. The overlap provided both a tie point for the rod reactivity curves and a determination of the worth of the fuel increment.

In considering fuel worths, one is interested in the average effects of increasing the channel loadings in the sequence of Table 2.4. In determining average effects, the variation in the worth of fuel element insertions versus the vertical position of channels must be taken into account. In UCX-II, the worths of individual fuel elements were observed using the reactivity monitor as fuel elements were loaded while the reactor was critical. The net worths of elements are plotted against their vertical positions in Fig. 2.19.

In addition to the net worth of an element, the transient reactivity as elements were inserted was also monitored. The plot in Fig. 2.20 shows the

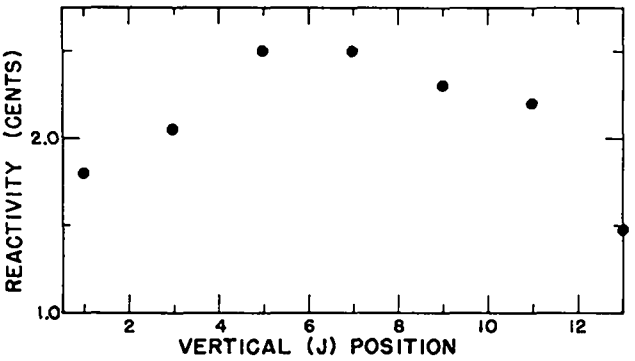

Fig. 2.19. Net worth of fuel element insertions vs vertical position of the channel loaded.

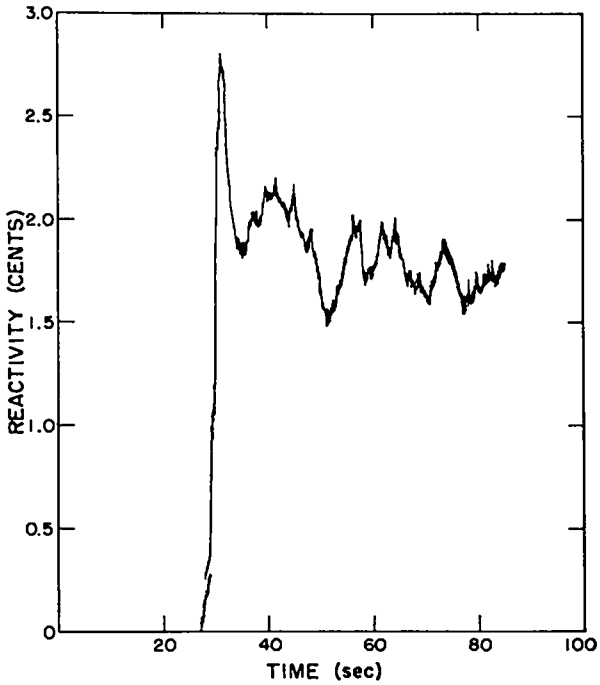

Fig. 2.20. Transient reactivity during insertion of a fuel element.

transient reactivity effects accompanying the insertion of an element into a channel at the core midheight, J = 7. At the peak in the reactivity, both the 6.57-g element being inserted and the 3.54-g element being expelled are in the core. The rapid decrease in reactivity following the peak accompanies the dropping out of the 3.54-g element.

Reactivities for various fuel element insertions are given in Table 2.8. These worths are averaged with respect to vertical channel positions. In each case, the reactor contained a combination of the two channel loadings. Thus, in the progression of UCX-I cases, the decrease in fuel worth from case to case is attributed to the overall increase in total core loading. The worth per gram in UCX-II is larger than the worth per gram for the equivalent c → xc case in UCX-I because of the smaller critical mass of UCX-II.

TABLE 2.8

AVERAGE REACTIVITIES OF FUEL ELEMENT INSERTIONS

Assembly	Loading Change	Mass Change (g)	Average Reactivity (¢/g)	Fuel Element Insertion Worth (¢)
UCX-I	c → xc	3.03	0.61	1.85
	xc → x^2c	3.60	0.52	1.87
	x^2c → x^3c	4.33	0.43	1.86
	x^3c → x^4c	4.41	0.37	1.63
UCX-II	c → xc	3.03	0.65	1.97

Void Worths. Worths of the voids in UCX-I were measured by filling the accessible holes with specially machined pieces of graphite. Measurements were made in the configuration containing no control rods (case 2, Table 2.7). The results are summarized in Table 2.9. The main purpose in measuring void worths was to test whether homogenization of the voids is adequate in the calculations (Sec. 3.4).

TABLE 2.9

WORTHS OF VOIDS IN UCX-I

Voids	Worth	
	Reactivity ($)	Fuel Mass (g)
24 core rod holes	2.74	490
16-in. exit coolant hole in radial reflector	0.56	97
Fuel loading slot	0.44	77
Cooling holes in 1248 fuel elements	0.70	121
Enlarged sections of 312 fuel channels	0.25	43

Pressure Coefficients. In conjunction with pressure tests of the vessel and coolant loop, the helium pressure coefficient of reactivity was measured in UCX-II. While the reactor power was maintained at 100 W by manipulation of the calibrated plug rod, the primary loop was pressurized in 50 psi increments to 450 psia using pure helium. At the end of each increment, the critical position of the calibrated rod was used to obtain the reactivity change.

The helium pressure coefficient of reactivity measurements are summarized in Table 2.10. The effective change in rod position due to expansion of the pressure vessel was calculated to be less than 0.03 in., which has a negligible effect on the reactivity.

TABLE 2.10

ROOM TEMPERATURE HELIUM PRESSURE REACTIVITY MEASUREMENTS

Primary Loop Pressure (psia)	Pressure Reactivity Coefficient Δρ/ΔP (¢/psi) Incremental	Cumulative
50		
100	0.068	0.068
150	0.064	0.066
200	0.050	0.061
251	0.052	0.059
300	0.054	0.058
350	0.050	0.057
400	0.056	0.056
448	0.054	0.056
475	0.056	0.056

The reactivity coefficient for the range up to 50 psia is not included in the table because the helium used to pressurize the loop to that point was contaminated with 2 vol% air. The measurements indicate that a depressurization of the system from 500 psi to 11.5 psi (Los Alamos atmosphere) would result in a reactivity loss of 28¢.

Most of the experiments in UCX-I and UCX-II were performed with the assemblies open to normal air pressure. Consequently, special experiments were conducted to assess the worth of air in the assemblies. Since it was expected that the thermal absorption cross section of nitrogen would be the principal factor determining the worth of air, the pressure coefficient of nitrogen was also measured.

Because the rod drive motors lie inside the primary containment, reference critical measurements could not be performed with a vacuum in the vessel. Consequently, the worths of air and nitrogen were measured relative to the critical configuration with helium in the reactor. The critical calibrated rod positions for helium, nitrogen, and air are listed in Table 2.11.

In order to obtain the absolute pressure coefficients for air and nitrogen, the helium reference case must be corrected to obtain an estimate of the rod worth for the void case. From Table 2.10, it is estimated that 12.9 psia of pure helium is worth +0.8¢. Mass spectrographic analysis of the helium, however, indicated it contained 1.2 vol% or 0.16 psia nitrogen. The data in Table 2.11 indicate that this amount of nitrogen is worth -1.1¢. The

TABLE 2.11

AIR AND NITROGEN WORTHS

Reactor Atmosphere	Pressure (psia)	Calibrated Rod Position[a]	Rod Worth[b] (¢)
Helium	12.9	30.0	-94.4
Air	11.5	37.0	-36.5
Nitrogen	12.9	43.0	-12.4

[a] Inches of withdrawal from full insertion.

[b] Relative to full withdrawal (55.0 in.).

net worth of the helium plus nitrogen contaminant is -0.3¢; therefore, the estimated rod worth for the void case is -94.7¢. Referring the rod worths of air and nitrogen to the void case, then, yields pressure coefficients of -5.06¢/psi and -6.38¢/psi for air and nitrogen, respectively. If it is assumed that the worth of air is determined entirely by the 78% nitrogen it contains, the air measurement would indicate a nitrogen worth of -6.49¢/psi which is in good agreement with the pure nitrogen measurement.

A Los Alamos atmosphere (11.5 psia) of air is worth 58¢ or 0.0039 Δk (for β_{eff} = 0.0068). The correction for the worth of air in comparing experimental critical masses with calculations is, therefore, non-negligible.

Temperature Coefficient. The temperature coefficient of reactivity was measured in UCX-II by operating the blower in the primary coolant loop to heat the core and reflectors. The fuel loading was adjusted to 6.289 kg so that the reactor was critical at the ambient temperature of 73°F with the calibrated plug rod at 29.74 in. of withdrawal. The available excess reactivity of 97.8¢ was then gradually consumed by the negative temperature coefficient of reactivity as the reactor was heated to about 163°F.

The reactor was heated in two stages. After 46.5¢ of the original excess reactivity was used up, the blower power was reduced until the heat input just compensated for heat losses to establish a nearly isothermal steady-state condition. At this point, the reactor temperatures and the equilibrium

rod positions were recorded. In the second stage of heating, the equilibrium was re-established with nearly all the excess reactivity (93.3¢) consumed.

Results for the two temperature plateaus are given in Table 2.12. During heating of the reactor, the helium pressure was maintained at 475 psia by venting the loop as the temperature increased. Thus, the temperature coefficient directly observed was at constant pressure, and a small fraction of the observed reactivity loss was due to a decrease in the helium density. In the last column of Table 2.12, the temperature coefficient data are corrected for the helium density changes using the data obtained earlier on helium worth.

TABLE 2.12

TEMPERATURE COEFFICIENT MEASUREMENTS

Steady-State Core Temperature (°F)	Calibrated Rod Position (in. withdrawal)	Net Loss in Reactivity (¢)	Temperature Coefficient (¢/°F)	
			Constant Pressure	Constant Helium Density
73	29.74			
118	34.87	46.5	-1.03	-0.99
163	48.44	93.3	-1.04	-1.00

The coefficients in Table 2.12 are only approximately isothermal temperature coefficients, since at the steady-state plateaus the temperature profiles were not constant, particularly in the outer reflectors. The reactor internal temperature distributions are given in Table 2.13. The temperaatures in the table were measured with 26 thermocouples distributed through the core and reflectors as shown in Fig. 2.21.

The last ten entries (channels 38 through 47) in Table 2.13 are core thermocouple readings. The readings for each plateau are constant within the experimental uncertainties. Because of heat leakage to the external vessel surface, however, the temperatures in the outer carbon layers of the reflector are markedly lower than the core temperatures. Channels 7, 17, 24, 25, 26, and 29, in particular, exhibit low readings.

Because of the high neutron leakage from the core, the neutronic importance of the reflectors is relatively large. Consequently, for accurate comparisons of calculated and experimental temperature

TABLE 2.13

REACTOR INTERNAL TEMPERATURES DURING STEADY-STATE OPERATION

Channel Number	Channel Name	First Plateau (°F)	Second Plateau (°F)
0	Helium exit #1	123	165
1	" " 2	121	167
2	" " 3	119	164
6	Core plug top	121	169
7	Carbon loader #1	87	104
14	Graphite reflector #1	117	165
15	" " 2	115	163
17	" " 4	95	130
18	" " 5	117	164
19	" " 6	117	165
24	Carbon reflector #1	85	116
25	" " 2	89	127
26	" " 3	86	116
27	Carbon top reflector #1	111	158
28	" " 2	114	162
29	" " 3	88	122
38	Core temperature #1	118	163
39	" " 2	118	163
40	" " 3	119	164
41	" " 4	117	162
42	" " 5	119	164
43	" " 6	118	163
44	" " 7	117	162
45	" " 8	118	164
46	" " 9	117	162
47	" " 10	117	162

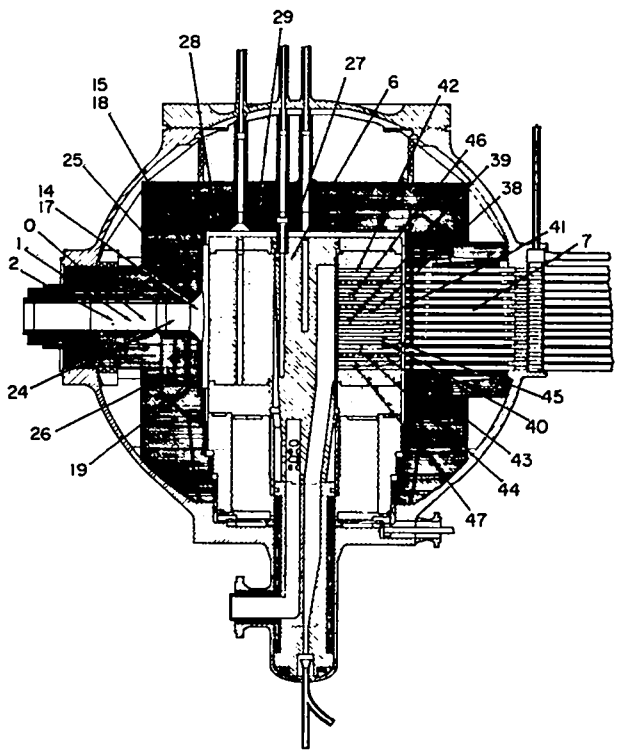

Fig. 2.21. Positions of internal thermocouples.

coefficients, the actual temperature distributions must be taken into account. This is discussed further in Sec. 3.6.

Miscellaneous Worths. A number of small reactivity effects of the order of 1 to 2¢, or less, were checked for safety reasons. The effects of core rotation and the insertion of a loading ram both were worth 1 to 2¢. Also, the residual worths of individual rods when withdrawn to 55 in. in UCX-II were of this same order of magnitude. At 55 in. of withdrawal, the bottom ends of the rods are 15 in. above the top of the core. Startup of the blower in the primary loop to its design speed produced no observable reactivity effect. The helium flow coefficient is, therefore, zero as expected.

3. CALCULATION AND INTERPRETATION OF EXPERIMENTS

3.1 Object and General Procedures

The objective of the calculations was to develop an accurate and detailed interpretation of the experiments through the application of neutron transport theory to the various critical configurations.

The steady-state neutron transport equation describes the neutron flux as a function of space, energy, and direction. Ideally this equation would be solved for the neutron flux as a continuous function of all the independent variables. In practice, however, the transport equation must be solved by numerical approximations using a limited number of discrete values of the independent variables. Thus, the continuous energy variable is replaced with a set of energy groups, the spatial variable (or variables) by a set of space intervals, and the angular variable by a set of discrete directions. Furthermore, the three-dimensional geometry of the reactor must be represented by a one- or two-dimensional coordinate system in current numerical codes. Unless the reactor composition is invariant in one direction, the reactor must be homogenized in the direction not represented by the coordinate system.

Three requirements must be met by the space, energy, and angular intervals used in the calculational model. They are

1. the number of intervals must be such that accurate results are obtained,
2. the number of intervals must be compatible with computer memory capacity, and
3. computing time required to solve the problem with the specified intervals must not be excessive.

Multigroup cross sections are derived from the continuous energy cross sections by spectrum weighting techniques. Initial calculations are made with a fine-group structure to determine the spectrum. These calculations are made in an infinite medium or, at most, in one-dimensional geometry. Once the spectrum is determined, the fine-group structure can be collapsed into a broad-group structure which is then used in the two-dimensional calculations.

Two broad-group structures were used: 25 groups and 6 groups. The six-group structure was adequate for most of the calculations. Spectrum problems and broad-group cross sections are discussed in Sec. 3.2. Since UHTREX is a thermal reactor, particular attention was devoted to the spectrum in the thermal energy range.

Figure 3.1 illustrates the general approach used to represent the UHTREX geometry in an R-Z coordinate system. Of the three options (R-Z, R-θ,

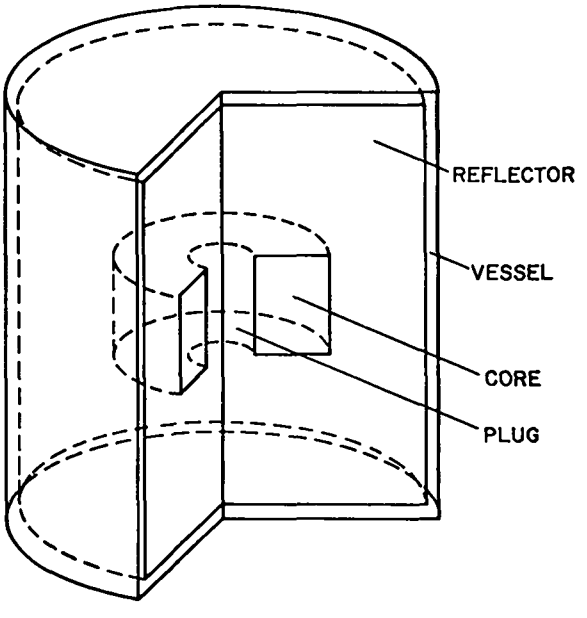

Fig. 3.1. Elementary model of UHTREX.

X-Y) available in the two-dimensional neutronic codes, the R-Z option is the most appropriate. The plug, reflectors, and core annulus are represented well in the R-Z coordinate system. However, the spherical pressure vessel and the insulating carbon surrounding the reflectors can only be approximated in this system. Also, the heterogeneous character of the core annulus cannot be represented in any two-dimensional coordinate system. Thus, cross sections used for the core in the R-Z calculations are effective cross sections which take into account the spatial self-shielding in the fuel elements. Effective cross sections for the core are derived by conventional cell homogenization techniques as discussed in Sec. 3.3.

The continuous space variable must be replaced in the numerical calculations by a suitable mesh. One-dimensional calculations in the radial and axial directions were made to determine appropriate mesh spacings. For the final calculations, an R-Z mesh containing about 1000 mesh points was found to be adequate. Detailed spatial models for UCX-I and UCX-II are discussed in Sec. 3.4.

To represent the continuous angular variable by discrete intervals, the S_n method[12,13] was used. This method is implemented in the DTF and 2DF codes.[6,7] A study of n up to n = 16 in one-dimensional models indicated that S_4 is sufficient to describe anisotropies in the angular flux. In two-dimensional geometry, no difference was observed in problems using S_4 and S_6.

The cell approach sometimes used for control rod calculations in large thermal reactors is not applicable to UHTREX, since the rods are not distributed evenly over the core, but are concentrated in two rings. Instead, two other approaches were used, one analytical and one numerical. These control rod calculational techniques are discussed in Sec. 3.5.

Reactivities due to changes in fuel loading, temperature, coolant gas composition, and other changes in reactor configuration can be computed by two-dimensional eigenvalue (k_{eff}) calculations. However, when the worths of many perturbations are required, the k_{eff} difference method requires a large investment in computing time. Furthermore, eigenvalue calculations give only the overall effect of the perturbation on k_{eff} and do not yield information on the distributed worth of the perturbation. For these reasons, reactivity worths were calculated by perturbation theory where applicable. The method used in these calculations is described in Sec. 3.6.

3.2 Microscopic Broad-Group Cross Sections - Spectrum Problems

Broad-Group Energy Structures. The 25-group structure contains 6 groups each in the fission spectrum and resonance regions, and 13 groups in the thermal region (Table 3.1). In the six-group structure, there are three groups in the fission spectrum region, two in the resonance region, and one in the thermal region (Table 3.2). Because of the long computing times required, the 25-group structure was not used routinely in two-dimensional calculations. Instead, the 25-group structure was used in a reference two-dimensional calculation to verify the adequacy of the 6-group structure, which was used in most of the two-dimensional work, and in one-dimensional calculations to study space-dependent thermalization effects.

TABLE 3.1

25-GROUP SPECIFICATIONS

Group	Energy Range			Velocity (10^8 cm/sec)	Prompt Fission Spectrum	Delayed Fission Spectrum
1	3	- ∞	MeV	28.5	0.204	0
2	1.4	- 3		19.9	0.344	0.026
3	0.9	- 1.4		14.7	0.168	0.098
4	0.4	- 0.9		11.0	0.180	0.386
5	0.1	- 0.4		6.7	0.090	0.414
6	17	-100	keV	2.70	0.014	0.076
7	3.35	- 17		1.237	0	0
8	0.454	- 3.35		0.5071		
9	61.44	-454	eV	0.1866		
10	22.6	- 61.44		0.0854		
11	8.315	- 22.6		0.0518		
12	3.056	- 8.315		0.0314		
13	1.125	- 3.056		0.0190		
14	0.425	- 1.125		0.0114		
15	0.325	- 0.425		0.00842		
16	0.250	- 0.325		0.00737		
17	0.200	- 0.250		0.00652		
18	0.150	- 0.200		0.00572		
19	0.090	- 0.150		0.00465		
20	0.055	- 0.090		0.00365		
21	0.035	- 0.055		0.00291		
22	0.025	- 0.035		0.00239		
23	0.0175	- 0.025		0.00201		
24	0.0075	- 0.0175		0.00155		
25	0	- 0.0075		0.00086		

TABLE 3.2

SIX-GROUP SPECIFICATIONS

Group	Energy Range	Velocity (10^8 cm/sec)	Prompt Fission Spectrum	Delayed Fission Spectrum
1	0.9 - ∞ MeV	18.85	0.716	0.160
2	0.4 - 0.9	11.00	0.180	0.380
3	0.017- 0.4	3.812	0.104	0.460
4	0.1 - 17 keV	0.3923	0	0
5	3.056-100 eV	0.05164	0	0
6	0 - 3.056 eV (thermal)	0.00346	0	0

With the 25-group structure as the reference case, the error in k_{eff} as a function of various reduced group structures is shown in Fig. 3.2. These calculations were done in one-dimensional geometry in the S_4 approximation. The cross sections for the reduced sets were obtained from the 25-group sets by conventional flux-weighting techniques.[14] The results in Fig. 3.2 show that the error in k_{eff} is independent of the number of thermal groups. However, the error is strongly dependent on the number of fast groups when there are less than five fast groups. For five fast groups or more, the error becomes independent of the number of fast groups. Thus, a six-group set containing five fast groups and one thermal group is a minimal set consistent with accuracy.

Fast Cross Sections. Group cross sections for the fast region (above 3 eV) were obtained from a LASL multigroup library.[15] The 24- and 16-group sets in this library contain 12 groups in the fast region--a structure fine enough that the cross sections for these groups are fairly independent of variations in the fast spectrum. Data sources and averaging schemes used to develop these group cross sections are discussed in Refs. 16 and 17.

Cross sections for the 12 fast groups of the 25-group structure were taken directly from the 25-group library. These cross sections have the fast-group energy structure shown in Table 3.1.

Cross sections for groups 1-5 of the 6-group structure were obtained by collapsing the upper 12 groups of the 16-group sets. This collapse was performed with the ZOT code,[14] using the core spectrum from a 16-group one-dimensional (cylindrical) S_4 calculation of UHTREX. Axial leakage in this calculation was represented by a DB^2 absorption term. The top 12 groups of the 16-group structure were collapsed according to the scheme 1-3, 4, 5-6, 7-9, and 10-12 in order to obtain, respecctively, groups 1, 2, 3, 4, and 5 of the 6-group structure (Table 3.2). The reasons for using this reduction scheme are that, in the 16-group structure,

1. fission in ^{238}U occurs only in groups 1-3,
2. almost 40% of the delayed fission neutrons are born in group 4,
3. groups 5-6 contain the fission neutrons not included in groups 1-4,
4. groups 7-9 contain the unresolved resonance range, and
5. groups 10-12 contain the resolved resonance range.

The reference cross sections for ^{235}U and ^{238}U taken from the library were those for infinite dilution ($\sigma_p = \infty$). However, cross sections in the resonance region (groups 7-12) were also computed with the RMITU code[17] for the proper dilution of these isotopes in UHTREX. Bell's integral formulae[18] are used in the RMITU code for group averaging of Doppler broadened resonances as a function of σ_p and temperature. The effect on k_{eff} of resonance self-shielding in ^{235}U and ^{238}U was investigated by comparing results obtained with the unshielded (infinite dilution) and the shielded

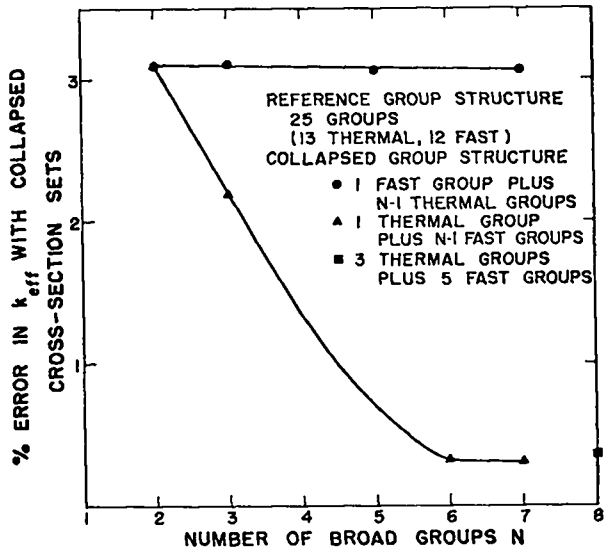

Fig. 3.2. Error in k_{eff} for various reduced-group structures.

(finite dilution) cross sections. This effect was negligible (+0.1% Δk), as expected, because of the large C/U atom ratios (about 10,000 for ^{235}U and about 160,000 for ^{238}U).

Thermal Cross Sections. Approximately 96% of the fissions in UHTREX occur in the thermal energy range (0 to 30 eV). Accordingly, special attention was devoted to the thermal neutron spectrum in deriving broad-group thermal cross sections. Briefly, the procedure for deriving microscopic cross sections for the single thermal group of the 6-group set and the 13 thermal groups of the 25-group set consisted of two steps. First, infinite medium thermal neutron spectra were computed for the reactor with a 59-group energy structure. Second, these spectra were used to collapse the 59-group thermal cross sections to the desired number of broad groups using standard flux-weighting techniques.

That the 59-group structure is adequate was indicated by comparing results with an 87-group structure. The energy structure for the 59 groups is given in Table 3.3, and the 59-group thermal cross sections are given in Appendix C. The collapsing scheme used to reduce the 59 fine groups to 13 broad groups (groups 13-25 of the 25-group set) is given in Table 3.4.

Thermalization calculations were done mostly with the SUMMIT and THERM codes.[19] Crystalline model inelastic scattering kernels for graphite are computed with SUMMIT, and the thermal infinite medium spectrum calculations and group collapsing are done with THERM. For comparison with the SUMMIT and THERM results, a few computations were also made with the recently developed LASL equivalents, the TOR[20] and GLEN[21] codes. Results of these comparisons are given in Appendix D. In general, the SUMMIT-THERM results agree well with the TOR-GLEN results.

The infinite medium thermal spectra depend both upon the temperature of the medium and the amount of thermal neutron absorber in the medium. As the temperature is increased, the average kinetic energy of the carbon atoms increases, and this energy

TABLE 3.3

59-GROUP ENERGY STRUCTURE
FOR THERMALIZATION CALCULATIONS

Group	Upper Energy Limit (eV)	Group	Upper Energy Limit (eV)
59	0.001	29	0.14
58	0.0025	28	0.15
57	0.005	27	0.16
56	0.0075	26	0.17
55	0.01	25	0.18
54	0.125	24	0.19
53	0.015	23	0.2
53	0.0175	22	0.21
51	0.02	21	0.22
50	0.0225	20	0.23
49	0.025	19	0.24
48	0.0275	18	0.25
47	0.03	17	0.275
46	0.035	16	0.3
45	0.04	15	0.325
44	0.045	14	0.35
43	0.05	13	0.375
42	0.055	12	0.4
41	0.06	11	0.425
40	0.065	10	0.45
39	0.07	9	0.5
38	0.075	8	0.6
37	0.08	7	0.75
36	0.085	6	0.9
35	0.09	5	1.125
34	0.095	4	1.5
33	0.1	3	2.0
32	0.11	2	2.5
31	0.12	1	3.056
30	0.13		

TABLE 3.4

COLLAPSING SCHEME USED
TO REDUCE 59 THERMAL GROUPS TO 13 GROUPS

Broad Group[a]	Fine Groups Included[b]
13	1 - 4
14	5 - 10
15	11 - 14
16	15 - 17
17	18 - 22
18	23 - 27
19	28 - 34
20	35 - 41
21	42 - 45
22	46 - 48
23	49 - 51
24	52 - 55
25	56 - 59

[a] Broad group numbers correspond to the 25-group set of Table 3.1.

[b] Fine group numbers correspond to the 59-group set of Table 3.3.

change is transmitted to the neutrons as they undergo scattering collisions with the speeded-up carbon atoms. This is the basic mechanism responsible for the UHTREX temperature reactivity coefficient, which is discussed further in Sec. 3.6.

Thermal neutron absorption cross sections in general vary approximately inversely with the neutron velocity. Consequently, low-energy neutrons suffer a preferential depletion due to absorption, and the average energy of the neutrons increases as the amount of absorber is increased. The effect of uranium on thermal spectra at 293°K was illustrated earlier in Fig. 1.3. The spectra progressively harden as the $C/^{235}U$ atom ratio is decreased from ∞ to 13,000 and 7520. A medium of free carbon atoms with no neutron capture would produce the Maxwellian spectrum shown.

The spectra in Fig. 1.3 cover the range of spectrum variation expected in the critical experiments with no control rods present. The spectrum for a pure graphite medium ($C/^{235}U = \infty$) shown in Fig. 1.3 was used for collapsing cross sections for the reflector and noncore regions in UHTREX. The spectra for $C/^{235}U$ = 13,000 and 7520 are the two extreme infinite medium spectra of the core in critical loadings with all control rods removed. The $C/^{235}U$ of 13,000 is obtained with a 5.67-g fuel element loaded in the outermost position in a fuel channel, and the $C/^{235}U$ of 7520 is obtained for a 4.82-g fuel element loaded in the innermost position in a channel. These $C/^{235}U$ ratios are based upon a homogenization of the fuel and moderator in the four radial core regions corresponding to the four different fuel element positions in a channel.

It was found in practice, however, that it is preferable to collapse core cross sections using the single spectrum obtained from a medium derived from homogenizing the entire core rather than using multiple spectra derived from subdividing the core as discussed above. Regions smaller than the core are too small for the thermal spectra to approach the equilibrium infinite medium spectra characteristic of the regions. A study of the effects of core subdivision on spectrum calculations is given in Appendix E.

In the core medium calculations, the 59-group thermal cross sections for the uranium isotopes were multiplied by self-shielding factors to take into account self-shielding in the coated fuel particles. The self-shielding factor for each group is determined by the macroscopic absorption cross section in the fuel particle and by the particle diameter (Appendix B). Self-shielding in the coated particles is worth -2.0% $\Delta k/k$ (Sec. 3.6).

As mentioned previously, the infinite medium thermal spectra are used to collapse the 59-group cross sections into a single broad thermal group (group 6 of the 6-group structure) or into 13 broad thermal groups (groups 13-25 of the 25-group structure). An example of results obtained for the single broad thermal group is shown in Fig. 3.3, where the absorption and fission cross sections for ^{235}U are plotted as a function of $C/^{235}U$ atom ratio.

3.3 Fuel Element Self-Shielding

Before the final calculations could be performed with the one- and two-dimensional finite reactor models, it was necessary to derive effective macroscopic cross sections which include the effect of self-shielding in the fuel elements. This was accomplished in the usual way by performing cell calculations with reflective boundary conditions to derive average multigroup fluxes in the fuel and moderator to use as weighting factors in homogenizing the cross sections. The problem of selecting

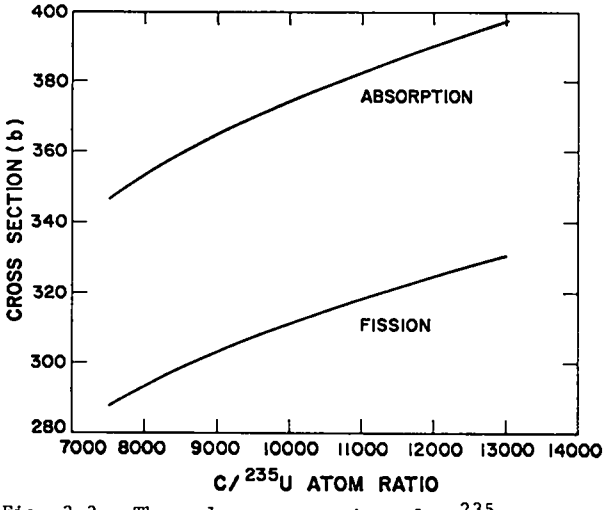

Fig. 3.3. Thermal cross sections for ^{235}U vs $C/^{235}U$ ratio.

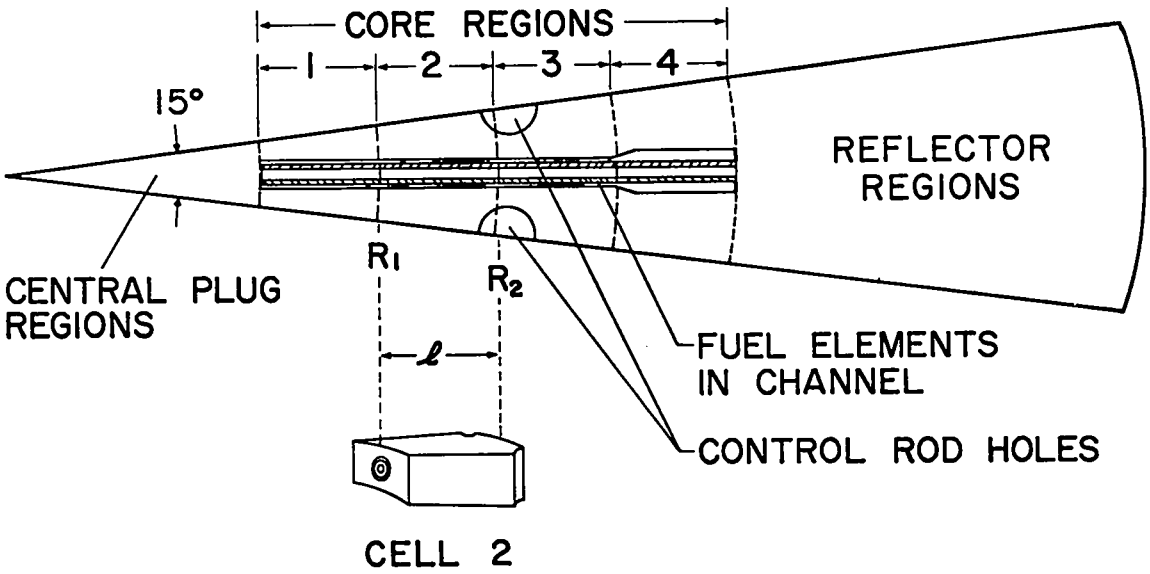

Fig. 3.4. Reactor unit cell

geometric models for cells was complicated because of the radial orientation of the fuel channels. A horizontal section of a reactor unit cell based on this configuration is shown in Fig. 3.4. If the axis of any channel is defined by the coordinates θ_0 and Z_0 in the cylindrical coordinate system of the core, then the surfaces of the reactor cell are defined by

$$\theta = \theta_0 \pm \pi/24$$

and

$$Z = Z_0 \pm h/2,$$

where h is the vertical distance (7.62 cm) between channels.

Unfortunately, the geometry shown in Fig. 3.4 is three-dimensional and not adaptable to existing neutronic codes. However, approximate one-dimensional core cells were adopted which provided adequate correction for the fuel element self-shielding. The core cells were obtained by dividing the core into four regions corresponding to the radial positions of the four fuel elements. This subdivision was made because of the different uranium loading in each of the four fuel elements in a channel. Further subdivision of the core into 12 regions to obtain fuel element self-shielding corrections made little difference in the final results (see Appendix E).

Cell Models. The basic unit for each of the four core regions contains a fuel element and associated core moderator as shown in Fig. 3.5 for core region 2. These basic units, which are referred to as cells, are not true cells in that periodic or reflective boundary conditions are not applicable at all exterior surfaces. Each cell has an angular width of 15° and is 13.97 cm long and 7.62 cm high. The fuel element actually rests on the bottom of the fuel channel, but for calculational purposes was centered in the fuel channel. The amount of moderator associated with each of the four cells increases with radial position because of the cylindrical geometry. The core control-rod holes, which are centered at a reactor radius of 59.7 cm and spaced 15° apart, are divided between cells 2 and 3. As a consequence of the fuel loading procedure discussed in Sec. 2.2, the loadings in the four fuel elements in a channel are all different, and a specific core loading contains two

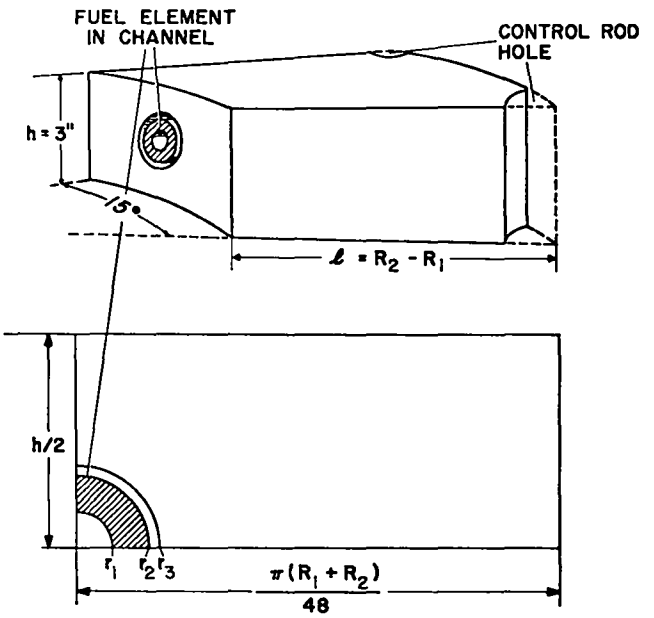

Fig. 3.5. Core cell 2.

different channel loadings. Thus, two different fuel element loadings are associated with each of the four cells, but the use of an average of these two loadings gave self-shielding factors equivalent to the average of the results for the two loadings.

Self-shielding in the fuel elements was computed with one- and two-dimensional representations of the core cells. The one-dimensional cylindrical representation is shown in Fig. 3.6. Specifications for this model are given in Table 3.5, and compositions of the fuel and moderator regions are given in Appendix F. Because of its simplicity and

TABLE 3.5

CYLINDRICAL CELL SPECIFICATIONS
(radii in cm)

	Core Region			
	1	2	3	4
Radius				
r_1	0.635	0.635	0.635	0.635
r_2	1.270	1.270	1.270	1.270
r_3	1.472	1.414	1.630	1.842
r_4	---	4.688	4.921	---
r_5	---	4.782	5.369	---
r_6	4.846	5.688	6.421	7.078
Volume fraction				
Fuel	0.0515	0.0374	0.0293	0.0241
Moderator	0.9078	0.9107	0.8237	0.9323
Void	0.0407	0.0519	0.1470	0.0436

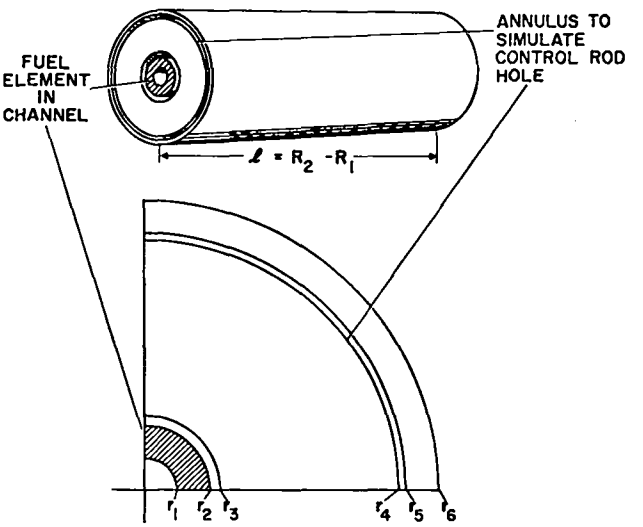

Fig. 3.6. One-dimensional cell representation.

because it yielded self-shielding in good agreement with more complicated models, the cylindrical model was adopted.

The outer radius, r_6, of the cylindrical cell model in Fig. 3.6 was calculated from

$$r_6 = \sqrt{\frac{h(R_1 + R_2)}{24}} .$$

The region between r_5 and r_4 simulated the portion of the core control rod holes in the cell. Final results were insensitive to the exact location of this void region in the cell moderator, so long as the volume fraction of the hole was preserved (see Appendix E). In the calculations, this void region was arbitrarily located 1 cm from the boundary of the cell. Radius r_3 varies from one core region to another to account for details in the fuel channel structure (Fig. 2.1), whereas r_2 and r_1 are fixed by the outer and inner diameters of the fuel element element, respectively.

In the one-dimensional cell calculations, the cells were taken to be infinite in length. The effects of identical cells in adjacent vertical and angular positions were taken into account by reflecting the outer boundary of the cell.

Results of two-dimensional cell calculations were reported previously.[22] In these investigations, X-Y geometry was used to calculate fluxes in planes perpendicular to a fuel channel axis. The

separation distances between fuel channels are different in vertical planes than in horizontal planes in the core. The X-Y calculations were performed to study the effect of these differences. In addition, R-θ geometry was used to calculate the fluxes in a horizontal plane containing a fuel channel axis. In these calculations, the variation in the horizontal separation of fuel channels as a function of radius in the core was treated. A method was developed for combining the results from the two sets of calculations based upon the assumption of flux separability in the different planes.

In general, the more complex two-dimensional approach to the cell problems produced results which were not significantly different from those obtained by the simple one-dimensional cell model. The reason is that the variation in the thermal flux, from which most of the heterogeneity effects are derived, is relatively small in the cell.

Cell Flux Distributions and Effective Cell Cross Sections. Typical flux distributions in a cylindrical cell are shown in Fig. 3.7. These results were obtained with the six-group energy structure for the innermost cell (cell 1) loaded with 4.16 g uranium. The thermal flux (group 6) is depressed in the fuel element by absorption. The flux distribution for group 4 is typical of the intermediate groups (groups 4 and 5). For these groups, the flux is flat throughout the cell because there are no fission sources and absorption is small. The flux variation in group 1 is typical of the groups in the fission source energy range (groups 1-3). Since a source for these groups is present only in the fuel element, the flux maximum is in the fuel.

The thermal flux rise in the central coolant hole is a focusing effect due to the anisotropic angular flux at the inner surface of the fuel. The angular flux entering the void is peaked along the radius because the flux in directions transverse to the radius sees more absorber than does that along the radius. An opposite effect occurs in the fission source groups, where the angular flux entering the void is peaked in the direction transverse to

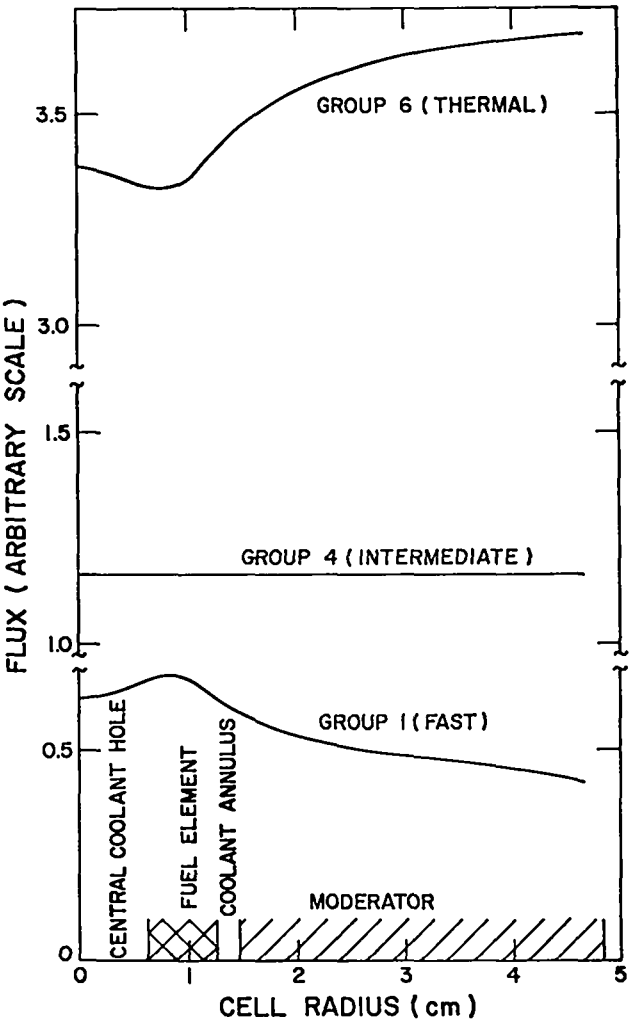

Fig. 3.7. Flux distributions in a cylindrical cell.

the radius. In the intermediate groups, where absorption in the fuel is small and there are no sources from fission, the angular flux is isotropic and the flux remains constant in the coolant hole.

Measurements of the thermal flux within a fuel element and associated core moderator were made at a reactor radius of 59.7 cm in core region 3. Results of these measurements, and of numerical calculations with the cylindrical representation of cell 3, are shown in Fig. 3.8.

Additional detail on the thermal flux variation within the fuel elements in the four radial core positions is shown in Fig. 3.9. The error bars indicate the spread in the experimental data where

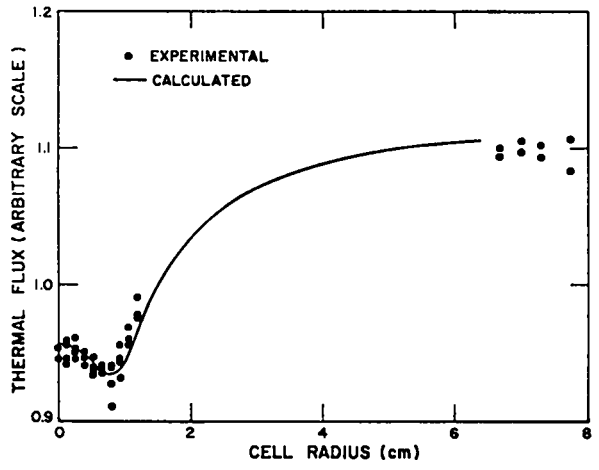

Fig. 3.8. Thermal flux variation in a fuel cell.

more than one measurement was available. Numerical results were obtained with the cylindrical representation of the four core cells containing fuel elements loaded with the appropriate uranium mass. Although the thermal flux variation within a fuel element is small, general trends are discernible in the data and support the variation expected from the numerical calculations.

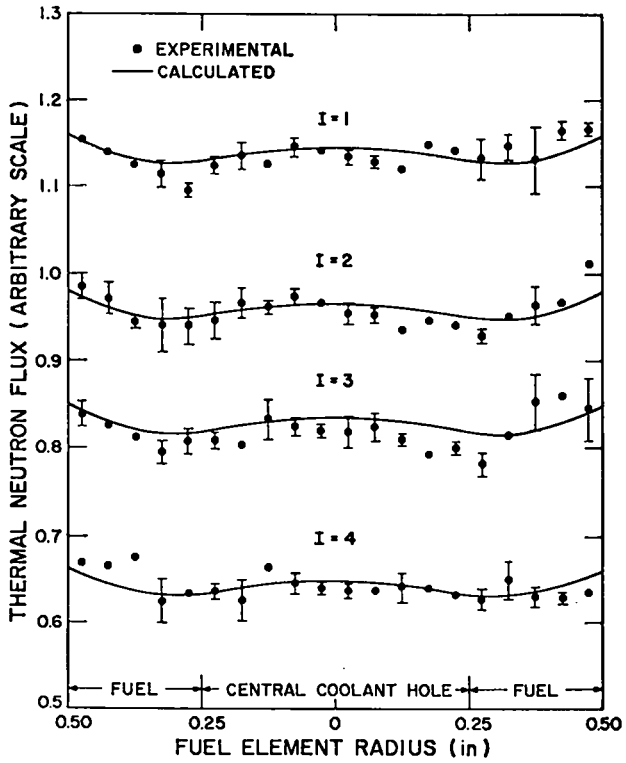

Fig. 3.9. Thermal flux variation within four fuel elements in a channel.

Fluxes obtained from the cell calculations were used to derive cell-averaged or effective homogenized macroscopic cross sections for the core. These effective macroscopic cross sections $\bar{\Sigma}$ were derived by requiring that interaction rates in the cell be preserved and are computed for each group g from

$$\bar{\Sigma}^g = \sum_{i=1}^{I} F_i^g \, \Sigma_i^g \tag{3.1}$$

where

$$F_i^g = \int_i \phi^g \, dV \Big/ \int_{cell} \phi^g \, dV = \left(\bar{\phi}_i^g \Big/ \bar{\phi}_c^g\right)\left(V_i/V_c\right). \tag{3.2}$$

In the above equations,

I = number of regions in the cell
Σ_i = macroscopic cross section in region i
ϕ = flux as a function of position in the cell
$\bar{\phi}_i$ = average flux in region i
$\bar{\phi}_c$ = average flux in the cell
V_i = volume of region i
V_c = volume of cell.

The cell effect is determined mainly by the self-shielding in the fuel element of the thermal flux. This is illustrated in Table 3.6, where the thermal (group 6) disadvantage factors for the fuel

TABLE 3.6

THERMAL DISADVANTAGE FACTORS FOR FUEL AND MODERATOR

Element Load (g)	Cell	$\bar{\phi}_f/\bar{\phi}_c$ (group 6)	$\bar{\phi}_m/\bar{\phi}_c$ (group 6)
3.54	1	0.9348	1.0061
4.16	1	0.9269	1.0068
4.16	2	0.9133	1.0051
4.82	2	0.9038	1.0057
4.82	3	0.9011	1.0047
5.67	3	0.8893	1.0052
5.67	4	0.8800	1.0069
6.57	4	0.8670	1.0076

$\bar{\phi}_f/\bar{\phi}_c$ and moderator $\bar{\phi}_m/\bar{\phi}_c$ are given for each of eight one-dimensional cell calculations. The thermal flux depression in the fuel element depends on the uranium loading of the fuel element, while the thermal flux rise in the moderator depends on the moderator thickness, that is, on the size of the cell. Thus, the ratios $\bar{\phi}_f/\bar{\phi}_c$ and $\bar{\phi}_m/\bar{\phi}_c$ depend on

both fuel element loading and cell size. The fuel element self-shielding was computed to be worth -3.6% Δk/k (Sec. 3.6).

3.4 Critical Mass (k_{eff}) Calculations

Reactor Models. Two-dimensional R-Z calculations of the UCX-I assembly (Fig. 1.1), in which the insulating carbon and pressure vessel were not present, were performed with the model shown in Fig. 3.10. Because there were different amounts of reflector above and below the core, the full height of the assembly was represented in the model. There are 33 regions in the model, and the core is represented by four homogeneous regions (30-33) with effective macroscopic cross sections derived in the manner described in Sec. 3.3.

The plug control-rod holes were represented by a void annulus (region 11) having the same cross-sectional area. Voids in the noncore regions which can be represented explicitly in the model, including the source hole (region 10), plug rod void annulus (region 11), top space (region 22), inlet plenum (regions 13 and 15), outlet plenum (region 26), and reflector void (region 28), are shown as shaded areas in Fig. 3.10. Those voids which cannot be represented explicitly, such as the fuel loader slot, exit coolant hole, and various other voids in the reflector and plug regions, were homogenized into adjacent regions. A space mesh consisting of 25 intervals radially and 37 intervals axially was used in the calculations.

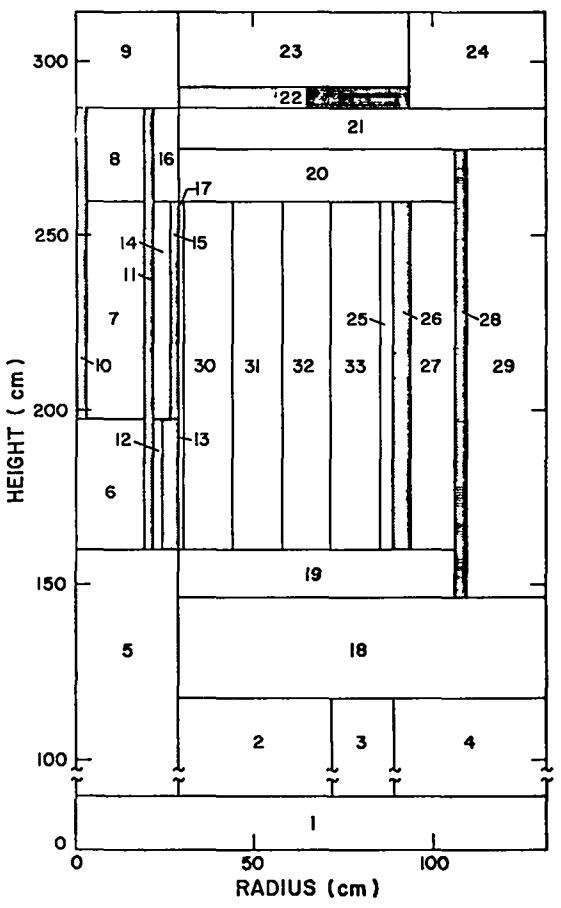

Fig. 3.10. Calculational model for UCX-I.

Elements and materials used in the neutronic calculations of the two cold critical experiments are given in Appendix F. The weight fractions of aluminum, boron, and iron in the various graphite and carbon components were determined from spectrochemical analyses of several samples from each component. Results of these analyses are given in Appendix A.

Critical mass measurements, with control rods withdrawn, were made for two different configurations in UCX-I. In the first configuration, the core control-rod holes were plugged with graphite filler rods, and the critical mass was observed to be 6.513 kg. In the second configuration, the normal configuration for UHTREX, the graphite filler rods were removed, and the critical mass was observed to be 7.003 kg. For the 6.513-kg critical load, 36 of the 312 fuel channels were loaded with 18.19 g uranium (Table 2.4). The remaining 276 channels were loaded with 21.22 g uranium. For the 7.003 kg critical load, 208 channels were loaded with 21.22 g and 104 channels with 24.82 g. Material compositions of the regions in UCX-I are given in Table 3.7.

Two-dimensional R-Z calculations of UCX-II (Fig. 1.2) were made with the reflected model shown in Fig. 3.11. Regions occupying corresponding positions above and below the midheight of the core were combined to define compositions for this model. Although UCX-II is not exactly symmetrical about the midheight of the core, the deviations from symmetry are minor and in regions of low importance. The model contains 26 regions, and the core is represented by regions 7 through 10. A 34 x 31 R-Z space mesh was used in the calculations.

TABLE 3.7

MATERIAL COMPOSITIONS OF 33 REGIONS IN UCX-I MODEL

Region	Description	Material	Volume Fraction of Material
1	Vessel	Steel	1.0000
2[a]	Lower insulator 1	Dense carbon	0.14966
		Void	0.85034
3	Core support	Dense carbon	0.88662
		Void	0.11338
4[a]	Lower insulator 2	Dense carbon	0.17507
		Void	0.82493
5	Bottom plug	Void	0.42000
		Reflector graphite	0.58000
6	Central plug 1	Void	0.11080
		Reflector graphite	0.88920
7	Central plug 2	Void	0.11320
		Reflector graphite	0.88680
8	Upper plug	Reflector graphite	1.0000
9	Dense carbon above plug	Dense carbon	0.69275
		Void	0.30725
10	Source hole	Void	1.0000
11	Plug rod annulus	Void	1.0000
12	Lower filler	Void	0.11000
		Reflector graphite	0.89000
13	Lower inlet plenum	Void	1.0000
14	Central filler	Void	0.10509
		Reflector graphite	0.89491
15	Upper inlet plenum	Void	1.0000
16	Upper filler	Reflector graphite	1.0000
17	Inner layer	Core graphite	0.82254
		Void	0.17746
18	Lower carbon reflector	Dense carbon	0.84875
		Void	0.15125
19	Lower graphite reflector	Core graphite	0.92495
		Void	0.07505
20	Top graphite reflector	Core graphite	0.92495
		Void	0.07505
21	Top carbon reflector 1	Dense carbon	0.93654
		Void	0.06346
22	Top void	Void	1.0000
23	Top carbon reflector 2	Dense carbon	0.96851
		Void	0.03149
24[a]	Corner reflector	Dense carbon	0.53772
		Void	0.46228
25	Outer layer	Core graphite	0.90000
		Void	0.10000
26	Outer plenum	Void	1.0000
27	Radial graphite reflector	Void	0.16185
		Reflector graphite	0.83815
28[b]	Reflector void	Void	1.0000
29	Radial carbon reflector	Dense carbon	0.97860
		Void	0.0214

Region	Description	Material	Volume Fraction of Material 6.51 kg	Volume Fraction of Material 7.00 kg
30	Core region 1	Fuel-1	0.11538	0.66667
		-2	0.88462	0.33333
31	2	-3	0.11538	0.66667
		-4	0.88462	0.33333
32	3	-5	0.11538	0.66667
		-6	0.88462	0.33333
33	4	-7	0.11538	0.66667
		-8	0.88462	0.33333

[a] In UCX-II, the void fractions in these regions are replaced with porous carbon.

[b] In UCX-II, this region is filled with carbon felt.

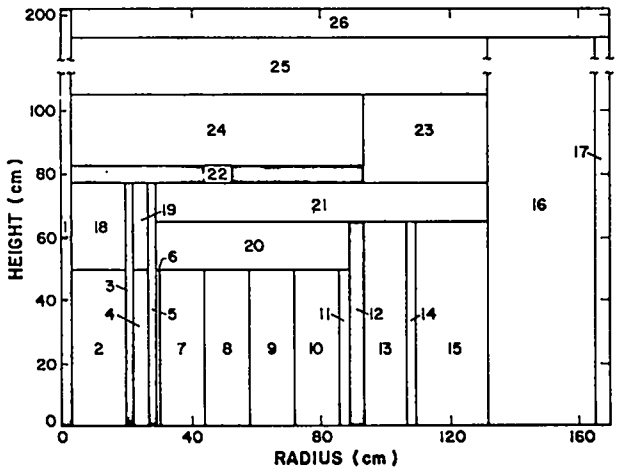

Fig. 3.11. Calculational model for UCX-II.

In the UCX-II model, the height was set equal to the diameter of the pressure vessel, and the radius was determined from conservation of volume. The effect of replacing the spherical outer surface by a right cylinder was studied by approximating the spherical boundary by steps, and the cylindrical cross section completed by specifying voids above the stepped boundaries. This model, which requires more regions and space points than the model in Fig. 3.11, did not improve the calculated results.

With the reactor open to the atmosphere, the cold critical mass for UCX-II was observed to be 6.277 kg. For this loading, 117 of the 312 fuel channels were loaded with 18.19 g uranium (Table 2.4) and the remaining 195 channels with 21.22 g. Material compositions of the regions in the UCX-II reflected model are given in Table 3.8.

The preparation of data from the models for input to the two-dimensional neutronic codes was greatly facilitated by the DPC code.[23] This code prepares the major blocks of input data cards for the neutronic codes from the specifications of the materials, configuration, and temperatures of the reactor.

Effective Multiplication Factors. Calculated effective multiplication factors for UCX-I and UCX-II are given in Table 3.9. These results were obtained from six-group S_4 calculations using the R-Z models shown in Figs. 3.10 and 3.11. Reference

TABLE 3.8

MATERIAL COMPOSITIONS OF 26 REGIONS IN UCX-II REFLECTED MODEL

Region	Description	Material M	Volume Fraction of Material
1	Source hole	Void	1.0000
2	Plug region 1	Void	0.1123
		Reflector graphite	0.8877
3	Plug rods void	Void	1.0000
4	Plug region 2	Void	0.2636
		Reflector graphite	0.7364
5	Inlet plenum	Void	1.0000
6	Inner layer	Core graphite	0.8225
		Void	0.1775
7	Core region 1	Fuel-1	0.3750
		-2	0.6250
8	Core region 2	-3	0.3750
		-4	0.6250
9	Core region 3	-5	0.3750
		-6	0.6250
10	Core region 4	-7	0.3750
		-8	0.6250
11	Outer layer	Core graphite	0.9000
		Void	0.1000
12	Outlet plenum	Void	1.0000
13	Radial reflector 1	Void	0.1618
		Reflector graphite	0.8382
14	Carbon felt	Carbon felt	1.0000
15	Radial reflector 2	Dense carbon	0.9786
		Void	0.2140
16	Radial insulation	Porous carbon	1.0000
17	Radial vessel	Steel	1.0000
18	Plug region 3	Void	0.2000
		Reflector graphite	0.8000
19	Plug region 4	Void	0.2000
		Reflector graphite	0.8000
20	Axial reflector 1	Core graphite	0.9249
		Void	0.0751
21	Axial reflector 2	Dense carbon	0.9544
		Void	0.0456
22	Axial void space	Void	1.0000
23	Corner reflector	Dense carbon	0.5138
		Porous carbon	0.4862
24	Axial reflector 3	Dense carbon	0.9420
		Void	0.0580
25	Axial insulation	Porous carbon	1.0000
26	Axial vessel	Steel	1.0000

TABLE 3.9

CALCULATED EFFECTIVE MULTIPLICATION FACTORS

Assembly	k_{eff}	Error in Critical Mass (%)
UCX-I (6.513 kg)	0.995	+2.0
UCX-I (7.003 kg)	0.998	+0.8
UCX-II (6.277 kg)	1.003	-1.0

calculations with 25 energy groups and the S_6 approximation verified the adequacy of the 6-group S_4 approach. The error in the calculted k_{eff} ranges from 0.2% to 0.5%. Using the average fuel worth for each assembly, the corresponding error in the calculated critical mass ranges from 0.8% to 2.0%, as shown in Table 3.9.

A decomposition of the calculated effective multiplication factor into $k_\infty = \varepsilon p \eta f$, which is representative of the core medium in infinite extent, and thermal and fast core nonleakage probabilities (P_{th} and P_f) are of interest. Typical values for these quantities are given in Table 3.10. The fast fission factor (ε), resonance escape probability (p), and the number of fission neutrons per thermal absorption (η) vary by less than 1% among the three configurations. Variation in the thermal utilization factor (f) is about 1% and changes with uranium loading as expected. The core thermal nonleakage probability (P_{th}) varies by about 6% among the three configurations. This variation is principally the result of additional reflection provided by the insulating carbon. The fast core nonleakage probability (P_f) varies by about 3%. This variation is mainly between the two UCX-I configurations, and results from removal of the graphite filler rods from the core control rod holes.

TABLE 3.10

INFINITE CORE MEDIUM PARAMETERS AND NONLEAKAGE PROBABILITIES

ε	1.04
p	0.95
η	2.01
f	0.90
P_{th}	0.98
P_f	0.57

The neutron economies for UCX-I (7.003 kg) and UCX-II, obtained from the two-dimensional calculations and normalized to 100 neutrons lost, are summarized in Table 3.11. The additional reflection provided by the insulating carbon in UCX-II is worth 0.726 kg of uranium, or about +3% $\Delta k/k$. Although about 32% of all neutrons produced leaked from the UCX-I assembly, only about 0.5% leaked from UCX-II, because of the increased absorption in the insulating carbon and pressure vessel in UCX-II. The pressure vessel absorbs about 21% of all neutrons produced, and the insulating carbon absorbs about 5%. In UCX-II, the calculations indicated a small (-0.3%) net leakage of thermal neutrons into the core, while in UCX-I they showed a net leakage out of 1.6%.

TABLE 3.11

NEUTRON ECONOMY FROM TWO-DIMENSIONAL, 6-GROUP, S_4 CALCULATIONS
(Normalized to total losses = 100)

	UCX-I (7.003 kg)			UCX-II (6.277 kg)		
	Reactor	Core	Reflector[a]	Reactor	Core	Reflector[a]
Absorptions						
Total	68.40	55.16	13.24	99.48	56.75	42.73
Thermal	65.38	52.20	13.18	96.73	54.10	42.63
Fast	3.02	2.96	0.06	2.75	2.65	0.10
Leakage						
Total	31.60	44.84	-13.24	0.52	43.25	-42.73
Thermal	26.77	1.62	25.15	0	- 0.34	0.34
Fast	4.83	43.22	-38.39	0.52	43.59	-43.07
Captures						
Total	---	14.38	---	---	15.14	---
Thermal	---	13.12	---	---	14.01	---
Fast	---	1.26	---	---	1.13	---
Fissions[b]						
Total	---	40.78	---	---	41.61	---
Thermal	---	39.08	---	---	40.09	---
Fast	---	1.70	---	---	1.52	---

[a] In this table, reflector means all noncore regions.
[b] Each fission produces 2.43 neutrons on the average.

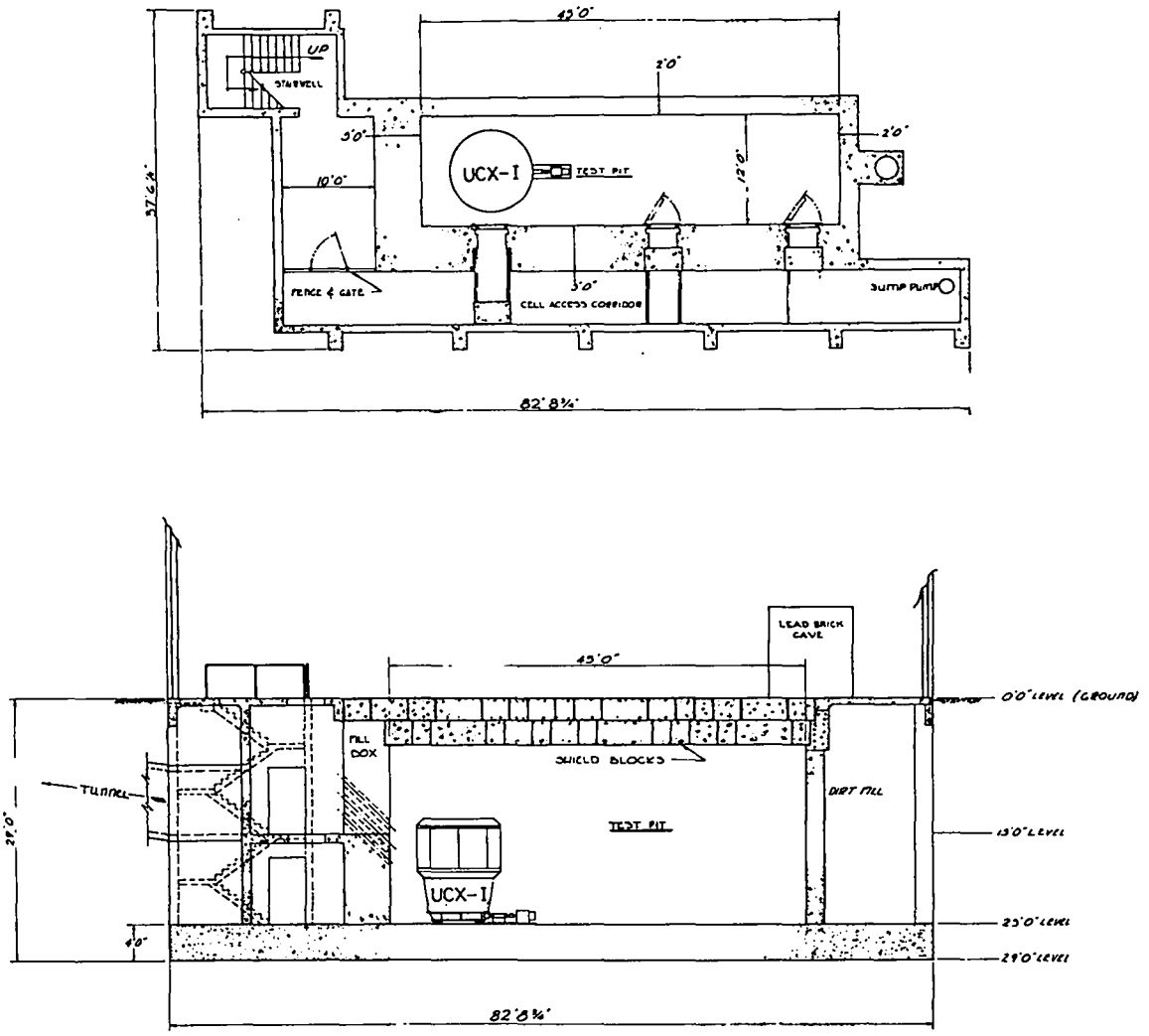

Fig. 3.12. Plan and section of UCX-I test building.

As mentioned previously, the assemblies were open to the atmosphere during the critical mass measurements. The k_{eff} calculations, however, were made for all coolant passages voided. Perturbation calculations subsequently indicated that one atmosphere of air is worth about -0.3% Δk/k. This correction was made to the calculated k_{eff} of each of the three critical configurations and is included in the values given in Table 3.9.

An additional correction of +1.0% Δk/k to the calculated k_{eff}'s for the two UCX-I critical configurations is included in the values given in Table 3.9. This correction is for the worth of the concrete walls of the test cell and is made necessary by the high leakage from the UCX-I assembly. The worth of the concrete walls is difficult to determine because of the complexity of the geometry (Fig. 3.12) and the impracticability of including the walls in the two-dimensional model. The estimate of +1.0% Δk/k was obtained from one-dimensional calculations and is reasonable because the insulating carbon, which was not present in UCX-I, is known to be worth about +3% Δk/k. This problem did not arise in the UCX-II experiment because leakage from the assembly is negligible.

Bypass flow paths through the joints in the insulating carbon bricks in UCX-II are closed by a membrane that encloses the reflector assembly. The

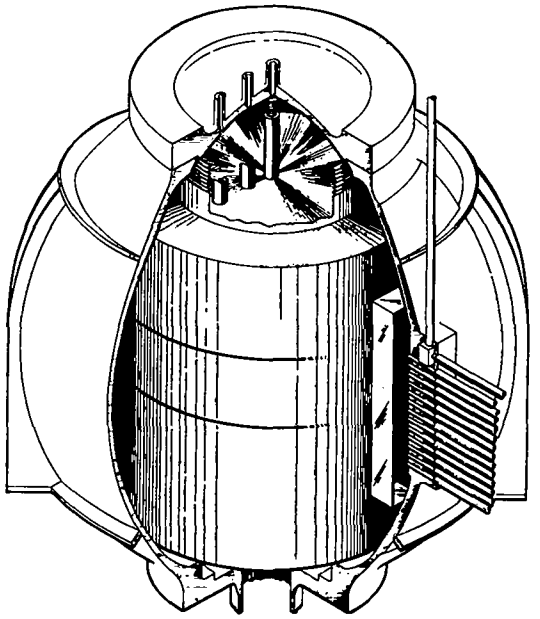

Fig. 3.13. Flow control membrane.

flow control membrane (Fig. 3.13) is a cylinder 104 in. high and 59 in. radius, made of 0.062-in.-thick Type 316 stainless steel. Because of the fine meshes required, the flow control membrane was not included in the two-dimensional model for UCX-II. An estimate of the worth of the membrane was obtained from one-dimensional calculations. These calculations indicated a worth of -0.45% Δk/k, which is included in the multiplication factor for UCX-II in Table 3.9.

It should be pointed out that the neutron economies in Table 3.11 do not contain the corrections to k_{eff} mentioned above. The concrete walls in UCX-I and the coolant control membrane in UCX-II affect mainly P_{th}, while the smaller effect of one atmosphere of air is probably on both P_{th} and f.

Worths of some voids that could not be represented explicitly in the calculational model were measured in UCX-I by filling the accessible holes with specially machined pieces of graphite. The main purpose in measuring void worths was to test whether homogenization adequately accounted for their worth. In particular, homogenization does not take into account neutron streaming out of the voids. Thus, the difference between the measured worth and the worth calculated by homogenizing the void is an indication of the importance of neutron streaming.

TABLE 3.12

VOID WORTHS[a] IN UCX-I
(% Δk/k)

Void Description	Measured	Calculated
Core control rod holes	+1.6	+1.3
Exit coolant hole and fuel loader slot	+0.64	+0.41
Fuel element holes	+0.45	+0.65

[a]Change in reactivity when the voids are filled with graphite.

Some measured and calculated void worths are given in Table 3.12. The calculated results were obtained from the difference in k_{eff} between a problem in which the void was filled with graphite and a problem in which the void was homogenized. These problems were solved in R-Z geometry (6.513-kg UCX-I configuration) using six energy groups in the S_4 approximation.

The calculated worth of the core control rod holes is about 80% of the experimental value, indicating that neutron streaming accounts for about 20% of the worth of these holes. The difference in worth between experiment and calculation is 0.003 Δk/k and accounts for the difference in the calculated k_{eff}'s for the two UCX-I critical configurations (Table 3.9).

The difference between the calculated and measured worths of the exit coolant hole and fuel loader slot implies that neutron streaming accounts for about 35% of the effect. Homogenization is not expected to adequately account for the worth of these voids because they are large and localized near the outer boundary of the assembly.

Experimental results were obtained for the fuel element holes, by inserting graphite plugs in the holes in a single column of fuel channels and observing the gain in reactivity. The gain of about 3¢ was multiplied by the number of columns to obtain the value in Table 3.12. Because a reactivity of only 3¢ is difficult to measure accurately, the

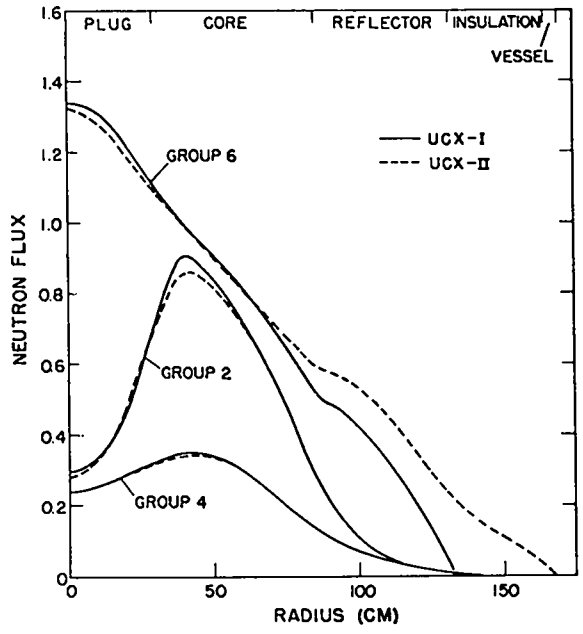

Fig. 3.14. Radial flux distributions at midheight of core. Flux units for Groups 4 and 6 are 10^{10} neutrons/cm^2-sec. Flux units for Group 2 are 10^8 neutrons/cm^2-sec.

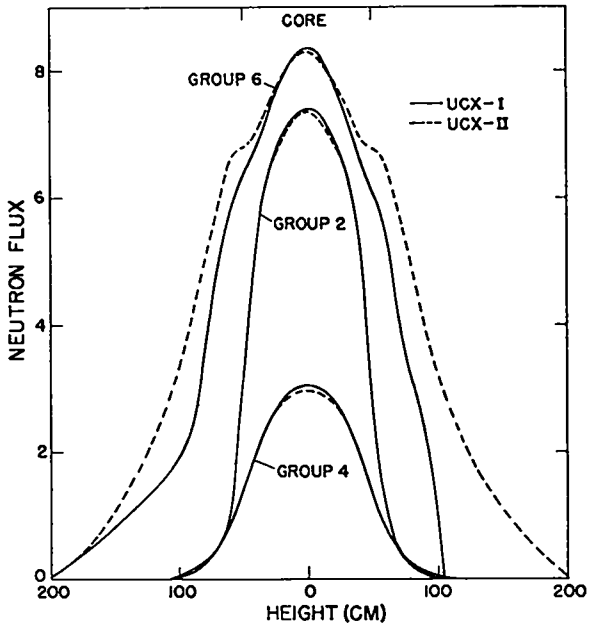

Fig. 3.15. Vertical flux distributions at mean core radius. Flux units are the same as those shown in Fig. 3.14.

experimental uncertainty probably accounts for the discrepancy between calculation and experiment. Since a fuel element coolant hole subtends a much smaller solid angle than a core control rod hole, neutron streaming effects should be small in the fuel element holes.

Flux and Power Distributions. Flux distributions calculated with the models described previously are shown in Figs. 3.14 and 3.15. Fluxes for groups 2, 4, and 6 of the 6-group energy structure are shown and are normalized to a total reactor power of 1 kW.

Radial flux distributions at the midheight of the core are given in Fig. 3.14. Outside the core and near its outer edge, the thermal flux falls off less rapidly in UCX-II than in UCX-I because of the additional reflection provided by the insulating carbon. The radial variation for group 2 is typical of the groups in the fission source energy range (groups 1-3). Because a fission source is present only in the core, the flux in these groups peaks in the core. For group 4, the variation is typical of the intermediate groups (groups 4 and 5) where sources are entirely from slowing down. The radial flux variation in these groups shows the spreading, with decreasing energy, of the slowing-down density. Note that the insulating carbon has little effect on the fast and intermediate radial flux distributions.

Vertical flux distributions at the mean radius of the core are given in Fig. 3.15. The effect of the insulating carbon on the vertical thermal flux distributions is similar to its effect on the radial distribution. As was the case with the radial distributions, the nonthermal groups have basically the same vertical distributions in UCX-I and UCX-II. In summary, the principal difference between the UCX-I and UCX-II flux distributions is that the slope of the thermal flux near the outer edges of the core is flatter in UCX-II than in UCX-I.

Measured and calculated specific power profiles for UCX-I (6.513 kg load) and UCX-II are shown in Figs. 3.16 and 3.17. In these figures, the specific power (W/g normalized to a total reactor power of 1 kW) is given for each of the fuel elements in the 13 vertical positions (J) and 4 radial positions (I) in a column of fuel elements. Because 96% of the fissions occur in the thermal group, specific power is very nearly proportional to thermal flux.

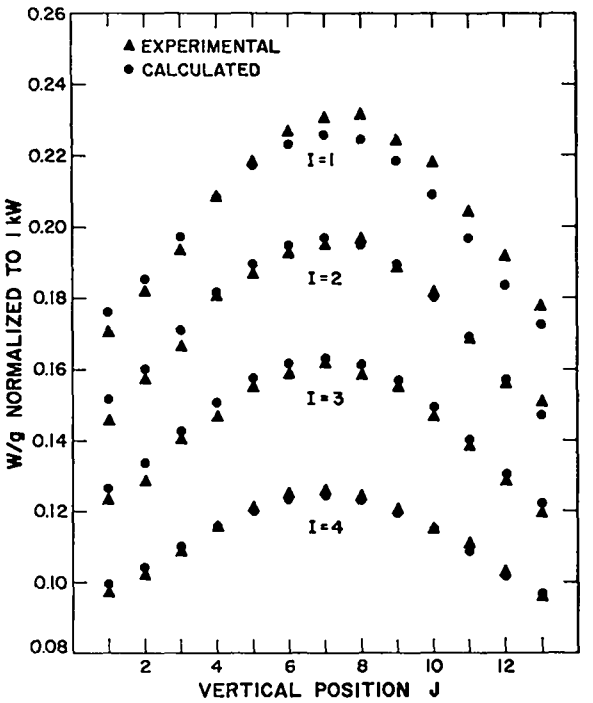

Fig. 3.16. Fuel elements specific powers in UCX-I.

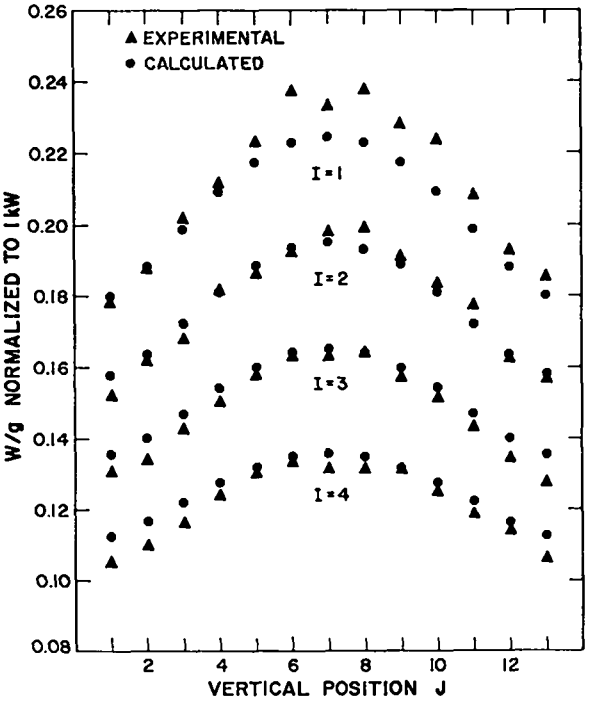

Fig. 3.17. Fuel element specific powers in UCX-II.

In Fig. 3.16, the average deviation of the calculated specific power from the experimental results in UCX-I is 1.8%. The maximum deviation is 4.3% at I = 2, J = 1. Experimental results for UCX-I were obtained from a single 1-min gross gamma count of each of the 52 elements in a column of channels. The uncertainty in the experimental results for UCX-I was estimated to be 2.2% on the average. This value includes the uncertainty in fuel loading for each fuel element and the uncertainty in the correction for decay of the gamma activity. Count rates were high enough that uncertainties due to the statistical nature of the decay process were negligible compared to the other uncertainties.

In Fig. 3.17, the average deviation of the calculated specific power from the experimental results in UCX-II is 2.7% and the maximum deviation is 7.0% at I = 4, J = 1. The experimental values are averages of three separate one-minute gross counts on each fuel element in two columns of fuel. The spread in the experimental data from the average values plotted in Fig. 3.17 is 4% on the average, with a maximum spread of 9%. Thus, the calculated results for UCX-II are within the uncertainty in the experimental data.

The UCX-II fuel elements were counted over a much longer time span (about 800 min) than the UCX-I fuel elements (about 200 min). Also, counting of the UCX-I fuel elements was started after many of the short-lived fission products had decayed, whereas counting of the UCX-II fuel elements was started sooner after the irradiation. These two factors probably account for the larger deviation of the calculated results from the experimental results in UCX-II than in UCX-I.

Additional detail on the radial specific power distributions is shown in Figs. 3.18 and 3.19. Figure 3.18 shows the calculated and experimental radial distributions for UCX-I at vertical position 8, the first position above the midheight of the core. Experimental results for UCX-I were obtained by gamma scanning along the length of the fuel elements. Good agreement between calculation and experiment is observed, as was the case in the two-dimensional distribution (Fig. 3.16).

Calculated and experimental radial distributions for UCX-II at vertical position 7 (midheight of core) are shown in Fig. 3.19. In UCX-II, a detailed radial profile was obtained with flux wires. Calculated results differ from the experimental

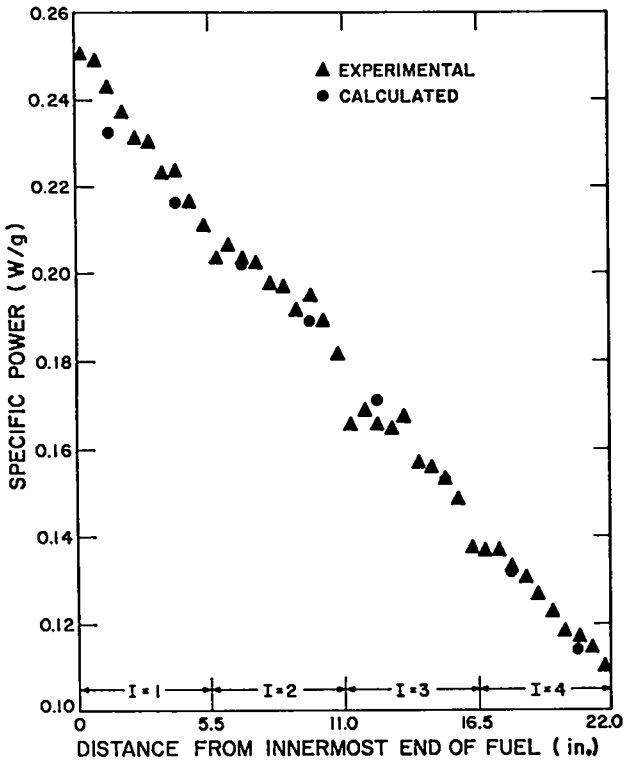

Fig. 3.18. UCX-I radial specific power profile. Vertical channel position 8.

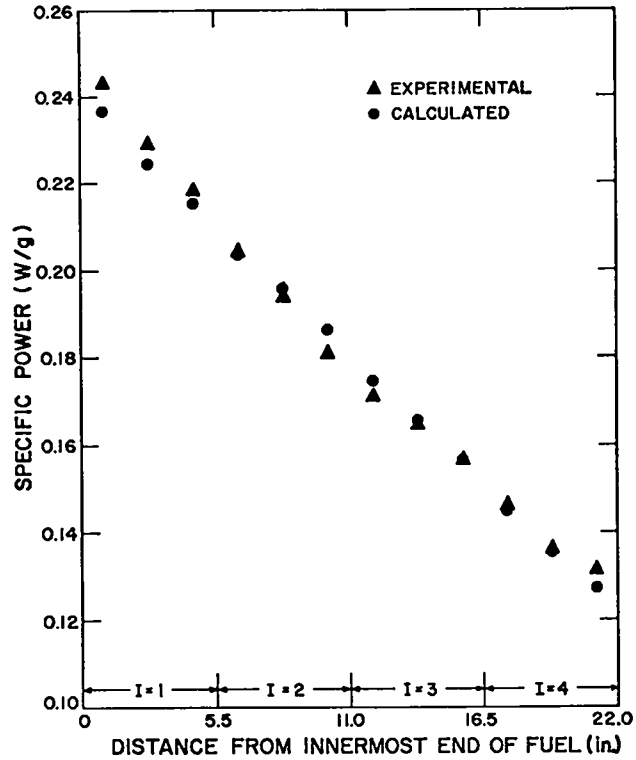

Fig. 3.19. UCX-II radial specific power profile. Vertical channel position 7.

results by 1.4% on the average, with a maximum deviation of 3.0%. This improved agreement over the gross fuel element gamma count data (Fig. 3.17) probably results from the smaller spread in the wire data. The average spread in the wire data is 2.0%, with a maximum spread of 4.4%. Thus, the calculated radial distribution for UCX-II is also within the accuracy of the wire data.

3.5 Control Rod Worths

The methods used in calculating control rod worths were reported previously.[8] An analytic method based on two-group diffusion theory was used, and the results from this method were checked by calculations with five- and six-group cross sections in two-dimensional S_n and diffusion numerical codes.

In the analytic approach, the critical determinant was solved for the case of a ring of N equally spaced rods embedded in a multiregion infinite cylinder reactor. S_n calculations were used to prepare the parameters needed as input to the analytic calculations. These parameters included the two-group extrapolation distances into the rods, the two-group cross sections, and the corrections required in the cross sections to represent leakage in the vertical direction. These two-group parameters are given in Ref. 8.

The numerical control rod calculations were performed with the R-θ options of the DDK S_n and the CRAM diffusion codes.[24,9] An off-center rod was represented by a single polar coordinate element and symmetries and reflective boundary conditions were used in the calculation of rings of control rods. Approximate corrections in the R-θ calculations for the axial neutron leakages were obtained from R-Z calculations in which the control rings were represented by equivalent annuli.

Calculated and experimental worths of the plug and core control rod rings are plotted against the number of rods in the rings in Figs. 3.20 and 3.21. In Fig. 3.20, data are plotted for two different methods of measuring rod worths: critical mass and fuel worth measurements as control rods were inserted, and rod drop experiments. Thus, the worths in

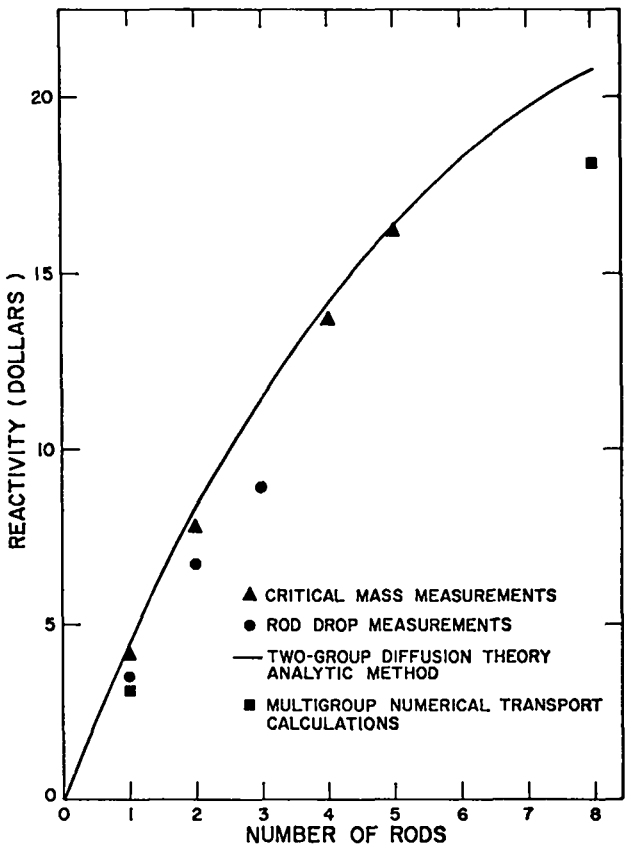

Fig. 3.20. Worths of plug rods.

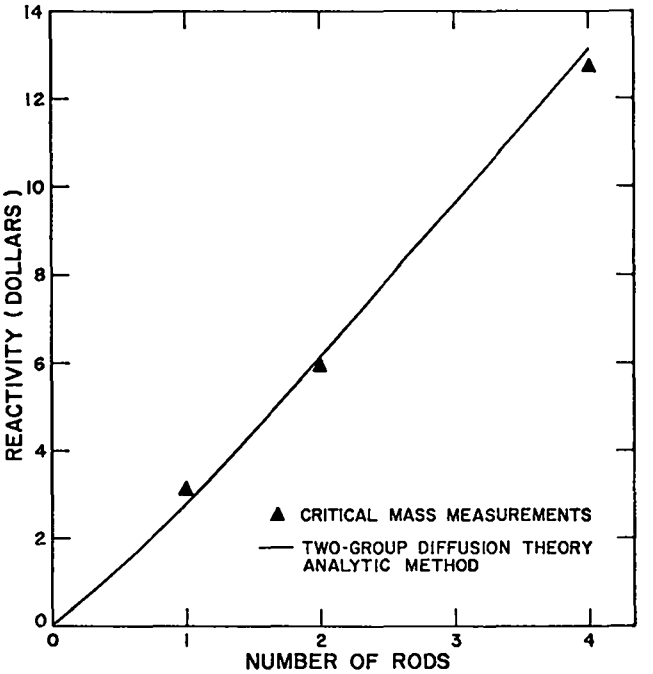

Fig. 3.21. Worths of core rods.

the first method are for an average core loading greater than the initial critical loading with all rods withdrawn, whereas the rod-drop experiments were performed in the initial critical loading. However, the discrepancy between the two methods is opposite to what would be expected from the differences in loading. Generally, the worths of black rods should decrease as the core loading increases. Of the two methods, the method based on critical mass and fuel worth measurements is deemed the more reliable; consequently, the discrepancy between the two methods, which is not considered serious, is most likely due to experimental uncertainties in the rod-drop technique.

Figure 3.20 also shows that the two-group analytic calculations agree better with the critical mass measurements than do the numerical calculations. This is probably the result of a fortuitous cancellation of errors in the two-group calculations. In the numerical studies which were conducted after the two-group calculations were completed, it was found that the worths of rod insertions near the center of the reactor are significantly affected by the change in axial leakage caused by the insertion. The differences in results from the two methods of calculation shown in Fig. 3.20 are largely due to this leakage effect which was taken into account in the numerical calculations but not in the analytic calculation.

The fractional worth of a single core rod as a function of vertical position in the core is shown in Fig. 3.22. This curve was obtained from critical mass measurements in UCX-I. The fractional worth versus vertical position computed for a symmetric ring of four core rods represented by an equivalent annulus is also shown. This curve was obtained by numerical multigroup diffusion calculations. The agreement is reasonably good considering the crudeness of the calculational model.

3.6 Perturbation Calculations

Theory. The advantage of perturbation theory is that accurate and detailed information on reactivities of perturbations is obtained with little expenditure of computing time. Only two of the time-consuming two-dimensional S_n calculations are required: a regular and an adjoint calculation of

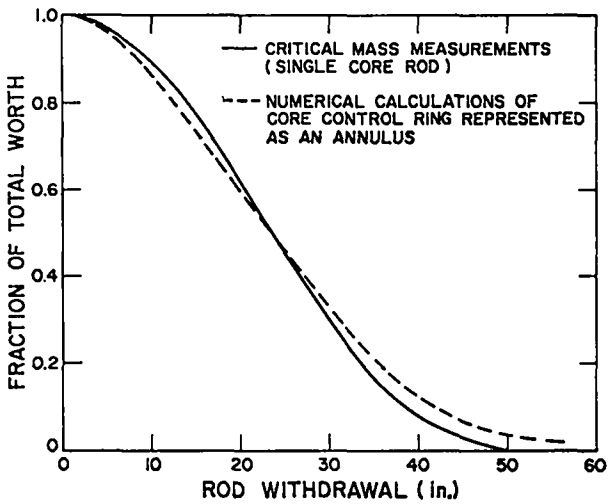

Fig. 3.22. Worth vs position of a core rod.

the unperturbed reactor. Moreover, the perturbation method supplies data on the contribution of each mesh point (and thus each region) to the overall worth of the perturbation. By the eigenvalue method, where the perturbation is evaluated by direct calculation of k_{eff}'s, only the overall effect on the system k_{eff} is obtained, and the perturbation must be large ($\approx 0.01\ \Delta k$) in order to obtain accurate values for Δk.

A two-dimensional R-Z perturbation code, the Data Analysis Code (DAC), was used in the perturbation calculations. Input to the code includes atom densities and dimensions defining the reactor model (card output from the DPC code), cross sections of the elements contained in the reactor, changes in atom densities and cross sections that define the perturbations, and two-dimensional regular and adjoint fluxes and currents from the 2DF code. The worth ρ of any perturbation which results in a change $\delta\sigma$ in macroscopic cross section is computed from

$$\rho = \frac{1}{F}\int d\vec{r}\left(\sum_{g'=1}^{G}\sum_{g=1}^{G}\phi_{g'}(\vec{r})\,\phi_{g}^{*}(\vec{r})\left|\delta\sigma_{g'g}(\vec{r})\right.\right.$$
$$\left.+\frac{1}{K}\,\delta[\nu\sigma_f(\vec{r})]_{g'}\left[(1-\beta)\,\chi_g+\sum_i \beta_i\, f_g^i\right]\right|$$
$$\left.-\sum_{g=1}^{G}[\phi_g(\vec{r})\,\phi_g^{*}(\vec{r})-3\vec{J}_g(\vec{r})\cdot\vec{J}_g^{*}(\vec{r})]\,\delta\sigma_g(\vec{r})\right) \qquad (3.3)$$

where

G = total number of groups,

$\sigma_{g'g}$ = macroscopic transfer cross section from group g' to group g,

$\nu\sigma_f^g$ = number of neutrons per fission multiplied by the macroscopic fission cross section for group g,

σ_g = macroscopic transport cross section for group g,

β_i = delayed neutron fraction for ith delayed neutron group,

χ_g = fraction of prompt fission neutrons born in group g,

f_g^i = fraction of delayed group i neutrons born in group g,

ϕ_g = regular scalar flux for group g,

ϕ_g^* = adjoint scalar flux for group g,

$\vec{J}_g$ = regular vector current for group g,

$\vec{J}_g^*$ = adjoint vector current for group g, and

K = reproduction factor.

In R-Z geometry, the vector currents consist of radial and axial components J_i and J_j with

$$\vec{J}(r,z) = \vec{i}J_i(r,z) + \vec{j}J_j(r,z) \quad , \qquad (3.4)$$

where $\vec{i}$ and $\vec{j}$ are, respectively, unit vectors in the R and Z directions. In Eq. 3.3, F is a normalization factor defined by

$$F = \frac{1}{K}\int d\vec{r}\left(\sum_{g=1}^{G}\phi_g^{*}(\vec{r})\left[(1-\beta)\,\chi_g+\sum_i\beta_i\,f_g^i\right]\cdot\sum_{g=1}^{G}\phi_g(\vec{r})[\nu\sigma_f(\vec{r})]_g\right) \quad . \qquad (3.5)$$

The current approximation to the angular flux $\psi(\vec{r},\vec{\Omega})$ was used in Eq. 3.3. This approximation is given by

$$\psi_g(\vec{r},\vec{\Omega}) = \phi_g(\vec{r}) + 3\vec{\Omega}\cdot\vec{J}_g(\vec{r})$$
$$\psi_g^{*}(\vec{r},\vec{\Omega}) = \phi_g^{*}(\vec{r}) - 3\vec{\Omega}\cdot\vec{J}_g^{*}(\vec{r}) \quad , \qquad (3.6)$$

where Ω is a unit vector in the direction of motion.

To define the perturbations, separate spectrum and cell calculations were performed with the perturbation (for example, a temperature change or material change) included. The associated cross-section perturbations were then processed by the DAC code to calculate the associated reactivities.

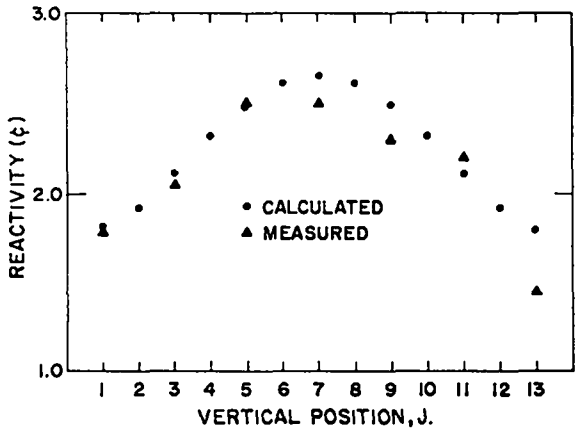

Fig. 3.23. Worths of fuel element insertions vs vertical channel position. Calculation compared to experiment.

Fluxes and currents from six-group S_4 computations of the unperturbed UCX-II assembly were used in the perturbation calculations.

Worths of Materials. The reactivity change when a fuel channel containing 18.19 g uranium (c channel) is converted into one containing 21.22 g (xc channel), is shown in Fig. 3.23. Calculated values obtained by perturbation theory are shown for the 13 vertical positions in a column of channels, whereas the experimental measurements were made for the odd vertical positions only.

From the results in Fig. 3.23, the calculated average fuel worth of converting a c channel into an xc channel in UCX-II is 0.74¢/g uranium compared to the measured average value of 0.65¢/g.

In UCX-I (6.513-kg load), the average worth of converting a column of c channels to xc channels was observed to be 0.575¢/g. Numerical calculations for this case yielded 0.598¢/g. The average fuel worth in UCX-I is less than in UCX-II because the core thermal neutron spectrum is harder in UCX-I than in UCX-II. In general, the thermal spectrum in the core becomes harder with increasing uranium load, so that the average fuel worth decreases with increasing load.

The distributed worth (¢/g) of carbon, the main constituent of UHTREX, is shown in Fig. 3.24. For a pure scatterer, the worth is positive or zero over the entire reactor. The positive reactivity

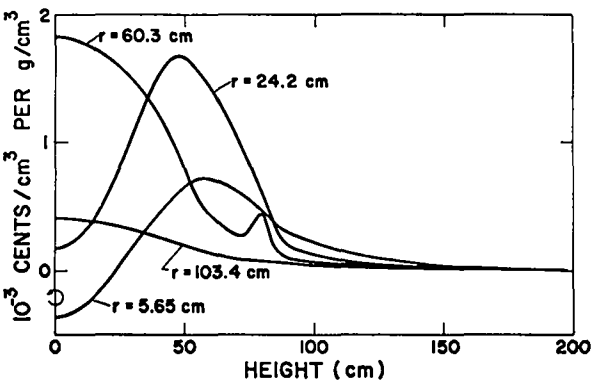

Fig. 3.24. Distributed worth of carbon in UCX-II.

effect in the core results from an increase in scattering, and outside the core it results from an increase in reflection. The worth of carbon, which is principally a scatterer, is negative only near the center of the reactor, where absorption is more important than the scattering effect (see curve for r = 5.65 cm). In general, the worth of carbon is greater in the core than in the noncore regions. The peak in the curve for r = 60.3 cm at a height of about 80 cm results from radial streaming in region 22, which is a void (see Fig. 3.11).

The distributed worth of boron, which is principally an absorber, is shown in Fig. 3.25. For a pure absorber, the worth is negative over the entire reactor. The negative reactivity effect in the core results from an increase in parasitic capture, while outside the core the additional absorption decreases the effectiveness of the reflector.

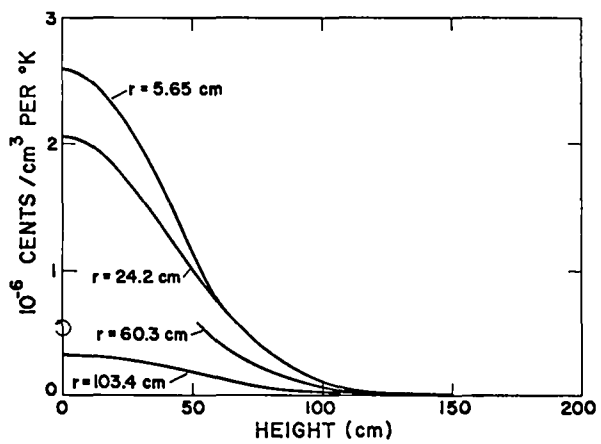

Fig. 3.25. Distributed worth of boron in UCX-II.

Because the effect of boron results from thermal absorption, the variation in worth is similar to the thermal flux distribution.

Table 3.13 gives the worth of a boron atom density of 1 x 10^{17} atoms/cm^3 in the major components of UCX-II. This concentration is equivalent to about 1 ppm boron in graphite. The multiplication factor is very sensitive to the amount of boron in the various components, particularly in the core.

TABLE 3.13

WORTH OF 1 x 10^{17} ATOMS/CM^3 OF BORON IN MAJOR COMPONENTS OF UCX-II

Component	Δk/k (%)
Plug	-0.29
Core	-1.80
Graphite reflectors	-0.19
Dense carbon reflectors	-0.39
Porous carbon	-0.14
Total	-2.81

The distributed worth of water is shown in Fig. 3.26. Because of competition between absorption and scattering effects, the worth of water is positive in some portions of the reactor and negative in other portions. In general, the worth is negative everywhere except in the inner portions of the core. Thus, the scattering effects predominate inside the core, and absorption predominates outside the core.

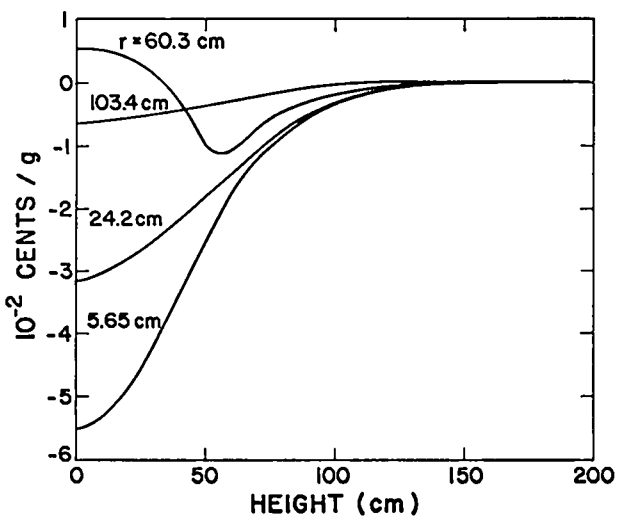

Fig. 3.26. Distributed worth of water in UCX-II.

A water density of 1 mg/cm^3 in all the graphite and carbon components was calculated to be worth -44¢ in reactivity. This density corresponds to about 32 kg of water in the reactor. Only 2.7 kg of water was removed during outgassing experiments at 400°F. This amount of water, assuming that it was uniformly distributed over the reactor, is worth about 4¢ in reactivity. Removal of any remaining moisture in the graphite and carbon components will thus add little reactivity to the reactor.

Pressure Coefficients. For the unperturbed problem, the coolant passages in the reactor were taken to be voids. The pressure coefficients given in Table 3.14 were computed by filling the reactor voids with helium, nitrogen, and air. Experimental results were obtained by observing the displacement of a calibrated control rod required to maintain criticality with the various gas atmospheres (Sec. 2.6).

TABLE 3.14

PRESSURE COEFFICIENTS (¢/psi)

Gas	Calculated	Measured
Helium	+0.025	+0.056
Nitrogen	-5.4	-6.4
Air	-4.2	-5.0

A perturbation calculation yielded a helium pressure coefficient of +0.025¢/psi, whereas the measured value was +0.056¢/psi. The distributed worth of helium exhibited, for the most part, the behavior expected for a scatterer. Reasonable uncertainties in the helium cross sections do not account for the difference between calculation and experiment. The difference might be due to the diffusion of helium into the pores of the graphite and carbon components. This effect, which is difficult to estimate, was not taken into account in the calculations. The assumption that 10 to 20% of the graphite and carbon volume is occupied by helium accounts for the difference between calculation and experiment. This assumption is reasonable because the theoretical maximum density of graphite is 2.26 g/cm^3, and the actual densities in the reactor range from 1.0 to 1.8 g/cm^3. The difference between theoretical and actual density is a measure of the pore volume in the material.

A perturbation calculation for nitrogen yielded a pressure coefficient of -5.4¢/psi, and the distributed worth was that expected for an absorber. The calculated value for nitrogen is 16% smaller than the measured value of -6.4¢/psi. As was the case with helium, the difference between the calculated and measured pressure coefficient of nitrogen can be accounted for by diffusion into the pores in the graphite and carbon components. Because of the difference in diffusion properties, however, a smaller fraction of the pores would be filled with nitrogen than with helium. This may explain why the calculated results for nitrogen agree more closely with experiment than do the results for helium.

The three principal constituents of air are nitrogen, oxygen, and argon with volume fractions, respectively, of 78, 21, and 1%. A perturbation calculation for air, with these constituents included, yielded a pressure coefficient of -4.2¢/psi. Both the calculated and measured pressure coefficients for air are 78% of the corresponding values for pure nitrogen, indicating that the nitrogen volume fraction accounts for all the pressure coefficient of air. This is an expected result since the thermal absorption cross section for nitrogen is the order of 10,000 times that for oxygen, and three times that for argon.

Temperature Coefficients. The temperature coefficients in UHTREX result from the influence of the carbon moderator temperature on the thermal neutron spectrum. This is true even for the fuel elements, where, because the uranium is both highly enriched and highly dilute, the Doppler coefficient is negligible.

Briefly, the procedure for calculating the fuel element temperature coefficient was as follows:

1. Microscopic multigroup thermal cross sections for appropriate temperatures and infinite core media were obtained with the THERM code.
2. Cell calculations were made for the unperturbed and perturbed cases with cross-section sets which included thermal cross sections derived in Step 1.
3. Cell-averaged six-group (five fast, one thermal) macroscopic cross sections for the core were derived by group- and space-collapse of the cross sections obtained in Step 1 using the flux distributions obtained in Step 2.
4. The effective six-group macroscopic cross sections for the perturbed and unperturbed cases obtained in Step 3 were then processed by the DAC code to calculate the worth of the temperature perturbation.

Even for a large perturbation in the fuel element temperature, the change in the thermal neutron spectrum in the cell is small because the moderator in the fuel element is only about 4% of the total in the cell. Thus, the cell calculations must be made with a fine thermal group structure. With 25 thermal groups, the fuel element temperature coefficient was calculated to be -1.54×10^{-5} $(\Delta k/k)/°C$ for a 100°C perturbation.

Calculation of the core temperature coefficient involved a uniform perturbation of the entire cell. For this case, a simplified approach was found to be adequate. The effect of the uniform temperature perturbation on the thermal neutron spectrum in the cell could be accounted for entirely in the infinite medium thermalization calculations. Thus, the cell calculations were made with the six-group structure containing a single broad thermal group whose cross sections included the effect of the perturbation. For a temperature perturbation of 100°C, the calculated core temperature coefficient was -1.86×10^{-4} $(\Delta k/k)/°C$. The distributed core temperature coefficient (Fig. 3.27) is similar, but opposite in sign, to the specific power and

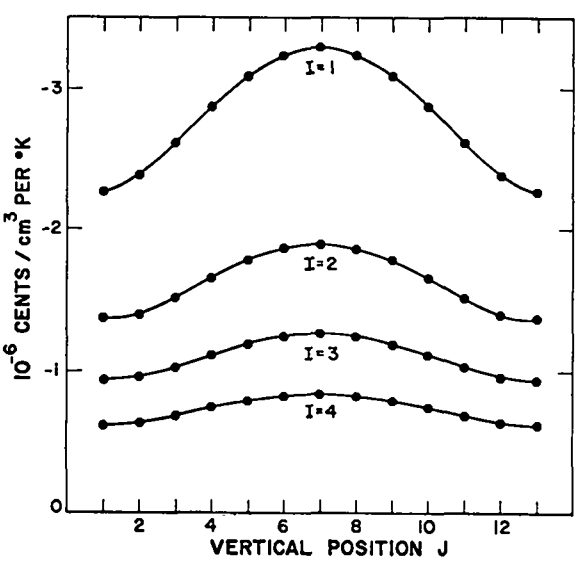

Fig. 3.27. Distributed core temperature coefficient in UCX-II.

fuel worth distributions (Figs. 3.17 and 3.23). An increase in core temperature thus has the same reactivity effect as a decrease in fuel loading.

The reflector temperature coefficient was calculated by making a uniform temperature perturbation in all the regions outside the core. Since cell effects were not involved, the procedure consisted simply of generating appropriate microscopic thermal cross sections for the perturbed and unperturbed cases and processing by DAC to obtain the worth of the perturbation. For a perturbation of 100°C, the calculated reflector coefficient was $+1.19 \times 10^{-4}$ $(\Delta k/k)/°C$. An increase in temperature reduces the thermal absorption cross section and has very little effect on the thermal scattering cross section. Thus, the distributed reflector temperature coefficient (Fig. 3.28) is similar, but opposite in sign, to the distributed worth of an absorber.

The net isothermal temperature coefficient is the sum of the core and reflector coefficients. For a temperature perturbation of 100°C, the perturbation result for the net temperature coefficient is thus -0.67×10^{-4} $(\Delta k/k)/°C$. The net coefficient was also computed by the k_{eff} difference method to check the perturbation results. The perturbation value was within 4% of the k_{eff} difference value.

A study of the neutron economy in the two k_{eff} problems showed that about 90% of the isothermal temperature coefficient results from changes in the core thermal nonleakage probability (Appendix G). An increase in core temperature decreases the thermal absorption cross section, which results in an increase in thermal neutron leakage from the core. An increase in reflector temperature decreases the thermal absorption and results in an increase in the thermal neutrons returned to the core.

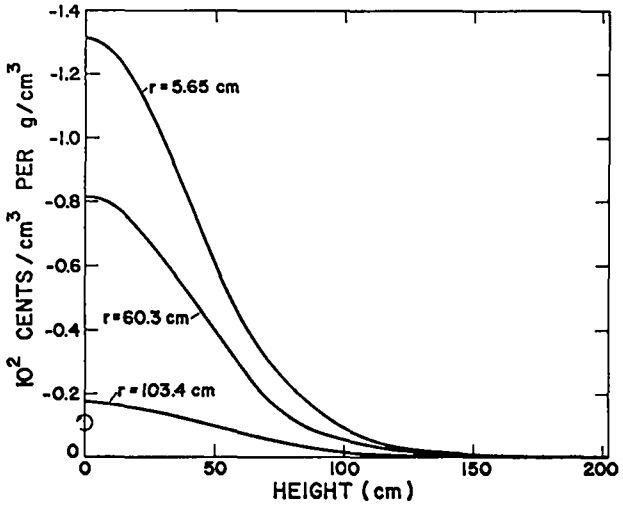

Fig. 3.28. Distributed reflector temperature coefficient in UCX-II.

The fuel element temperature coefficient is about 8% of the core temperature coefficient. Since the moderator contained in the fuel elements is only about 4% of the total mass of moderator in the core, the moderator in the fuel elements is twice as effective as the bulk core moderator. Because most of the thermal absorptions in the cell occur in the fuel element, thermal leakage from the core is affected more by the thermal neutron spectrum in the fuel elements than by that in the bulk moderator. The thermal neutron spectrum in the fuel elements, however, is more sensitive to a temperature perturbation of the fuel element moderator than of an equal mass of moderator outside the fuel element.

Reactivity changes associated with two temperature increments above room temperature were measured in UCX-II (Sec. 2.6). These experiments were performed as an approximate check on the calculated isothermal core and reflector temperature coefficients. The experiments did not provide a rigorous test of the calculated coefficients because the temperature distributions during the experiments were not strictly isothermal and because only the combined effect of the core and reflector temperature coefficients could be measured.

Estimates of the steady-state temperatures in the 26 regions of the calculational model (Fig. 3.11) were made from the thermocouple measurements (Table 2.13). Using the regional temperature coefficients computed by perturbation theory, the reactivity change for the two temperature increments was calculated. For the first increment, the perturbation calculation yielded a reactivity change of -35.1¢; the measured value was -44.4¢. For the second increment, the perturbation calculation yielded a reactivity change of -63.4¢; the measured value was -89.6¢.

In addition to the reasons stated above, two effects are suggested to explain at least part of the discrepancy between calculation and experiment. First, the calibrated control rod used to measure the reactivity change perturbed the fluxes and currents in the reactor. This perturbation might be significant because the rod was 10 in. below the top of the core in the reference room temperature case. This effect could not be accounted for in the two-dimensional perturbation calculations, where the fluxes and currents were those for the unrodded reactor. Second, some uncertainty exists in the estimated regional temperatures, particularly in those reflector and insulating carbon regions where few or no thermocouples were available.

Self-Shielding. In all the perturbation calculations, the cross sections for the unperturbed case contained the effects of self-shielding in the coated particles and fuel elements. In order to compute the worths of these effects, perturbations were made in which these effects were removed. That is, the spatial flux distributions in the core cells and in the fuel particles were assumed to be flat in the perturbed cases.

Self-shielding in the coated particles and in the fuel elements was calculated to be, respectively, -2.05% $\Delta k/k$ and -3.56% $\Delta k/k$. The combined worth of these two effects is equivalent to about 1.4 kg of fuel in UCX-II. In other words, if the uranium were dispersed homogeneously throughout the core annulus, instead of being concentrated in fuel particles and fuel elements, the critical mass for UCX-II would be about 5 kg instead of 6.3 kg. Since the worth of self-shielding in the fuel elements is large, the perturbation result for this case was checked with the k_{eff} difference method. The perturbation value was within 4% of the k_{eff} difference value.

APPENDIX A

ANALYSIS OF IMPURITIES IN GRAPHITE AND CARBON COMPONENTS

Impurities in various graphite and carbon components of UHTREX were determined by spectrochemical analyses of several samples from each component. Results of these analyses are given in Table A.1. Only those elements for which definite amounts were reported in the analyses are included in the tables. Since only aluminum, boron, and iron were used in the neutronic calculations as impurities, other elements present were included as an equivalent (in terms of thermal absorption) amount of aluminum, boron, or iron.

From the impurities in the tables and a value of 3.7 mb for pure carbon, the 2200 m/sec absorption cross section ranges from 5.8 to 8 mb for the various components. These values are higher than those (4.5 to 6 mb) usually encountered in nuclear graphites. The accuracy of the absorption cross section is determined by the completeness of the spectrochemical analysis and the precision of the determinations of the various elements.

Relatively large concentrations are required for quantitative determination, by the spectrochemical method, of the rare-earth elements. Because the thermal absorption cross sections of these elements are very large, the uncertainty in the concentration of the rare earths is a defect in the spectrochemical method.

TABLE A.1

SPECTROCHEMICAL ANALYSES OF GRAPHITE AND CARBON COMPONENTS

Impurity	Elements Included	σ_a (2200 m/sec) (b)	Core Moderator Graphite ppm[a]	Core Moderator Graphite Equivalent ppm of Impurity	Dense Carbon ppm	Dense Carbon Equivalent ppm of Impurity	Reflector Graphite ppm	Reflector Graphite Equivalent ppm of Impurity	Unloaded Fuel Element ppm	Unloaded Fuel Element Equivalent ppm of Impurity	Porous Carbon ppm	Porous Carbon Equivalent ppm of Impurity
Al	Al	0.23	88	1501	70	1686	100	2628	50	2661	42	1345
	Na	0.50	37		92		108		40		200	
	Mg	0.06	12		20		20		50		10	
	Si	0.13	184		436		412		300		160	
	K	1.97	83		106		150		-		84	
	Ca	0.43	275		137		412		100		30	
	Ti	5.60	-		-		-		50		-	
	V	4.98	-		-		-		20		-	
	Cr	2.9	-		-		-		40		-	
B	B	755	0.875	1.1007	0.2222	0.2222	2	2.2821	3	3	0.6	0.8
	Li	71	2.4		-		3		-		2	
Fe	Fe	2.53	262	505	283	610	450	797	200	273	160	466
	Ti	5.60	22.5		4.4		50		-		5	
	V	4.98	45		44.4		40		-		50	
	Cr	2.9	21.6		6		20		-		3	
	Mn	13.2	6.6		3.6		10		-		1	
	Ni	4.6	10		100		10		30		100	
	Cu	3.62	5		9.4		10		10		4	
	Zn	1.06	2		12.8		-		-		-	
	Sr	1.16	10		-		20		-		-	
	Nb	1.1	1		1.1		-		-		-	
	Mo	2.5	6		-		30		-		-	
	Ba	1.17	16		5		20		10		-	
	Pb	0.17	15		11.4		30		-		3	

[a]Number of impurity atoms per million carbon atoms.

APPENDIX B

FUEL PARTICLE SELF-SHIELDING

The fuel in UHTREX consists of uranium dicarbide (UC_2) spheres of nominally 150 μ diam coated with about 100 μ of pyrolytic carbon and dispersed in a matrix of graphite. Various methods of calculating self-shielding factors were investigated.[25] It was found that scattering effects and particle interaction effects on thermal neutrons may be neglected. Thus, an isotropic source was assumed on the surface of the particle, and the self-shielding factor S was calculated as the ratio of the probability of absorption in the sphere including self-shielding to the probability of absorption neglecting self-shielding. The probability in each case was found by integrating over all paths through the sphere. The self-shielding factor so derived is

$$S = \frac{2}{y}\left[1 - \frac{1}{y}(1 - e^{-y})\right] ,$$

where

$$y = \Sigma_a d$$

is the "optical diameter," d is the actual diameter, and Σ_a is the macroscopic absorption cross section. For small y

$$S = 1 - \frac{1}{3} y + \frac{1}{12} y^2 - \ldots$$

In the computation of self-shielding factors, it was assumed that the UC_2 fuel particle core had a density of 11.28 g/cm^3 and that the isotopic abundances of uranium in the coated-particle cores were as shown in Table B.1. The particle size distribution shown in Fig. B.1 was also taken into account.

TABLE B.1

ISOTOPIC ABUNDANCES OF URANIUM IN COATED PARTICLE CORES

Isotope	Abundance (%)
^{234}U	0.87
^{235}U	93.10
^{236}U	0.28
^{238}U	5.75

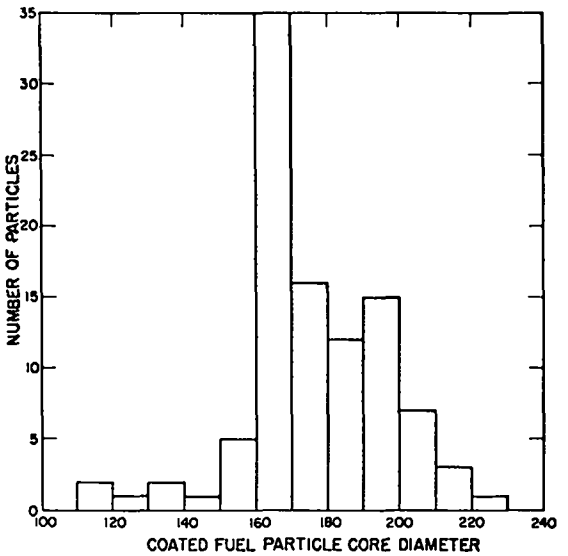

Fig. B.1. Fuel particle size distribution.

That is, self-shielding factors were computed for particle diameters of 115, 125, 135, 145, 155, 165, 175, 185, 193, 205, 215, and 225 μ, and then these self-shielding factors were weighted by the size distribution of Fig. B.1 to obtain an effective self-shielding factor for each of the energy groups used in infinite medium thermalization calculations.

A set of self-shielding factors for the 59-group case is given in Table B.2. The self-shielding in the fuel particles was calculated to be worth -2% Δk.

TABLE B.2

SELF-SHIELDING FACTORS

Group	Self-Shielding Factor	Group	Self-Shielding Factor
59	0.5274	29	0.9656
58	0.6915	28	0.9668
57	0.7758	27	0.9679
56	0.8192	26	0.9688
55	0.8453	25	0.9694
54	0.8625	24	0.9698
53	0.8750	23	0.9701
52	0.8849	22	0.9702
51	0.8928	21	0.9703
50	0.8994	20	0.9702
49	0.9051	19	0.9698
48	0.9101	18	0.9685
47	0.9144	17	0.9673
46	0.9198	16	0.9667
45	0.9260	15	0.9688
44	0.9312	14	0.9727
43	0.9356	13	0.9763
42	0.9393	12	0.9799
41	0.9425	11	0.9822
40	0.9453	10	0.9839
39	0.9479	9	0.9857
38	0.9501	8	0.9882
37	0.9522	7	0.9904
36	0.9540	6	0.9912
35	0.9556	5	0.9874
34	0.9572	4	0.9920
33	0.9585	3	0.9972
32	0.9603	2	0.9965
31	0.9624	1	0.9981
30	0.9641		

APPENDIX C

59-GROUP THERMAL CROSS SECTIONS

Microscopic 59-group cross sections for Al, B, C, Fe, ^{234}U, ^{235}U, and ^{238}U are given in Table C.1. The 59-group energy structure, which covers the range 0 to 3 eV, is given in Table 3.3. The absorption (σ_a) and total scattering (σ_s) cross sections are given for all these nuclides. In addition, the fission cross section (σ_f) is given for ^{235}U.

The total cross section was defined by $\sigma_t = \sigma_a + \sigma_s$ and the transport cross section by $\sigma_{tr} = \sigma_a + (1 - \bar{\mu})\,\sigma_s$, where $\bar{\mu}$ is the average cosine of the scattering angle in the laboratory system. For the nuclides in the tables, the approximation $\bar{\mu} = 2/3A$, where A is the atomic mass, was used.

In general, the 59-group cross sections were obtained by averaging the point cross sections over the group limits with a Maxwellian spectrum as the weighting function. Except for a few groups, the 59-group structure is fine enough that the cross section at the energy corresponding to the midpoint of a group is a good approximation of the averaged cross section for that group.

Except for ^{235}U, the absorption cross sections were assumed to follow the 1/v law with 0.0253 eV values as shown in Table C.2. For Al, Fe, and ^{238}U σ_t was obtained from the point data in Ref. 26, and the scattering cross section was computed from

TABLE C.1

59-GROUP CROSS SECTIONS
(b)

Group	Aluminum		Boron[a]	Carbon		Iron		^{234}U[b]	^{235}U[c]		^{238}U	
	σ_a	σ_s	σ_a	σ_a[d]	σ_s	σ_a	σ_s	σ_a	σ_a	σ_f	σ_a	σ_s
1	0.0224	1.328	73.47	0.36	4.71	0.246	11.20	10.22	15.44	10.72	0.259	8.941
2	0.0254	1.375	83.37	0.41		0.279	11.17	11.60	24.27	12.84	0.301	8.929
3	0.0292	1.421	95.87	0.47		0.321	11.13	13.33	20.65	14.24	0.347	9.003
4	0.0335	1.446	110.1	0.54		0.369	11.08	15.31	56.74	39.24	0.398	9.022
5	0.0373	1.443	122.4	0.60		0.410	11.04	17.03	89.68	73.29	0.443	9.057
6	0.0410	1.439	132.4	0.65	4.72	0.444	11.06	18.41	62.81	55.05	0.488	8.932
7	0.0451	1.455	148.0	0.73	4.73	0.496	11.00	20.58	68.16	60.49	0.535	8.885
8	0.0491	1.451	161.1	0.80	4.73	0.540	10.96	22.40	83.60	73.49	0.582	8.848
9	0.0518	1.458	170.0	0.84	4.74	0.570	10.93	23.64	101.6	87.06	0.615	8.825
10	0.0535	1.466	175.7	0.87		0.589	10.96	24.44	114.9	98.12	0.635	8.815
11	0.0576	1.462	189.2	0.93		0.634	10.92	26.31	126.9	109.0	0.684	8.786
12	0.0582	1.472	191.1	0.94	4.75	0.640	10.91	26.57	146.7	124.5	0.691	8.809
13	0.0607	1.469	199.2	0.98		0.667	10.88	27.70	170.1	142.3	0.720	8.780
14	0.0627	1.467	206.0	1.02		0.690	10.91	28.64	196.6	161.8	0.745	8.775
15	0.0653	1.475	214.3	1.06	4.76	0.718	10.88	29.80	225.4	180.7	0.775	8.765
16	0.0681	1.472	223.4	1.10		0.749	10.85	31.07	240.6	190.2	0.808	8.742
17	0.0712	1.479	233.9	1.16		0.784	10.87	32.53	236.2	184.4	0.846	8.714
18	0.0735	1.476	241.3	1.19	4.77	0.809	10.84	33.56	227.3	176.4	0.873	8.697
19	0.0751	1.475	246.4	1.22		0.826	10.82	34.27	218.2	173.3	0.891	8.689
20	0.0767	1.473	251.9	1.24		0.844	10.86	35.03	215.1	171.4	0.911	8.679
21	0.0785	1.472	257.7	1.27	4.78	0.863	10.84	35.83	214.3	171.4	0.932	8.668
22	0.0804	1.470	263.9	1.30		0.884	10.87	36.70	214.5	172.3	0.954	8.646
23	0.0824	1.468	270.6	1.34		0.907	10.84	37.63	215.7	173.9	0.978	8.622
24	0.0846	1.475	277.8	1.37		0.931	10.82	38.63	217.5	176.2	1.004	8.616
25	0.0870	1.473	285.6	1.41		0.957	10.79	39.72	220.5	180.0	1.033	8.597
26	0.0896	1.470	294.2	1.45		0.986	10.81	40.91	225.6	184.9	1.064	8.586
27	0.0925	1.478	303.5	1.50	4.79	1.017	10.78	42.21	231.8	190.8	1.098	8.552
28	0.0956	1.474	313.8	1.55	4.79	1.052	10.80	43.65	239.9	198.3	1.135	8.565
29	0.0991	1.481	325.3	1.61	4.80	1.090	10.81	45.24	249.2	206.8	1.176	8.574
30	0.1030	1.497	338.1	1.67	4.83	1.133	10.77	47.02	260.3	216.4	1.222	8.558
31	0.1074	1.493	352.5	1.74	4.82	1.181	10.77	49.02	272.8	227.4	1.275	8.525
32	0.1124	1.488	369.0	1.82	4.80	1.236	10.76	51.31	288.6	240.7	1.334	8.486
33	0.1165	1.484	382.5	1.89	4.75	1.282	10.72	53.19	301.7	252.0	1.383	8.447
34	0.1196	1.430	392.7	1.94	4.70	1.316	10.68	54.61	312.0	260.4	1.420	8.430
35	0.1230	1.427	403.7	1.99		1.353	10.65	56.15	323.5	269.8	1.460	8.440
36	0.1267	1.403	415.8	2.05		1.393	10.61	57.83	336.0	280.3	1.504	8.446
37	0.1307	1.369	429.0	2.12	4.75	1.438	10.66	59.66	349.5	291.7	1.551	8.419
38	0.1351	1.365	443.6	2.19	4.85	1.486	10.61	61.69	365.4	304.5	1.604	8.386
39	0.1400	1.360	459.7	2.27	5.05	1.541	10.61	63.94	382.6	318.7	1.662	8.338
40	0.1456	1.404	477.8	2.36	5.05	1.601	10.60	66.45	402.0	335.2	1.728	8.292
41	0.1510	1.399	495.7	2.45	4.71	1.661	10.64	68.93	424.1	353.6	1.792	8.258
42	0.1580	1.402	518.8	2.56	4.80	1.739	10.66	72.16	448.6	374.9	1.876	8.224
43	0.1670	1.383	548.2	2.71	4.84	1.837		76.23	477.2	398.7	1.982	8.218
44	0.1766	1.374	579.5	2.86	4.60	1.942		80.60	511.7	426.9	2.096	8.204
45	0.1880	1.312	617.0	3.05	4.56	2.068	10.68	85.81	552.5	459.6	2.231	8.219
46	0.2019	1.328	662.9	3.27	4.64	2.221	10.78	92.19	601.8	500.3	2.397	8.103
47	0.2145	1.326	704.2	3.48	4.56	2.360	10.64	97.94	645.8	537.9	2.546	8.054
48	0.2245	1.276	737.0	3.64	4.94	2.470	10.73	102.5	680.8	566.6	2.665	8.035
49	0.2360	1.264	774.9	3.83	5.10	2.597	10.80	107.8	721.6	600.2	2.802	7.998
50	0.2496	1.300	819.2	4.05	4.95	2.745	10.76	113.9	768.3	638.0	2.962	7.938
51	0.2657	1.484	872.1	4.31	4.95	2.922	10.68	121.3	823.0	685.8	3.153	7.947
52	0.2854	1.665	936.8	4.63	4.49	3.139	10.66	130.3	890.3	742.9	3.387	8.113
53	0.3103	1.490	1018.	5.03	3.45	3.413	10.59	141.6	975.8	812.7	3.683	6.817
54	0.3430	1.357	1126.	5.56	3.73	3.773	10.48	156.6	1084.	907.0	4.071	6.429
55	0.3889	1.211	1277.	6.31	4.42	4.278	10.72	177.5	1239.	1040.	4.616	5.784
56	0.4600	1.340	1510.	7.46	4.06	5.060	11.94	210.0	1484.	1245.	5.460	5.940
57	0.5927	1.007	1946.	9.61	3.99	6.519	0.951	270.6	1919.	1626.	7.035	5.465
58	0.8642	0.266	2837.	14.02	4.25	9.507	1.303	394.5	2885.	2414.	10.26	5.465
59	1.5370	0.383	5047.	24.93	1.00	16.91	2.079	701.9	5474.	4562.	18.25	5.465

[a] σ_s = 4 barns
[b] σ_s = 0
[c] σ_s ≈ 15 barns, ν = 2.43
[d] units of mb.

TABLE C.2

ABSORPTION CROSS SECTIONS
AT 0.0253 eV FOR 1/v ABSORBERS

Nuclide	σ_a (barns)
Al	0.230
B	755
C	0.00373
Fe	2.53
^{234}U	105
^{238}U	2.71

$\sigma_s = \sigma_t - \sigma_a$. For boron σ_s is very small compared to σ_a and, therefore, it was assumed that σ_s was constant at 4 b. Also, the scattering cross section for ^{234}U was taken to be zero, because the concentration of this nuclide is very small and thus makes a negligible contribution to the macroscopic scattering cross section of the core.

For carbon σ_t was obtained from the point data in Ref. 26, and the total scattering was computed from $\sigma_s = \sigma_t - \sigma_a$. In addition to σ_a and σ_s, the inelastic scattering kernel is required for carbon. The kernel is a 59 x 59 matrix for the 59-group energy structure and hence is not reproduced here. The point kernel, $\sigma(E_{g'} \rightarrow E_g)$, where $E_{g'}$ and E_g are discrete energies corresponding to the group boundaries, was computed with the SUMMIT code. This point kernel, which is temperature dependent, was used in the THERM code to compute the group transfer matrix $\sigma(g' \rightarrow g)$ required in the calculation of the 59-group infinite medium thermal neutron spectrum.

The cross sections for ^{235}U were obtained from two sources. For $E \leq 0.19$ eV, σ_t and σ_f were obtained from the data in Ref. 27. The absorption cross section was computed from $\sigma_a = \sigma_t - \sigma_s$ where $\sigma_s = 15$ b. For $E > 0.19$ eV, σ_f and α were obtained from the data in Ref. 28, and absorption was computed from $\sigma_a = (1 + \alpha)\ \sigma_f$.

APPENDIX D

ADDITIONAL THERMALIZATION STUDIES

As mentioned in Sec. 3.2, the SUMMIT and THERM codes[19] were used in most of the thermalization calculations. That is, the crystalline scattering kernel for graphite was computed with the SUMMIT code, and the thermal spectrum calculations were performed with the THERM code. Recently, two equivalent programs, the TOR and GLEN codes[20,21] were developed at LASL. A few calculations were made with these codes to compare with the SUMMIT and THERM codes. These additional thermalization studies were made with 87 groups in the thermal energy range (0 to 3 eV).

Inelastic scattering cross sections computed from the SUMMIT and TOR kernels for graphite at 293°K are shown in Fig. D.1. The inelastic cross section $\sigma(E)$ is computed from

$$\sigma(E) = \int dE'\ \sigma(E \rightarrow E') \quad ,$$

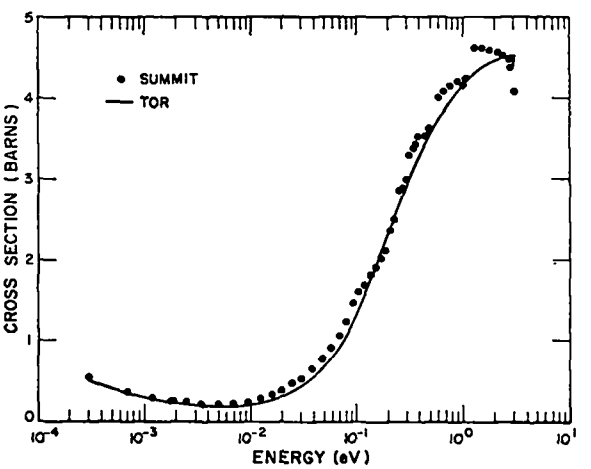

Fig. D.1. Crystalline model inelastic scattering cross section at 293°K.

where $\sigma(E \rightarrow E')$ is the scattering kernel. Results from the two codes agree well, except at the upper end of the thermal energy range, where several discontinuities in the SUMMIT results are evident. In TOR, the cross sections are calculated by direct evaluation of the Fourier integrals involved without recourse to a phonon expansion, as is the case in SUMMIT. A new method[29] of numerical calculation of Fourier integrals is used which makes possible rapid and accurate evaluation even for large values of the frequency parameter.

Thermal neutron spectra obtained with the SUMMIT and TOR kernels are shown in Fig. D.2. The spectra, which are plotted on an arbitrary scale, are for an infinite medium with C/U = 8850, which corresponds to the volume-averaged core composition in UCX-I (7.003-kg load). Note the very close agreement in the spectra, except at the upper end of the thermal energy range, where differences in the kernels were previously noted.

Finite reactor calculations using broad-group thermal cross sections derived with the SUMMIT-THERM and TOR-GLEN codes yielded k_{eff}'s which were within 0.2% $\Delta k/k$ of each other. These calculations were performed in one-dimensional geometry (cylinder) with 25 energy groups (12 fast, 13 thermal) in the S_4 approximation.

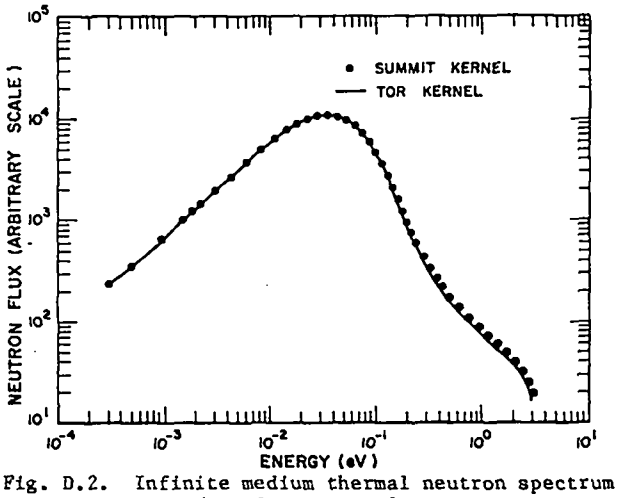

Fig. D.2. Infinite medium thermal neutron spectrum for C/U = 8850 at 293°K.

The SUMMIT and THERM codes provide only the P_0 component of the graphite scattering matrix, whereas the TOR and GLEN codes provide the P_0 through P_3 components. Computations with the P_0 and P_1 (single and double table) approximations indicated that anisotropic scattering in carbon in the thermal energy range is worth about -1% $\Delta k/k$. This effect was found to be adequately accounted for in an isotropic-type solution (single table) using the $(1 - \bar{\mu})$ approximation of the transport correction to the scattering cross section.

APPENDIX E

TESTS OF METHODS USED IN AVERAGING CROSS SECTIONS

Infinite Medium Calculations

In Sec. 3.2, the procedure is described for reducing the original 59 thermal groups to one thermal group for 6-group calculations or to 13 thermal groups for 25-group calculations. In the procedure, the core and reflector regions are homogenized separately to obtain two different media for infinite medium calculations. The fluxes obtained from the infinite medium calculations are used as weighting factors in the group reduction procedure.

In actuality, the thermal spectrum will vary continuously from a relatively soft spectrum deep in the reflector regions where the thermal absorption is low to a relatively hard spectrum in the core interior where the thermal absorption is high. Furthermore, variation in the core thermal spectrum is expected due to the radial variation in the C/U ratio.

To investigate further the effects of the approximations involved, different ways of partitioning the reactor for the infinite medium calculations were studied. Results in terms of the effects on the k_{eff} of UCX-II are summarized in Table E.1. The cross sections obtained from the infinite medium collapsing procedure were first corrected for cell effects and then were used in one-dimensional cylinder calculations of the entire reactor.

TABLE E.1

INFINITE MEDIUM EFFECTS

Case		k_{eff} 25 Groups	k_{eff} 6 Groups
1	Single core medium	0.9905	0.9937
2	Four core media	0.9918	0.9915
3	5-cm reflector added to core	0.9908	1.0017
4	30-cm reflector added to core	0.9918	1.0234

Cases 1 and 2 show the changes in k_{eff} produced by subdividing the core into four separate regions or media for collapsing cross sections. For Case 1, the standard two-region (core and reflector) procedure was used. In Case 2, the core was subdivided into the four radial regions used to define cells as described in Sec. 3.3. The changes in k_{eff} for both the 6-group and 25-group structures are small.

Cases 3 and 4 were the same as Case 1, except that portions of the radial reflector were lumped with the core. In Case 3, the core region was extended 5 cm into the central plug and 5 cm into the outer radial reflector. In Case 4, the same extensions were increased to 30 cm. Changes in k_{eff} for the 25-group case are again small, but in the 6-group case the effects of increasing the effective average C/U ratio of the core by this means are of some significance.

For the 6-group structure, which contains a single broad thermal group, the volume-averaged core medium (Case 1) for determining the thermal weighting spectrum for the entire core yields the best agreement with the measured radial fission distribution. For the 25-group structure, the results are not sensitive to the regional spectrum used, indicating that 13 thermal groups provide a sufficiently fine structure for the thermal neutron spectrum variations encountered in the core.

The best agreement (in k_{eff}) between the 6- and 25-group calculations is obtained with four core media (Case 2). However, the agreement using the simpler approach of Case 1 is also adequate.

Cell Calculations

The problem of cell definitions in UHTREX is discussed at length in Sec. 3.3. In the calculations described therein, the core was divided into four radial regions corresponding to the four radial fuel element locations in order to perform cell calculations. A question remains as to whether four sections is a fine enough subdivision of the core to account for the continuously varying fuel-to-moderator-volume ratio.

To check this point, calculations with 12 cells were performed for comparison to the calculations with four cells. The results for k_{eff} are given in Table E.2. In the 12-cell calculations, each of

TABLE E.2

k_{eff} FOR 4- AND 12-CELL CASES

Number of Cells	k_{eff} 25 Groups	k_{eff} 6 Groups
4	0.9905	0.9937
12	0.9871	0.9908

the four original core regions was subdivided into three regions of equal radial increments. Both 6- and 25-group calculations were performed with a one-dimensional cylinder model of UCX-II. For both group structures, k_{eff} was reduced about 0.3% by increasing the number of cells from 4 to 12. Calculated radial fission distributions for both four and 12 cells agree closely with measurements in a fuel channel by wire irradiation (Fig. E.1). Thus, the four-cell approach was considered adequate for UHTREX calculations.

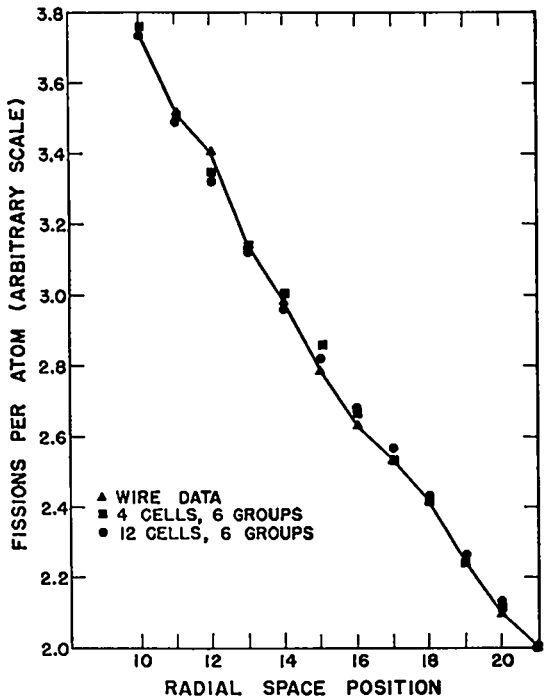

Fig. E.1. Radial fission distributions in UCX-II from four and 12 cell procedures.

In the 4-cell calculations, the core control-rod holes were distributed in the form of annuli in cells 2 and 3 (Sec. 3.3). Thus, the holes were distributed over a large fraction of the core when in actuality they are very localized. In the 12-cell calculations, the radial position of these holes could be more accurately represented by distributing the holes in cells 6 and 7.

Cell calculations with the control-rod void annulus located in various positions in the moderator gave identical results for the effective cell cross sections. This fact, in addition to the fact that the 4-cell and 12-cell calculations yielded similar results, indicates that the method of treating the core control-rod holes in the cell calculations is not of major importance.

APPENDIX F

MATERIAL COMPOSITIONS

APPENDIX F: MATERIAL COMPOSITIONS

Fuel element compositions are given in Table F.1. The atom densities of the uranium isotopes vary with the uranium loading in the fuel element. Atom densities for aluminum, boron, carbon, and iron were assumed to be independent of the uranium loading. The atom density for carbon is based on a fuel element density of 1.80 g/cm^3 exclusive of the uranium content. The atom densities for aluminum, boron, and iron are based on the spectrochemical analysis (Appendix A) of the fuel element graphite.

TABLE F.1

COMPOSITIONS OF FUEL ELEMENTS
(atom densities in units of 10^{20} atoms/cm^3)

Element Load (g)	^{234}U[a]	^{235}U	^{238}U
3.54	0.01512	1.588	0.0981
4.16	0.01777	1.867	0.1153
4.82	0.02060	2.164	0.1337
5.67	0.02423	2.546	0.1572
6.57	0.02806	2.949	0.1821

	Al	B	C	Fe
All fuel elements	2.409	0.002715	905.1	0.2471

[a] ^{236}U was included as an equivalent amount of ^{234}U.

The compositions of the core moderator are given in Table F.2. Compositions are given for the four core regions discussed in Sec. 3.3 (Fig. 3.4). Core volume fractions of each of the four core regions are also given in the table. The densities of the six concentric graphite cylinders which make up the core vary from 1.74 to 1.66 g/cm^3. Thus, the atom densities in the moderator vary with position in the core. Relative amounts of aluminum, boron, and iron in the core moderator were determined from spectrochemical analyses (Appendix A).

TABLE F.2

COMPOSITIONS OF CORE MODERATOR
(atom densities in units of 10^{20} atoms/cm^3)

Region	Core Volume Fraction	Al	B	C	Fe
1	0.1596	1.310	0.0009604	872.5	0.4406
2	0.2199	1.285	0.0009422	856.0	0.4323
3	0.2801	1.270	0.0009312	846.0	0.4272
4	0.3404	1.252	0.0009179	833.9	0.4211

Atom densities in Tables F.1 and F.2 were used in the cell calculations described in Sec. 3.3. If these atom densities are homogenized over the volume of the cell (cell specifications are given in Table 3.5) or over the entire core, atom densities for the infinite medium thermalization calculations are obtained.

The materials used in the noncore regions are defined in Table F.3.

TABLE F.3

MATERIALS USED IN NONCORE REGIONS

Material	Element[a]	Weight Fraction	Material Density (g/cm^3)
core graphite	aluminum[b]	3.3718×10^{-3}	1.73
	boron[c]	9.9067×10^{-7}	
	carbon[d]	9.9428×10^{-1}	
	iron[e]	2.3483×10^{-3}	
dense carbon	aluminum	3.7874×10^{-3}	1.65
	boron	1.9998×10^{-7}	
	carbon	9.9337×10^{-1}	
	iron	2.8365×10^{-3}	
porous carbon	aluminum	3.0212×10^{-3}	1.02
	boron	2.7000×10^{-7}	
	carbon	9.9481×10^{-1}	
	iron	2.1668×10^{-3}	
steel	iron	1.0000	7.837
carbon felt	aluminum	3.6000×10^{-4}	0.5
	boron	1.4000×10^{-6}	
	carbon	9.9775×10^{-1}	
	iron	1.8900×10^{-3}	
void	carbon	1.0000	0.0
reflector graphite	aluminum	5.9030×10^{-3}	1.73
	boron	2.0558×10^{-6}	
	carbon	9.9039×10^{-1}	
	iron	3.7063×10^{-3}	

[a] Input as microscopic cross sections for regions outside the core only.

[b] Atomic weight = 26.98

[c] Atomic weight = 10.81

[d] Atomic weight = 12.011

[e] Atomic weight = 55.85

APPENDIX G

NEUTRON ECONOMY ANALYSIS OF TEMPERATURE COEFFICIENTS

Neutron balance parameters from a 2DF calculation of UCX-II at room temperature (293°K) are given in Table G.1. The upper five groups in the six-group 2DF calculation were summed to obtain the fast absorptions and leakages, and the sixth (thermal) group results were taken directly for the slow losses. If the balance were perfect, the last two rows giving total losses and sources would be identical. However, the source of 101.10 fission neutrons/sec compared to losses of 100 neutrons/sec reflects the slight supercriticality in the calculation of the experimentally critical configuration.

Using the abbreviations in Table G.1, the results for the core can be summarized in terms of the modified one-group expression

$$k_{eff} = \frac{S}{A + L} = k_\infty P_f P_{th} \cdot C \quad , \tag{G.1}$$

where

$$k_\infty = S/A \tag{G.2}$$

is the infinite reproduction factor,

$$P_f = \frac{A + L_2}{A + L} \tag{G.3}$$

TABLE G.1

UCX-II NEUTRON BALANCE AT 293°K

	Core	Reflector[a]	Reactor Totals
Absorptions			
Fast, A_1	2.65	0.10	2.75
Slow, A_2	54.10	42.62	96.72
Total, A	56.75	42.72	99.47
Leakages			
Fast, L_1	43.59	- 43.07	0.52
Slow, L_2	- 0.34	0.35	0.01
Total, L	43.25	- 42.72	0.53
Total Losses			
Fast	46.26	- 42.97	3.27
Slow	53.76	42.97	96.73
Total	100.00	0	100.00
Sources, S	101.10	0	101.10

[a]Includes all regions other than the core.

is the fast nonleakage probability,

$$P_{th} = \frac{A_2}{A_2 + L_2} \qquad (G.4)$$

is the thermal nonleakage probability, and

$$C = \frac{1 + L_2/A_2}{1 + L_2/A} \qquad (G.5)$$

is a factor required to make Eq. G.1 consistent with Eqs. G.2 through G.4, which provides a measure of the accuracy of the one-group approximation. Since for the core $L_2 \ll A_2$, and, moreover, $L_2/A_2 \approx L_2/A$, $C \approx 1.0$, and $k_{eff} = k_\infty P_f P_{th}$ to a fair approximation.

To evaluate temperature effects, three additional calculations of the same UCX-II configuration were performed with 1) core and reflector both at 393°K, 2) core alone perturbed to 393°K, and 3) reflector alone perturbed to 393°K. Results for all cases are summarized in Table G.2.

The changes in the thermal nonleakage probability, P_{th}, dominate the temperature coefficients. Furthermore,

$$\frac{1}{P_{th}} \frac{\partial P_{th}}{\partial T} \approx - \frac{1}{A_2} \frac{\partial L_2}{\partial T} \quad . \qquad (G.6)$$

Thus, although the core thermal leakage L_2 in UHTREX is small, reactivity effects caused by temperature changes are largely determined by the

TABLE G.2

CORE PARAMETERS AND TEMPERATURE COEFFICIENTS

	Case 1	Case 2	Case 3	Case 4
Temperatures (°K)				
Core	293	393	393	293
Reflector	293	393	293	393
k_{eff}	1.011	1.004	0.991	1.023
Core Parameters				
k_∞	1.781	1.780	1.779	1.781
P_f	0.564	0.564	0.565	0.563
P_{th}	1.006	1.000	0.986	1.021
C	1.000	1.000	1.001	0.999
Temperature Coefficients (10^{-4}/°C)				
$\frac{1}{k}\frac{\partial k_\infty}{T}$		-0.07	-0.09	+0.02
$\frac{1}{P_f}\frac{\partial P_f}{\partial T}$		-0.04	+0.08	-0.13
$\frac{1}{P_{th}}\frac{\partial P_{th}}{\partial T}$		-0.62	-2.07	+1.41
$\frac{1}{C}\frac{\partial C}{\partial T}$		+0.03	+0.10	-0.07
$\frac{1}{k_{eff}}\frac{\partial k_{eff}}{\partial T}$		-0.69	-1.98	+1.24

changes in the core thermal leakage. Heating either the core or reflector causes thermal absorption to be reduced in the heated component. Consequently, the core thermal leakage is increased by core heating, but is decreased by reflector heating. This is the basic cause of the difference in sign in the core and reflector temperature coefficients.

For a sufficiently large core, the variation of k_∞ with temperature would dominate the temperature coefficient. It is evident from the data in Table G.2, however, that in UHTREX the temperature coefficient depends only weakly on the changes in k_∞. In addition, the contribution of $1/k_\infty \cdot \partial k_\infty/\partial T$ to the total reflector temperature coefficient is less than 2% which is in agreement with the concept of k_∞.

There is some variation in k_∞ radially in the UHTREX core, since the fuel-to-moderator ratio varies radially. The values of k_∞ at 293°K obtained from calculations of the four core cells (Fig. 3.4) in UHTREX are shown in Table G.3. The

TABLE G.3

CELL AND TEMPERATURE EFFECTS ON k_∞

Cell	k_∞	$\frac{1}{k_\infty}\frac{dk_\infty}{dT}$	$\frac{1}{\eta}\frac{\partial \eta}{\partial T}$	$\frac{1}{f}\frac{\partial f}{\partial T}$
1	1.8052	-9.8×10^{-6}	-9.8×10^{-6}	-0.3×10^{-6}
2	1.7808	-8.5	-9.7	+1.0
3	1.7836	-7.4	-9.7	+2.1
4	1.7540	-5.3	-9.7	+4.3

effects of temperature changes on k_∞ and the factors η and f are also given. The factor η is the ratio of neutrons produced by thermal fissions to thermal absorptions in the fuel elements, and the factor f is the ratio of thermal absorptions in the fuel elements to the thermal absorptions in the cell. The contributions of ε, the fast fission factor, and p, the resonance escape probability, to the temperature variation of k_∞ are small.

REFERENCES

1. "Ultra High Temperature Reactor Critical Experiment (UCX) Safety Analysis Report," LA-3279, Los Alamos Scientific Laboratory (1965).

2. "Ultra High Temperature Reactor Experiment (UHTREX) Facility Description and Safety Analysis Report," LA-3556 (Rev.), Los Alamos Scientific Laboratory (1967).

3. "Quarterly Status Report on Advanced Reactor Technology (ART)," LA-3244-MS (1965), LA-3316-MS (1965), LA-3370-MS (1965), ... LA-3760-MS (1967).

   "Quarterly Status Report on the Ultra High Temperature Reactor Experiment (UHTREX)," LA-3835-MS (1967). LA-3952-MS (1968), LA-3965-MS (1968), LA-4009-MS (1968), LA-4094-MS (1969).

   These are all Los Alamos Scientific Laboratory reports.

4. F. Kim et al., "Reactor Physics Measurements in TREAT," ANL-6173, Argonne National Laboratory (1960).

5. H. P. Iskenderian, "Physics Analysis of the TREAT Reactor Design," ANL-6025, Argonne National Laboratory (1959).

6. K. D. Lathrop, "DTF-IV, A FORTRAN-IV Program for Solving the Multigroup Transport Equation with Anisotropic Scattering," LA-3373, Los Alamos Scientific Laboratory (1965).

7. The 2DF code is a two-dimensional version of the DTF-IV code. It has not been documented separately.

8. B. M. Carmichael and R. J. LaBauve, "Control Rod Calculation Techniques with Applications to the UHTREX Reactor," LA-3194, Los Alamos Scientific Laboratory (1965).

9. A. Hassitt, "A Computer Program to Solve the Multigroup Diffusion Equations," TRG Report 229(R), UKAEA, Risley (1962).

10. J. M. Taub and R. J. Bard, "Coated Particle Fuel Elements for UHTREX," LA-3378, Los Alamos Scientific Laboratory (1966).

11. R. W. Wiesener, "High Temperature Neutron Source for UHTREX," LA-3953, Los Alamos Scientific Laboratory (1968).

12. B. G. Carlson, "Solution of the Transport Equation by S_n Approximations," LA-1599 (1953) and LA-1891 (1955), Los Alamos Scientific Laboratory.

13. C. E. Lee, "The Discrete S_n Approximation to Transport Theory," LA-2595, Los Alamos Scientific Laboratory (1961).

14. R. S. Cooper, "A Code for Reducing Many-Group Cross Sections to Few Groups," LAMS-2801, Los Alamos Scientific Laboratory (1962).

15. L. D. Connolly, ed., "Los Alamos Group-Averaged Cross Sections," LAMS-2941, Los Alamos Scientific Laboratory (1963).

16. G. E. Hansen and W. H. Roach, "Six and Sixteen Group Cross Sections for Fast and Intermediate Critical Assemblies," LAMS-2543, Los Alamos Scientific Laboratory (1961).

17. C. B. Mills, "Fast Reactor Design Computations," LA-3724, Los Alamos Scientific Laboratory (1967).

18. G. I. Bell, "Theory of Effective Cross Sections," LA-2322, Los Alamos Scientific Laboratory (1959).

19. J. Bell, "SUMMIT, An IBM-7090 Program for the Computation of Crystalline Scattering Kernels," GA-2492, General Atomic (1962).

20. W. W. Clendenin, "Calculation of Thermal Neutron Scattering Cross Sections for Crystalline Materials: The TOR Program," LA-3823, Los Alamos Scientific Laboratory (1967).

21. W. W. Clendenin, "Calculation of Thermal Neutron Diffusion Length and Group Cross Sections: The GLEN Program," LA-3893, Los Alamos Scientific Laboratory (1968).

22. R. J. LaBauve, "Heterogeneity Effects in a Radially Loaded Reactor," LA-4024-MS, Los Alamos Scientific Laboratory (1968).

23. W. H. Hannum and B. M. Carmichael, "DPC, A Two-Dimensional Data Preparation Code," LA-3427-MS, Los Alamos Scientific Laboratory (1965).

24. The DDK code is a two-dimensional S_n code written by W. J. Worlton and B. Carlson which is now obsolete. The current version is the 2DF code.

25. G. L. Ragan, "A Method for Calculating Self-Shielding Factors for Materials Containing Closely Spaced Particles," Trans. Am. Nucl. Soc. 10, 584 (1967).

26. D. J. Hughes and R. B. Schwartz, "Neutron Cross Sections," BNL-325 (Second Edition), Brookhaven National Laboratory (1958).

27. D. J. Hughes, B. A. Magurno, and M. K. Brussel, "Neutron Cross Sections," BNL-325 (Second Edition, Supplement No. 1), Brookhaven National Laboratory (1960).

28. J. R. Stehn et al., "Neutron Cross Sections," BNL-325 (Second Edition, Supplement No. 2, Vol. III), Brookhaven National Laboratory (1965).

29. W. W. Clendenin, Numerische Mathematik 8, 422 (1966).